Optical Coherence Tomography: Modeling and Applications

Thrane, Lars; Hanson, Steen Grüner; Skettrup, Torben

Publication date:
2001

Document Version
Publisher's PDF, also known as Version of record

Risø–R–1217(EN)

Optical Coherence Tomography: Modeling and Applications

Lars Thrane

Risø National Laboratory, Roskilde, Denmark
May 2001

Abstract An analytical model is presented that is able to describe the performance of OCT systems in both the single and multiple scattering regimes simultaneously. This model inherently includes the *shower curtain effect*, well-known for light propagation through the atmosphere. This effect has been omitted in previous theoretical models of OCT systems. It is demonstrated that the shower curtain effect is of utmost importance in the theoretical description of an OCT system. The analytical model, together with proper noise analysis of the OCT system, enables calculation of the SNR, where the optical properties of the tissue are taken into account. Furthermore, by using the model, it is possible to determine the lateral resolution of OCT systems at arbitrary depths in the scattering tissue. During the Ph.D. thesis project, an OCT system has been constructed, and the theoretical model is verified experimentally using this system. A demonstration of the imaging capabilities of the OCT system is given. Moreover, a novel *true-reflection OCT imaging algorithm*, based on the new OCT model presented in this thesis, is demonstrated. Finally, a theoretical analysis of the Wigner phase-space distribution function for the OCT geometry, i.e., reflection geometry, is developed. As in the new OCT model, multiple scattered photons has been taken into account together with multiple scattering effects. As an important result, a novel method of creating images based on measurements of the momentum width of the Wigner phase-space distribution is presented, and compared with conventional OCT.

This thesis is submitted to the Technical University of Denmark as part of the requirements for the Doctor of Philosophy degree in Physics.

ISBN 87–550–2771–7; 87–550–2882–9 (Internet)
ISSN 0106–2840

Print: Danka Services International A/S, 2001

Contents

Preface

The present thesis describes the work carried out during the period March 1997 to August 2000 in the Optics and Fluid Dynamics Department at Risø National Laboratory, Denmark while being enrolled as a Ph.D. student at Department of Physics, the Technical University of Denmark. The project has been financed by The Danish Technical Research Council, Risø National Laboratory, and The Center for Biomedical Optics and New Laser Systems. The Ph.D. thesis work has been supervised by:

- Steen G. Hanson, Head of Scientific Programme, Risø National Laboratory, Denmark
- Peter E. Andersen, Senior scientist, Risø National Laboratory, Denmark
- Torben Skettrup, Docent, Technical University of Denmark

I would like to express my sincere gratitude to my supervisors for their kind help and support during the project. A special thanks to Peter E. Andersen for a fruitful and enjoyable collaboration. Also a special thanks to Harold T. Yura from The Aerospace Corporation, USA, who introduced me to the extended Huygens-Fresnel formalism. As a frequent guest scientist at Risø National Laboratory during the Ph.D. thesis project, he has contributed considerably to the theoretical analyses in this thesis. It has been a great experience working with you, Hal.

I also take the opportunity to thank:

- Thomas M. Jørgensen, Risø National Laboratory for having developed software to handle the processing and display of OCT data, and for many valuable discussions.
- René S. Hansen, Risø National Laboratory for different kinds of technical assistance, and fruitful discussions.
- Thim N. Andersen, René L. Eriksen, Peter S. Jensen, and Steven Kitchen, Risø National Laboratory, for being volunteers in connection with the OCT imaging investigations. A special thanks to Peter S. Jensen for always being very helpful.
- Andreas Tycho, COM, Technical University of Denmark for a good collaboration and many fruitful discussions.
- Merete Hædersdal, Bispebjerg Hospital, Denmark for valuable discussions, and for providing me with mouse biopsies.

Finally, I would like to thank the rest of my colleagues in the Optics and Fluid Dynamics Department at Risø National Laboratory for good interactions.

Lars Thrane, August 2000.

List of publications

The Ph.D. thesis work has resulted in the following publications:

- L. Thrane, H. T. Yura, and P. E. Andersen, "Analysis of optical coherence tomography systems based on the extended Huygens-Fresnel principle," J. Opt. Soc. Am. A **17**, 484-490 (2000).
- H. T. Yura, L. Thrane, and P. E. Andersen, "Closed form solution for the Wigner phase-space distribution function for diffuse reflection and small-angle scattering in a random medium," J. Opt. Soc. Am. A **17**, 2464-2474 (2000).
- L. Thrane, H. T. Yura, and P. E. Andersen, "Optical coherence tomography: New analytical model and the shower curtain effect," Proc. SPIE **4001**, pp. 202-208 (2000).
- L. Thrane, H. T. Yura, and P. E. Andersen, "Calculation of the maximum obtainable probing depth of optical coherence tomography in tissue," Proc. SPIE **3915**, pp. 2-11 (2000).
- P. E. Andersen, L. Thrane, H. T. Yura, A. Tycho, and T. M. Jørgensen, "Modeling the optical coherence tomography geometry using the extended Huygens-Fresnel principle and Monte Carlo simulations," Proc. SPIE **3914**, pp. 394-406 (2000) (invited paper).
- A. Tycho, T. M. Jørgensen, and L. Thrane, "Investigating the focusing problem in OCT: comparison of Monte Carlo simulations, the extended Huygens-Fresnel principle and experiments," Proc. SPIE **3915**, pp. 25-35 (2000).

1 Introduction

Optical coherence tomography (OCT) has developed rapidly since its potential for applications in clinical medicine was first demonstrated in 1991 [1]. OCT performs high-resolution, cross-sectional tomographic imaging of the internal microstructure in materials and biologic systems by measuring backscattered or backreflected light.

The origin of OCT lie in the early work on white-light interferometry that led to the development of optical coherence-domain reflectometry (OCDR), a one-dimensional optical ranging technique [2],[3]. OCDR uses short coherence length light and interferometric detection techniques to obtain high sensitivity, high resolution range information. OCDR was developed for finding faults in fiber-optic cables and network components [2],[3]. However, its ability to perform ranging measurements in the retina [4],[5] and other eye structures [4],[5],[6] was soon recognized. D. Huang *et al.* [1] then extended the technique of OCDR to tomographic imaging in biological systems by developing the OCT system. The OCT system performs multiple longitudinal scans at a series of lateral locations to provide a two- or three-dimensional map of reflection sites in the sample.

In the original OCT system [1], low-coherence light from a broad bandwidth superluminescent diode (SLD) centered at 830 nm is coupled into a single-mode fiber-optic Michelson interferometer. Light exiting the sample arm fiber is focused into the specimen being measured. Light retroreflected from tissue structures is combined in the fiber-optic beamsplitter (50/50) with light from a scanning reference mirror. Interference occurs at the detector only when the distance of the reflection from the sample is matched to the length of the reference arm to within the coherence length of the source. A longitudinal scan of the sample is then performed by scanning the reference mirror position and simultaneously recording the interferometric signal. The interferometric signal is demodulated using band pass filtering and envelope detection. The signal is then digitized and stored on a computer. To acquire data for a two-dimensional image, a series of longitudinal scans are performed with the optical beam position translated laterally between scans. The data set is then displayed as either a false-color or gray-scale image.

The longitudinal resolution of an OCT image is determined by the coherence length of the light source. For a light source having a Gaussian spectrum, the coherence length $l_c = (\sqrt{2\ln(2)/\pi})\lambda^2/\Delta\lambda$, where λ and $\Delta\lambda$ are the center wavelength and the FWHM spectral bandwidth, respectively [7]. This is the expression for the coherence length used throughout this thesis. Other definitions of the coherence length than the one used here and in Ref.[7] yield similar expressions [8]. The first OCT system had a longitudinal resolution of 17 μm in air [1].

The lateral resolution of an OCT image is determined by the spot size of the sample beam at the depth being probed in the tissue. In a random medium like tissue, it is necessary to take the scattering of the light into account when determining the spot size.

Since the development of the first OCT system [1] described above, a lot of effort has been put into the improvement of the system. Regarding a system based on the original concept, the main focus areas have been: the light source, the interferometer, and the beam scanning optics. A comprehensive review of the progress within these areas is given in Ref. [9].

A superluminescent diode, as used in the first OCT system, comes close to being the ideal source for OCT imaging due to the high irradiance and relatively low cost. However, the coherence length of SLD's, which is typically $10 - 20\,\mu$m, is insufficient to image individual cells or subcellular structures such as nuclei in tissue. The highest longitudinal resolution OCT achieved to date was, according to the

author's knowledge, obtained by using a femtosecond Ti:sapphire laser [10]. Using this source, *in vivo* subcellular imaging with longitudinal resolution of $\sim 1\,\mu$m was demonstrated [11]. Femtosecond lasers are not, however, without limitations as sources for OCT. The cost, complexity, and environmental instability of these lasers make their clinical application cumbersome.

In addition to a higher irradiance of the light source, other interferometer configurations than the conventional Michelson interferometer may also lead to an improved signal-to-noise ratio (SNR). By using interferometers with balanced detection, the intensity noise of the light is suppressed [12]. The choice of a balanced OCT configuration versus an unbalanced OCT configuration with optimized reference-arm attenuation has been investigated [13]. Moreover, a family of power-conserving fiber-optic interferometer designs have been introduced that use optical circulators, unbalanced couplers, and (or) balanced detection [14], [15].

In the first OCT system [1], a stepper motor stage was used to scan the reference mirror. Since then, several techniques have been applied in the attempt to make the image acquisition faster. Real time *in vivo* imaging has recently been demonstrated [16]. The reference scanning was performed by using a delay line in the reference arm that was developed for femtosecond pulse shaping [17],[18], and recently applied to OCT [19],[20]. It is important to note that faster image acquisition requires detection electronics with broader bandwidth, thus decreasing the SNR.

The most advanved clinical applications of OCT to date have been for non-invasive, high-resolution imaging of intraocular structures [21],[22],[23]. Ophthalmic OCT imaging studies have demonstrated significant potential for routine clinical examinations of the anterior eye, crystalline lens, and retina. A specialized version of OCT for retinal examination has been commercialized and several thousand patients have been examined using this method (Humphrey Systems, Dublin, CA). Sub-surface OCT imaging in highly scattering tissues is a topic of considerable current interest. Optical imaging in non-transparent biological tissues is, in general, a difficult problem, primarily due to the scattering of the tissue. The attractive spectral region for OCT imaging in non-transparent biological tissues is near $1.3\,\mu$m, where light scattering is low relative to scattering of light in the visible region, and the tissue absorption is low. In this wavelength region near $1.3\,\mu$m, several investigators have demonstrated imaging up to 2-3 mm deep in the tissue, dependent on the tissue type examined [24], [25]. For a review of the biomedical and clinical applications of OCT, the reader is referred to Ref. [25].

1.1 Scope of the thesis

Mathematical models have been developed to promote understanding of the OCT imaging process and thereby enable development of better imaging instrumentation and data processing algorithms. One of the most important issues in the modeling of OCT systems is the role of the multiple scattered photons, an issue, which up to now is not yet fully understood. The scope of this thesis is the development of a model that is able to describe the performance of the OCT system in both the single and multiple scattering regimes simultaneously. Such a model, where the contribution to the OCT signal from multiple scattered photons has been taken into account together with multiple scattering effects, is essential in the calculation of the SNR of the OCT system. A determination of the lateral resolution of the OCT system at arbitrary depths in the scattering tissue is also made possible by such a model. Another important aspect of the thesis is an experimental verification of the model carried out using phantoms with optical properties typical for tissue.

1.2 Organization of the thesis

In chapter 2 of this thesis, a new analytical model is presented where the contribution to the OCT signal from multiple scattered photons has been taken into account. This model inherently includes the *shower curtain effect*, well-known for light propagation through the atmosphere [26],[27]. This effect has been omitted in previous theoretical models of OCT systems. It is demonstrated in this thesis that the shower curtain effect is of utmost importance in the theoretical description of an OCT system. The analytical model, together with a proper noise analysis of the OCT system, enables a calculation of the SNR, where the optical properties of the tissue have been taken into account. Moreover, by using the model, it is possible to determine the lateral resolution of the OCT system at arbitrary depths in the scattering tissue. An experimental verification of the new OCT model is presented in chapter 3 of the thesis.

The main part of chapter 4 is devoted to a demonstration of the imaging capabilities of the OCT system, which has been developed during the Ph.D. thesis project. The last section in that chapter deals with a novel *true-reflection OCT imaging algorithm*, which is based on the new OCT model presented in this thesis.

Finally, in chapter 5, a theoretical analysis of the Wigner phase-space distribution function for the OCT geometry is presented. As in the new OCT model, multiple scattered photons has been taken into account together with multiple scattering effects. The fundamental difference of measuring the Wigner phase-space distribution and the OCT signal is discussed. Furthermore, a novel method of creating images based on measurements of the momentum width of the Wigner phase-space distribution is presented, and compared with conventional OCT.

2 Modeling optical coherence tomography systems

2.1 Introduction

Since the first paper describing the use of the optical coherence tomography (OCT) technique for noninvasive cross-sectional imaging in biological systems [1], various theoretical models of the OCT system have been developed. The primary motivation has been optimization of the OCT technique based on these models thereby improving the imaging capabilities. The first theoretical models were based on single-scattering theory [28, 29]. These models are restricted to superficial layers of highly scattering tissue in which only single scattering occurs. Single scattering or single backscattering refer to photons which do not undergo scattering either to or from the backscattering plane of interest, i.e., ballistic photons. However, at larger probing depths, the light is also subject to multiple scattering. The effects of multiple scattering have been investigated on an experimental basis [30], and by using a hybrid Monte Carlo/analytical model [31], analysis methods of linear systems theory [32], a model based on the extended Huygens-Fresnel principle [33], and Monte Carlo simulations [34]. As shown by these investigations, the primary effects of multiple scattering are a reduction of the imaging contrast and resolution of the OCT system, and a less steep slope of the signal intensity depth profile than the slope given by the single-backscatter model [30, 32].

2.2 Analytical OCT model based on the extended Huygens-Fresnel principle

In this section, a new theoretical description [35],[36],[37],[38],[39] of the OCT technique when used for imaging in highly scattering tissue is presented. The description is based on the extended Huygens-Fresnel principle. It is shown that the theoretical model, based on this principle and the use of mutual coherence functions, describes the performance of the OCT system in both the single and multiple scattering regimes simultaneously. In a standard OCT system [1] with diffuse backscattering from the tissue discontinuity being probed, and a distance between the focusing lens and the tissue, the so-called shower curtain effect [26],[27] is present. This effect has been omitted in previous theoretical models [33]. However, it is demonstrated in this section that inclusion of this effect is of utmost importance in the theoretical description of an OCT system.

The extended Huygens-Fresnel principle

When an optical wave propagates through a random medium, e.g. tissue, both the amplitude and phase of the electric field experience random fluctuations caused by small random changes in the index of refraction. Several different theoretical approaches have been developed for describing these random amplitude and phase fluctuations, based upon solving the wave equation for the electric field of the wave or for the various statistical moments of the field.

By assuming a sinusoidal time variation in the electric field, it has been shown [40],[41],[42],[43] that Maxwell's equations for the vector amplitude $\vec{E}(\vec{R})$ of a propagating electromagnetic wave through a nonabsorbing refracting medium lead directly to

$$\nabla^2 \vec{E} + k^2 n^2(\vec{R})\vec{E} + 2\nabla[\vec{E} \cdot \nabla \ln n(\vec{R})] = 0, \tag{1}$$

where $\vec{R}$ denotes a point in space, k is the wave number of the electromagnetic wave, and $n(\vec{R})$ is the index of refraction whose time variations have been suppressed. We now assume that the magnitude of the index of refraction fluctuations is small in comparison with unity. This means, that the index of refraction $n(\vec{R}) = \left\langle n(\vec{R}) \right\rangle + n_{\mathrm{f}}(\vec{R})$, where $n_{\mathrm{f}}(\vec{R})$ is the small fluctuating part of the index of refraction with zero mean and a root-mean-square value much less than unity. This assumption is in general valid for tissue [44]. In this case it has been shown, that the last term on the left-hand side of Eq. (1), which is related to the change in polarization of the wave as it propagates, is negligible if the wavelength of the radiation $\lambda \ll 2\pi l_0$, where l_0 is a measure of the smallest random inhomogeneities in the medium [42],[43]. The structures that dominate light propagation in tissue, for example the cells, have a size of $2\,\mu$m or more, which means that the criteria for neglecting the depolarization term is fulfilled in the case of interest where $\lambda \simeq 1.0\,\mu$m. By dropping this term, Eq. (1) simplifies to

$$\nabla^2 \vec{E} + k^2 n^2(\vec{R}) \vec{E} = 0, \tag{2}$$

which is now easily decomposed into three scalar equations, one for each component of the field $\vec{E}$. If we let $U(\vec{R})$ denote one of the scalar components that is transverse to the direction of propagation along the positive z-axis, then Eq. (2) may be replaced by the scalar stochastic equation

$$\nabla^2 U + k^2 n^2(\vec{R}) U = 0. \tag{3}$$

Equation (3) cannot be solved exactly in closed form. Some early attempts to solve Eq. (3) were based on the geometric optics approximation [45], which ignores diffraction effects, and on perturbation theories widely known as the Born approximation and Rytov approximation [41].

One approach to solving Eq. (3) by other than perturbation methods was developed, independent of each other, in the United States by Lutomirski and Yura [46] and in the former Soviet Union by Feizulin and Kravtsov [47]. This technique is called the extended Huygens-Fresnel principle. As the name indicates, it is an extension of the Huygens-Fresnel principle to a medium that exhibits a random spatial variation in the index of refraction. That is, the field due to some arbitrary complex disturbance specified over an aperture can be computed, for propagation distances that are large compared with the size of the aperture, by superimposing spherical wavelets that radiate from all elements of the aperture.

This principle follows directly from Green's theorem [48] and the Kirchhoff approximation [48] applied to the scalar wave equation together with a field reciprocity theorem between an observation point and a source point of spherical waves in the random medium. On the basis of this principle, the geometry of the problem, i.e., the aperture field distribution, can be separated from the propagation problem, which is determined by the way a spherical wave propagates through the medium. Furthermore, Yura and Hanson [49],[50] have applied the extended Huygens-Fresnel principle to paraxial wave propagation through an arbitrary $ABCD$ system in the presence of random inhomogeneities. An arbitrary $ABCD$ system refers to an optical system that can be described by an $ABCD$ ray-transfer matrix [51]. In the cases of interest in this thesis, the $ABCD$ ray-transfer matrix is real, and the field in the output plane is then given by [49]

$$U(\vec{r}) = \int U_0(\vec{p})\, G(\vec{p}, \vec{r})\, d\vec{p}, \tag{4}$$

where $\vec{r}$ and $\vec{p}$ are two-dimensional vectors transverse to the optical axis in the output plane and input plane, respectively. The quantity $U_0(\vec{p})$ is the field in

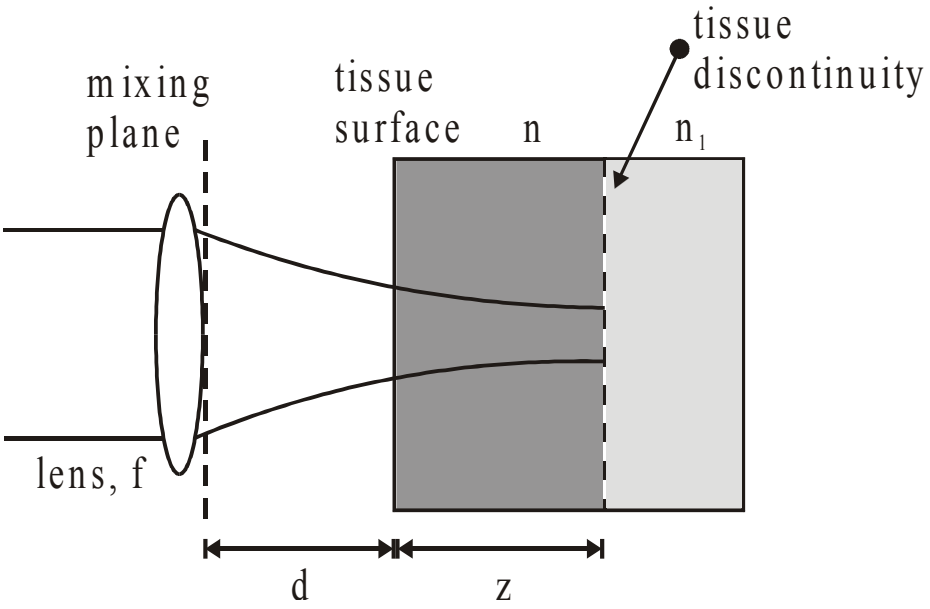

Figure 1. The sample arm geometry of the OCT system.

the input plane, and $G(\vec{p},\vec{r})$ is the extended Huygens-Fresnel Green's function response at $\vec{r}$ due to a point source at $\vec{p}$, which is given by [46],[49]

$$G(\vec{p},\vec{r}) = G_0(\vec{p},\vec{r}) \exp\left[i\phi(\vec{p},\vec{r})\right], \tag{5}$$

where $G_0(\vec{p},\vec{r})$ is the Huygens-Fresnel Green's function for propagation through an $ABCD$ system in the absence of random inhomogeneities, and $\phi(\vec{p},\vec{r})$ is the random phase of a spherical wave propagating in the random medium from the input plane to the output plane. The Huygens-Fresnel Green's function $G_0(\vec{p},\vec{r})$ is given by [49]

$$G_0(\vec{p},\vec{r}) = -\frac{ik}{2\pi B} \exp\left[-\frac{ik}{2B}\left(Ap^2 - 2\vec{p}\cdot\vec{r} + Dr^2\right)\right], \tag{6}$$

where A, B, and D are the ray-matrix elements for propagation from the input plane to the output plane. In the following, it is assumed that ϕ is a normally distributed zero-mean random process.

The OCT signal

A conventional OCT system [1] consists of a superluminescent diode (SLD), a Michelson interferometer with movable reference mirror, and a photodetector. The rotationally symmetric sample arm geometry of the OCT system is shown in Fig. 1. The tissue discontinuity being probed arises from a refractive index discontinuity between two tissue layers ($n \neq n_1$ in Fig. 1). Therefore, the discontinuity, placed at a depth z in the tissue, is characterized by a Fresnel reflection coefficient R_{d}. A lens with focal length f is placed at a distance d from the tissue surface. In the system of interest, the focal plane coincides with the tissue discontinuity. Furthermore, the reference arm optical path length in the Michelson interferometer is matched to the focal plane optical depth.

In the case of human skin, light scattering in the bulk tissue is predominantly in the forward direction for the wavelengths of interest in the NIR region [52]. Hence, we neglect bulk backscattering, and use the extended Huygens-Fresnel principle [46],[47] to describe the light propagation in the bulk tissue. This is

justified by the fact that the extended Huygens-Fresnel principle is based on the paraxial approximation and therefore valid for small-angle forward scattering. In particular, it can be shown that the paraxial approximation is valid up to 30°(i.e., 0.5 rad) [51]. Because most tissues are characterized by rms scattering angles below this limit, the extended Huygens-Fresnel principle may be used to describe light propagation in tissue retaining both amplitude and phase information. The bulk tissue absorption is neglected [52]. Thus, the bulk tissue is characterized by a scattering coefficient μ_{s}, a root mean square scattering angle θ_{rms} or asymmetry parameter g [53], and a mean index of refraction n. Furthermore, the bulk tissue is modeled as a material with scatterers randomly distributed over the volume of interest. Note, that in the present analysis polarization effects are not included.

By mixing the sample field, U_{S}, reflected at the discontinuity in the tissue at depth z, with the reference field, U_{R} , on the photodetector of the OCT system, we obtain that the heterodyne signal current $i\left(z\right)$ can be expressed as [33]

$$i\left(z\right) \propto \mathrm{Re}\left[\int U_{\mathrm{R}}\left(\vec{p},t\right) U_{\mathrm{S}}^{*}\left(\vec{p},t+\tau\right) d\vec{p}\right], \tag{7}$$

where the integration is taken over the area of the photodetector, Re denotes the real part, and τ is the difference between the propagation times of the reference and sample beams. In practice, the heterodyne signal current $i\left(z\right)$ is measured over a time much longer than the source coherence time. In this case, it can be shown that [33]

$$i\left(z\right) \propto \left|g\left(\tau\right)\right| \mathrm{Re}\left[\int U_{\mathrm{R}}\left(\vec{p}\right) U_{\mathrm{S}}^{*}\left(\vec{p}\right) d\vec{p}\right], \tag{8}$$

where $\left|g\left(\tau\right)\right|$ is the modulus of the normalized temporal coherence function of the source.

Because the detailed structure of the tissue is unknown *a priori*, it is necessary and appropriate to treat the optical distortions as a random process and, as is commonly done in the literature, to specify certain measures of the average performance, e.g., the mean (i.e., ensemble average) square heterodyne signal current. It can be shown that the mean square heterodyne signal current $\left\langle i^{2}\left(z\right)\right\rangle$, which is proportional to the heterodyne signal power, is given by [33, 26]

$$\left\langle i^{2}\left(z\right)\right\rangle = 2\alpha^{2}\left|g\left(\tau\right)\right|^{2} \mathrm{Re}\left[\iint \Gamma_{\mathrm{S}}(\vec{p}_{1},\vec{p}_{2};z)\,\Gamma_{\mathrm{R}}\left(\vec{p}_{1},\vec{p}_{2}\right) d\vec{p}_{1} d\vec{p}_{2}\right], \tag{9}$$

where

$$\Gamma_{\mathrm{R}}\left(\vec{p}_{1},\vec{p}_{2}\right) = U_{\mathrm{R}}\left(\vec{p}_{1}\right) U_{\mathrm{R}}^{*}\left(\vec{p}_{2}\right) \tag{10}$$

$$\Gamma_{\mathrm{S}}\left(\vec{p}_{1},\vec{p}_{2};z\right) = \left\langle U_{\mathrm{S}}\left(\vec{p}_{1};z\right) U_{\mathrm{S}}^{*}\left(\vec{p}_{2};z\right)\right\rangle \tag{11}$$

are the mutual coherence functions of the reference and the reflected sample optical fields in the mixing plane. The angular brackets denote an ensemble average both over the statistical properties of the tissue and the reflecting discontinuity, which are assumed to be statistically independent. For simplicity, the heterodyne mixing process has been chosen to take place directly behind the lens at the side facing the tissue, and $\vec{p}_{1},\vec{p}_{2},\vec{p}$ are two-dimensional vectors in this plane transverse to the optical axis. The quantity α is a conversion factor for power to current and equals $q_{\mathrm{e}}\eta/h\nu$, where q_{e} is the electronic charge, η is the detector quantum efficiency, ν is the optical frequency, and h is Planck's constant. In the case of interest, the reference arm optical path length in the Michelson interferometer is always matched to the sample arm optical path length, from which it follows that $\left|g\left(\tau\right)\right| = \left|g\left(0\right)\right| = 1$ [33].

For the heterodyne detection scheme, the spatial coherence properties of the sample field contained in the mutual coherence function Γ_{S} are of utmost importance in the determination of the corresponding signal. In particular, if the spatial coherence of the sample field is degraded with respect to the reference field, one obtains a corresponding degradation in the signal-to-noise ratio.

The reference field and the input sample field, U_{Si} , in the lens plane are assumed to be of Gaussian shape and given by

$$U_{\mathrm{R}}\left(\vec{p},t\right) = \sqrt{\frac{P_{\mathrm{R}}}{\pi w_0^2}}\exp\left[-\frac{p^2}{2}\left(\frac{1}{w_0^2}+\frac{ik}{f}\right)\right]\exp\left[i\omega_{\mathrm{R}}t+\phi_{\mathrm{R}}\left(t\right)\right] \tag{12}$$

$$U_{\mathrm{Si}}\left(\vec{p},t\right) = \sqrt{\frac{P_{\mathrm{S}}}{\pi w_0^2}}\exp\left[-\frac{p^2}{2}\left(\frac{1}{w_0^2}+\frac{ik}{f}\right)\right]\exp\left[i\omega_{\mathrm{S}}t\right], \tag{13}$$

where P_{R} and P_{S} are the powers of the reference and input sample beams, respectively, w_0 is the $1/e$ intensity radius of these beams in the lens plane, $k=2\pi/\lambda$, where λ is the center wavelength of the source in vacuum, ω_{R} and ω_{S} are the angular frequencies of the reference and input sample beams, respectively, and ϕ_{R} is the phase of the reference field relative to the input sample field.

In the determination of the mutual coherence function Γ_{S}, we use the extended Huygens-Fresnel principle to obtain a viable expression for $U_{\mathrm{S}}\left(\vec{p};z\right)$, i.e., the reflected sample optical field in the mixing plane. Using Eq. (4), we have

$$U_{\mathrm{S}}\left(\vec{p};z\right)=\int U_{\mathrm{B}}\left(\vec{r};z\right)G\left(\vec{r},\vec{p};z\right)d\vec{r}, \tag{14}$$

where $U_{\mathrm{B}}\left(\vec{r};z\right)$ is the reflected sample field in the plane of the tissue discontinuity, $\vec{r},\vec{r}_1,\vec{r}_2$ are two-dimensional vectors in this plane transverse to the optical axis, and $G\left(\vec{r},\vec{p};z\right)$ is the extended Huygens-Fresnel Green's function response at $\vec{p}$ due to a point source at $\vec{r}$, which includes the effects of scattering in the intervening medium. Combining Eqs. (11) and (14) yields

$$\Gamma_{\mathrm{S}}\left(\vec{p}_1,\vec{p}_2;z\right)=\iint\left\langle U_{\mathrm{B}}\left(\vec{r}_1;z\right)U_{\mathrm{B}}^{*}\left(\vec{r}_2;z\right)G\left(\vec{r}_1,\vec{p}_1;z\right)G^{*}\left(\vec{r}_2,\vec{p}_2;z\right)\right\rangle d\vec{r}_1d\vec{r}_2. \tag{15}$$

For simplicity in notation, we omit in the following the explicit dependence of the various quantities on z.

We next assume that the statistical properties of the bulk tissue and the tissue discontinuity are independent, and that the propagation to the tissue discontinuity is statistically independent from the corresponding reflected propagation path. The former seems to be a reasonable assumption for a medium like tissue. The latter means that enhanced backscattering is neglected. The criteria for neglecting enhanced backscattering is discussed in section 5.2. From these assumptions it follows that

$$\begin{aligned}\left\langle U_{\mathrm{B}}\left(\vec{r}_1\right)U_{\mathrm{B}}^{*}\left(\vec{r}_2\right)G\left(\vec{r}_1,\vec{p}_1\right)G^{*}\left(\vec{r}_2,\vec{p}_2\right)\right\rangle &= \left\langle U_{\mathrm{B}}\left(\vec{r}_1\right)U_{\mathrm{B}}^{*}\left(\vec{r}_2\right)\right\rangle\times\\ &\quad\left\langle G\left(\vec{r}_1,\vec{p}_1\right)G^{*}\left(\vec{r}_2,\vec{p}_2\right)\right\rangle.\end{aligned} \tag{16}$$

The first term on the right hand side of Eq. (16) relates to both the mean value over statistics of the bulk tissue in propagating from the lens plane to the tissue discontinuity, and the reflection statistics of the discontinuity. The second term on the right hand side of Eq. (16) relates to the corresponding average over the statistics of the bulk tissue when propagating back from the discontinuity to the mixing plane.

Assuming diffuse backscattering from the tissue discontinuity, we have [26, 54]

$$\left\langle U_{\mathrm{B}}\left(\vec{r}_1\right)U_{\mathrm{B}}^{*}\left(\vec{r}_2\right)\right\rangle=\frac{4\pi}{k^2}\delta\left(\vec{r}_1-\vec{r}_2\right)\left\langle I_{\mathrm{B}}\left(\vec{r}_1\right)\right\rangle, \tag{17}$$

where $\delta(\vec{r})$ is the two-dimensional Dirac delta function, and $\langle I_{\mathrm{B}}(\vec{r}_1)\rangle$ is the mean backscattered irradiance distribution in the plane of the discontinuity. An adequate analytic approximation for this mean backscattered irradiance distribution is obtained by multiplying the approximate expression for the mean irradiance distribution, derived in the section "The lateral resolution" in chapter 2, by the reflection coefficient R_{d}. The expression, which is valid for arbitrary values of the optical depth $\mu_{\mathrm{s}}z$, is given by

$$\langle I_{\mathrm{B}}(\vec{r})\rangle = \frac{R_{\mathrm{d}}P_{\mathrm{S}}}{\pi}\left[\frac{e^{-\mu_{\mathrm{s}}z}\exp\left[-r^2/w_{\mathrm{H}}^2\right]}{w_{\mathrm{H}}^2} + \frac{(1-e^{-\mu_{\mathrm{s}}z})\exp\left[-r^2/w_{\mathrm{S}}^2\right]}{w_{\mathrm{S}}^2}\right]. \quad (18)$$

The first term in the brackets on the right hand side of Eq. (18) can be interpreted to represent the attenuated distribution obtained in the absence of the inhomogeneities, and the corresponding second term represents a broader halo resulting from scattering by the inhomogeneities. The quantities w_{H} and w_{S} are the $1/e$ irradiance radii or spot sizes in the discontinuity plane in the absence and presence of scattering, respectively, given by

$$w_{\mathrm{H}}^2 = w_0^2\left(A-\frac{B}{f}\right)^2 + \left(\frac{B}{kw_0}\right)^2 \quad (19)$$

$$w_{\mathrm{S}}^2 = w_0^2\left(A-\frac{B}{f}\right)^2 + \left(\frac{B}{kw_0}\right)^2 + \left(\frac{2B}{k\rho_0}\right)^2. \quad (20)$$

A and B are the ray-matrix elements for propagation from the lens plane to the discontinuity plane. For the geometry of interest, A and B are given by $A=1$ and $B=f=d+z/n$ [51]. The quantity ρ_0 appearing in Eq. (20) is the lateral coherence length of a spherical wave in the lens plane due to a point source in the discontinuity plane [26]. The lateral coherence length is discussed in detail below, see also Appendix A.

Combining Eqs. (15)–(17) and simplifying yields

$$\Gamma_{\mathrm{S}}(\vec{p}_1,\vec{p}_2) = \frac{4\pi}{k^2}\int \langle I_{\mathrm{B}}(\vec{r})\rangle \langle G(\vec{r},\vec{p}_1)\,G^*(\vec{r},\vec{p}_2)\rangle\, d\vec{r}. \quad (21)$$

Using Eq. (5), the second term in the integral on the right-hand side of Eq. (21) may be written as

$$\langle G(\vec{r},\vec{p}_1)\,G^*(\vec{r},\vec{p}_2)\rangle = G_0(\vec{r},\vec{p}_1)\,G_0^*(\vec{r},\vec{p}_2)\,\Gamma_{\mathrm{pt}}, \quad (22)$$

where $G_0(\vec{r},\vec{p})$ is the Huygens-Fresnel Green's function when propagating from the discontinuity plane to the lens plane, and Γ_{pt} is the mutual coherence function of a point source located in the discontinuity plane and observed in the lens plane, which is given by

$$\Gamma_{\mathrm{pt}} = \langle \exp\left[i\left(\phi(\vec{p}_1)-\phi(\vec{p}_2)\right)\right]\rangle. \quad (23)$$

The mutual coherence function Γ_{pt} contains the effects of the scattering inhomogeneities. Using Eq. (6), the Green's function $G_0(\vec{r},\vec{p})$ is given by

$$G_0(\vec{r},\vec{p}) = -\frac{ik}{2\pi B_{\mathrm{b}}}\exp\left[-\frac{ik}{2B_{\mathrm{b}}}\left(A_{\mathrm{b}}r^2 - 2\vec{r}\cdot\vec{p} + D_{\mathrm{b}}p^2\right)\right], \quad (24)$$

where A_{b}, B_{b}, and D_{b} are the ray-matrix elements for backpropagation to the lens plane. These quantities are given by: $A_{\mathrm{b}}=D=1$, $B_{\mathrm{b}}=B=d+z/n$, and $D_{\mathrm{b}}=A=1$ [49]. In order to obtain an analytical solution, we have to use an approximate expression for the mutual coherence function Γ_{pt}. The expression, which is derived in the section "The lateral resolution" in chapter 2, is given by

$$\Gamma_{\mathrm{pt}}(\rho) \simeq e^{-\mu_{\mathrm{s}}z} + (1-e^{-\mu_{\mathrm{s}}z})\exp\left[-\rho^2/\rho_0^2\right], \quad (25)$$

where $\rho = |\vec{p}_1 - \vec{p}_2|$.

Substituting Eqs. (10), (12), (18), (21), (22), (24), and (25) into Eq. (9) and performing the indicated Gaussian integrations over $\vec{p}_1, \vec{p}_2$, and simplifying yields

$$\left\langle i^2(z)\right\rangle = \frac{2\alpha^2 P_{\mathrm{R}} P_{\mathrm{S}} \sigma_{\mathrm{b}}}{\pi^2} \times \int \left[\frac{e^{-\mu_{\mathrm{s}} z} \exp\left[-r^2/w_{\mathrm{H}}^2\right]}{w_{\mathrm{H}}^2} + \frac{(1 - e^{-\mu_{\mathrm{s}} z}) \exp\left[-r^2/w_{\mathrm{S}}^2\right]}{w_{\mathrm{S}}^2} \right]^2 d\vec{r}, \quad (26)$$

where the effective backscattering cross section of the tissue discontinuity $\sigma_{\mathrm{b}} = 4\pi R_{\mathrm{d}}/k^2$. It is important to note that the algebraically simple result given in Eq. (26) are, strictly speaking, valid only for propagation geometries where $A = D$, as is obtained in the case of interest. Performing the integration over the discontinuity plane in Eq. (26) and simplifying, we obtain the following expression for the mean square heterodyne signal current

$$\begin{aligned} \left\langle i^2(z)\right\rangle &= \frac{\alpha^2 P_{\mathrm{R}} P_{\mathrm{S}} \sigma_{\mathrm{b}}}{\pi w_{\mathrm{H}}^2} \left[e^{-2\mu_{\mathrm{s}} z} + \frac{2e^{-\mu_{\mathrm{s}} z}(1 - e^{-\mu_{\mathrm{s}} z})}{1 + w_{\mathrm{S}}^2/w_{\mathrm{H}}^2} + \left(1 - e^{-\mu_{\mathrm{s}} z}\right)^2 \frac{w_{\mathrm{H}}^2}{w_{\mathrm{S}}^2} \right] \\ &\equiv \left\langle i^2 \right\rangle_0 \Psi(z). \end{aligned} \quad (27)$$

The quantity $\left\langle i^2 \right\rangle_0 = \alpha^2 P_{\mathrm{R}} P_{\mathrm{S}} \sigma_{\mathrm{b}} / \pi w_{\mathrm{H}}^2$ is the mean square heterodyne signal current in the absence of scattering, and the terms contained in the brackets is the heterodyne efficiency factor $\Psi(z)$. A comparison between the analytic approximation of the heterodyne efficiency factor, given in Eq. (27), and the exact numerical calculation is given in Appendix B.

Physically, $\Psi(z)$ can be looked upon as the reduction in the heterodyne signal-to-noise ratio due to the scattering of the tissue. The first term in the brackets of Eq. (27) represents the contribution due to single scattering. The corresponding third term is the multiple scattering term, and the second term is the cross term. Physically, the cross term is the coherent mixing of the unscattered and the multiple scattered light.

When the focal plane coincides with the tissue discontinuity (i.e., $fA = B$), we obtain

$$w_{\mathrm{H}}^2 = \left(\frac{f}{k w_0}\right)^2; \qquad \frac{w_{\mathrm{H}}^2}{w_{\mathrm{S}}^2} = \frac{1}{1 + \left(\frac{2w_0}{\rho_0(z)}\right)^2}. \quad (28)$$

The quantity $\rho_0(z)$ is the lateral coherence length of the reflected sample field in the mixing plane. For lateral separations much less (greater) than $\rho_0(z)$, the field can be considered to be mutually coherent (incoherent). Because of the diffuse backscattering from the tissue discontinuity, $\rho_0(z)$ is determined only by the propagation back through the tissue from the tissue discontinuity to the mixing plane. As a consequence, $\rho_0(z)$ is the lateral coherence length of a point source located in the tissue discontinuity plane, as observed in the mixing plane. For the geometry of interest, it is shown in Appendix A that

$$\rho_0(z) = \sqrt{\frac{3}{\mu_{\mathrm{s}} z}} \frac{\lambda}{\pi \theta_{\mathrm{rms}}} \left(1 + \frac{n d(z)}{z}\right), \quad (29)$$

where $d(z) = f - (z/n)$, and $\theta_{\mathrm{rms}} \simeq \sqrt{2(1-g)}$. The second term in the brackets of Eq. (29) indicates, that the lateral coherence length increases with increasing distance between the tissue surface and the mixing plane. This well-known dependence of the lateral coherence length on the position of the scattering medium relative to the observation plane, is the so-called shower curtain effect [26, 27].

In general, the shower curtain effect implies that the lateral coherence length obtained for the case when the scattering medium is close to the radiation source

is larger than the case when the scattering medium is close to the observation plane. Physically, this is due to the fact that a distorted spherical wave approaches a plane wave as it further propagates through a non-scattering medium. As a consequence, e.g., one can see a person immediately behind a shower curtain, but the person cannot see you. The effect is well-known for light propagation through the atmosphere as discussed by Dror et al. [27], but has been omitted in previous theoretical OCT models [33]. However, due to the finite distance between the focusing lens and the tissue, the effect is inevitably present in practical OCT systems and could facilitate system optimization.

The reflection characteristics of the tissue discontinuity play a vital role for the shower curtain effect. If we, instead of diffuse backscattering, had a specular reflection at the tissue discontinuity, the corresponding inhomogeneous mutual coherence function for plane waves would apply. Using this mutual coherence function, we have [55]

$$\Psi(z) = \left[e^{-2\mu_s z} + \left(1 - e^{-2\mu_s z}\right) \frac{w_H^2}{w_S^2} \right] \tag{30}$$

and

$$\rho_0(z) = \sqrt{\frac{1}{2\mu_s z}} \frac{\lambda}{\pi \theta_{rms}}. \tag{31}$$

It is obvious from Eq. (31) that the shower curtain effect would not be present in the case of a specular reflection at the tissue discontinuity, in contrast to the case of diffuse backscattering. However, it is important to note that it is diffuse backscattering which actually occurs in the case of (skin) tissue.

Numerical results The heterodyne efficiency factor $\Psi(z)$ is shown as a function of depth z of the tissue discontinuity in Fig. 2 for typical parameters of human skin tissue with diffuse backscattering and the shower curtain effect included (dashed) and specular reflection (solid), respectively. For comparison, we show the case of diffuse backscattering with exclusion of the shower curtain effect (dash-dot) and the case of pure single scattering (dotted). At shallow depths single backscattering dominates. Due to multiple scattering, the slope is changed and $\Psi(z)$ becomes almost constant for three cases (curve 1–3). The important difference is, however, that the change of slope occurs at different depths. This is due to the shower curtain effect leading to an appreciable enhancement of $\Psi(z)$, and with it the heterodyne signal, which is obtained by comparing curve 1 and 2 in Fig. 2. Physically, this increase in the heterodyne signal is due to an enhanced spatial coherence of the multiple scattered light.

In Fig. 3, the heterodyne efficiency factor $\Psi(z)$ is shown as a function of depth z for $\mu_s = 10\,\mathrm{mm}^{-1}$ and three values of g within the range of validity of the extended Huygens-Fresnel principle. The curves are computed for the case of a diffuse backscattering at the discontinuity, and inclusion of the shower curtain effect. This figure demonstrates the degree of sensitivity of the heterodyne efficiency factor with respect to changes in the asymmetry parameter.

Moreover, in Fig. 4, the heterodyne efficiency factor $\Psi(z)$ is shown as a function of depth z for $g = 0.95$ and three values of μ_s within a range of interest with respect to tissue [52]. The curves are computed for the case of a diffuse backscattering at the discontinuity, and inclusion of the shower curtain effect. This figure demonstrates the degree of sensitivity of the heterodyne efficiency factor with respect to changes in the scattering coefficient.

Choice of scattering function In the present novel modeling of the OCT geometry, we use a Gaussian volume scattering function [7], as discussed in the

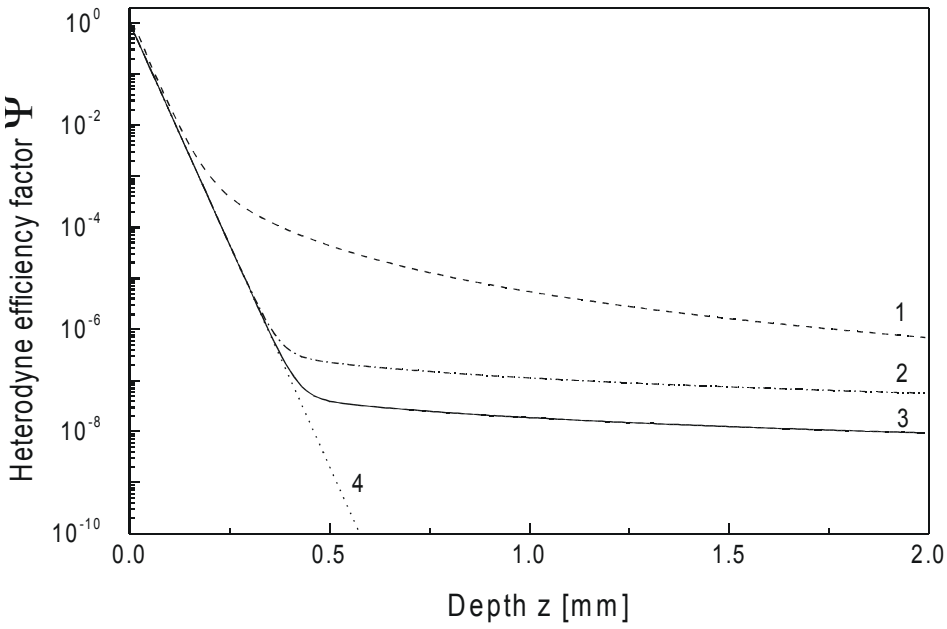

Figure 2. The heterodyne efficiency factor $\Psi(z)$ as a function of depth z for diffuse backscattering with the shower curtain effect included (curve 1), and for specular reflection (curve 3). Curve 2 is calculated for diffuse backscattering but with the shower curtain effect excluded, and curve 4 is the case of pure single backscattering ($\lambda = 814\,\mathrm{nm}$, $\mu_\mathrm{s} = 20\,\mathrm{mm}^{-1}$, $g = 0.955$ ($\theta_\mathrm{rms} = 0.3\,\mathrm{rad}$), $n = 1.4$, $f = 5\,\mathrm{mm}$, $w_0 = 0.5\,\mathrm{mm}$).

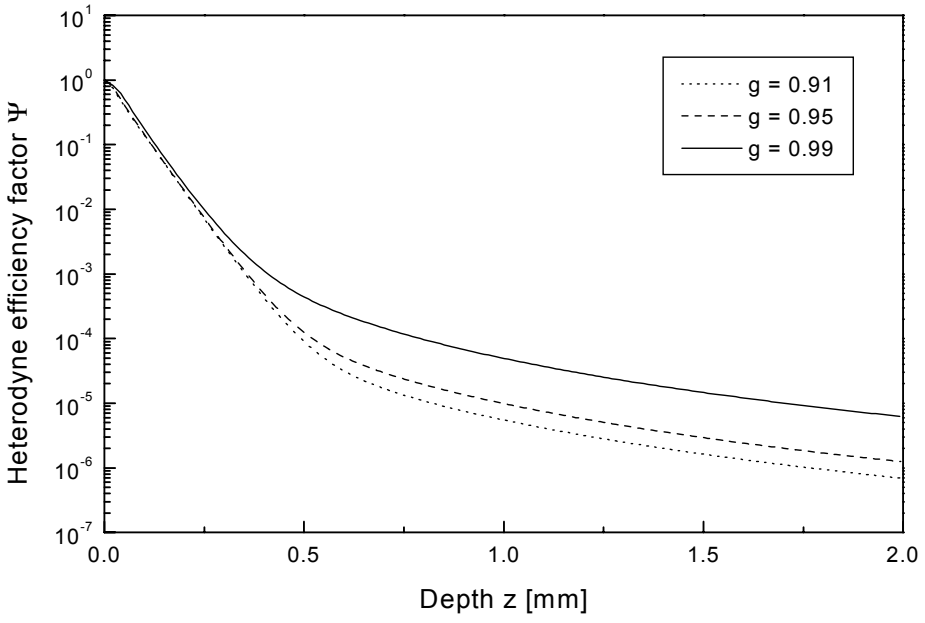

Figure 3. The heterodyne efficiency factor $\Psi(z)$ as a function of depth z for $\mu_\mathrm{s} = 10\,\mathrm{mm}^{-1}$ and three values of g within the range of validity of the extended Huygens-Fresnel principle. The curves are for the case of a diffuse backscattering at the discontinuity, and inclusion of the shower curtain effect ($\lambda = 814\,\mathrm{nm}$, $n = 1.4$, $f = 5\,\mathrm{mm}$, $w_0 = 0.5\,\mathrm{mm}$).

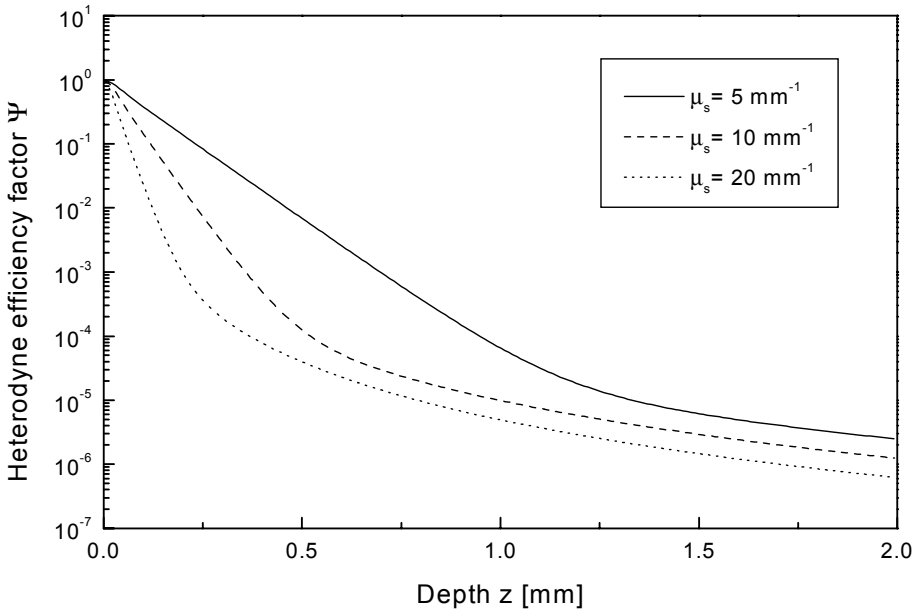

Figure 4. The heterodyne efficiency factor $\Psi(z)$ as a function of depth z for $g = 0.95$ and three values of μ_s within a range of interest with respect to tissue. The curves are for the case of a diffuse backscattering at the discontinuity, and inclusion of the shower curtain effect ($\lambda = 814\,\mathrm{nm}$, $n = 1.4$, $f = 5\,\mathrm{mm}$, $w_0 = 0.5\,\mathrm{mm}$).

section called "The lateral resolution" in chapter 2. The motivation for this choice of scattering function is the ability to obtain an accurate analytic engineering approximation, valid for all values of the optical depth. In the case of the Henyey-Greenstein scattering function [56], which has been widely used in approximating the angular scattering dependence of single-scattering events in some biological media [57],[52], the corresponding analytic approximation is not as accurate as for the case of a Gaussian scattering function. However, a numerical computation using the exact expressions may be carried out instead. Hence, both scattering functions may be used in the modeling of the OCT geometry presented in this thesis.

Signal-to-noise ratio (SNR) Without loss of generality, an OCT system with shot-noise limited operation is considered in a calculation of the signal-to-noise ratio (SNR). The only significant source of noise is the shot-noise caused by the reference beam. For a photoconductive detector the mean square noise power N_p can then be expressed as [58]

$$N_\mathrm{p} = 2\alpha q_\mathrm{e} G_\mathrm{ca}^2 R_\mathrm{l} B_\mathrm{w} P_\mathrm{R}, \tag{32}$$

where R_l is the resistance of the load, G_ca is the gain associated with the current amplifier, and B_w is the system bandwidth. The corresponding mean heterodyne signal power $S(z)$ is given by [59]

$$S(z) = \left\langle i^2(z) \right\rangle G_\mathrm{ca}^2 R_\mathrm{l}, \tag{33}$$

where $\left\langle i^2(z) \right\rangle$ is given by Eq. (27). Hence, the mean signal-to-noise ratio $SNR(z)$ is given by

$$\begin{aligned} SNR(z) &= \frac{S(z)}{N_\mathrm{p}} \\ &= (SNR)_0 \, \Psi(z), \end{aligned} \tag{34}$$

where the signal-to-noise ratio in the absence of scattering $(SNR)_0$ is given by

$$(SNR)_0 = \frac{\eta P_S}{2h\nu B_w}\left(\frac{\sigma_b}{\pi w_H^2}\right). \tag{35}$$

In the case of interest where the focal plane coincides with the tissue discontinuity, we get the following expression for $(SNR)_0$

$$(SNR)_0 = \frac{2\eta P_S}{h\nu B_w}\left(\frac{w_0}{f}\right)^2 R_d, \tag{36}$$

where it has been used that $\sigma_b = 4\pi R_d/k^2$.

The lateral resolution

As already discussed, the lateral resolution of an OCT system is determined by the spot size at the depth being probed in the tissue. Therefore, we want to determine the mean irradiance distribution or the intensity pattern of the optical field as a function of the probing depth z in the tissue. In highly scattering tissue, the mean irradiance distribution, and with it the lateral resolution, are dependent on the scattering properties of the tissue. The formalism presented in this thesis enables the calculation of the lateral resolution in highly scattering tissue, which is shown below.

For small-angle scattering, where the paraxial approximation is valid, the extended Huygens-Fresnel principle yields that the mean irradiance distribution is given by [49]

$$\langle I(\vec{r})\rangle = \left(\frac{k}{2\pi B}\right)^2 \int K(\rho)\exp\left[\frac{ik}{B}\vec{\rho}\cdot\vec{r}\right]\Gamma_{pt}(\rho)\,d^2\rho, \tag{37}$$

where

$$K(\rho) = \int \exp\left[-\frac{ikA}{B}\vec{\rho}\cdot\vec{P}\right] U_{Si}\left(\vec{P}+\vec{\rho}/2\right) U_{Si}^*\left(\vec{P}-\vec{\rho}/2\right) d^2P, \tag{38}$$

and $\vec{\rho} = \vec{p}_1 - \vec{p}_2$. For an OCT system focused at a depth z in the tissue $A = 1$, and $B = f$.

The mutual coherence function Γ_{pt} can be expressed as [54]

$$\begin{aligned}\Gamma_{pt} &= \langle\exp[i(\phi(\vec{p}_1) - \phi(\vec{p}_2))]\rangle \\ &= \exp[-s(1 - b_\phi(\rho))],\end{aligned} \tag{39}$$

where we have assumed that the phase ϕ is a normally distributed zero-mean random process. The quantity s is the phase variance, and $b_\phi(\rho)$ is the normalized phase autocorrelation function for a point source whose origin is at the probing depth z. It can be shown [60] that the phase variance $s = \mu_s z$, which is the optical depth. The normalized phase autocorrelation function $b_\phi(\rho)$ is given by [54]

$$b_\phi(\rho) = \frac{\int_0^L dz' \int_0^\infty \sigma(\theta; z') J_0(kp_s\theta)\,\theta d\theta}{\int_0^L dz' \int_0^\infty \sigma(\theta; z')\,\theta d\theta}, \tag{40}$$

J_0 is the Bessel function of the first kind, of order zero,

$$p_s = \frac{B_b(z')}{B_b}\rho, \tag{41}$$

where $B_b(z')$ is the B-matrix element for backpropagation from the probing depth z to a distance z', and $\sigma(\theta; z')$ is the volume scattering or phase function with θ being the scattering angle. For the OCT geometry $B_b(z') = z'/n$ for $0 \le z' \le z$, $L = d + z$, and $\sigma(\theta; z') = \sigma(\theta)$ for $0 \le z' \le z$, and zero otherwise. In this

model, we use a Gaussian volume scattering function, which in the small-angle approximation is given by

$$\sigma(\theta) = \exp\left[-\theta^2/\theta_0^2\right], \tag{42}$$

where $g = \langle \cos\theta \rangle \simeq 1 - \langle \theta^2 \rangle /2$, and $\theta_0 = \sqrt{\langle \theta^2 \rangle} \simeq \sqrt{2(1-g)}$.

Substituting Eqs. (41) and (42) into Eq. (40) and performing the indicated integrations yields the following equation for the normalized phase autocorrelation function

$$b_\phi(\rho) = \frac{\sqrt{\pi}}{2}\frac{\rho_\phi}{\rho}\,\mathrm{erf}\left(\rho/\rho_\phi\right), \tag{43}$$

where $\mathrm{erf}(\cdot)$ denotes the error function, and ρ_ϕ is the phase correlation length given by

$$\rho_\phi = \frac{\lambda}{\pi\sqrt{2(1-g)}}\left(1 + \frac{nd}{z}\right). \tag{44}$$

Hence, the mutual coherence function Γ_{pt} is given by Eq. (39) with $b_\phi(\rho)$ given by Eq. (43).

Thus, for specific values of both s and g, the mutual coherence function is completely determined, and for a given value of the initial optical wave function U_{Si}, numerical results for the mean irradiance can be obtained directly from Eq. (37). Here U_{Si} is given by Eq. (13), and we get the following equation for the mean irradiance distribution at the probing depth z in the tissue

$$\langle I(\vec{r}) \rangle = \frac{P_{\mathrm{S}}}{2\pi\left(f/kw_0\right)^2}\int_0^\infty \exp\left[-\frac{x^2}{4}\right] xJ_0(ux)\,\Gamma_{\mathrm{pt}}(xw_0)\,dx, \tag{45}$$

where J_0 is the Bessel function of the first kind of order zero, and

$$u = \frac{r}{f/kw_0} \tag{46}$$

is a normalized transverse coordinate.

As indicated above, numerical results can readily be obtained. However, it is useful to have an analytic approximation so that OCT system parameter studies can be performed. Examination of Eq. (39) reveals for large values of the optical depth, that Γ_{pt} is nonzero for $s(1 - b_\phi(\rho))$ less than the order unity, that is, for $b_\phi(\rho)$ near unity. Expanding $b_\phi(\rho)$ in powers of ρ and retaining the first two nonzero terms yields from Eq. (43) that $b_\phi(\rho) \simeq 1 - \rho^2/3\rho_\phi^2$, from which it follows that

$$\Gamma_{\mathrm{pt}} \simeq \exp\left[-\rho^2/\rho_0^2\right], \qquad s \gg 1 \tag{47}$$

where $\rho_0 = \sqrt{3}\rho_\phi/\sqrt{s}$. We expect that the ballistic, i.e., unscattered component of the irradiance pattern is proportional to $e^{-\mu_{\mathrm{s}} z}$. Thus, we approximate the mutual coherence function as

$$\Gamma_{\mathrm{pt}} \simeq e^{-\mu_{\mathrm{s}} z} + \left(1 - e^{-\mu_{\mathrm{s}} z}\right)\exp\left[-\rho^2/\rho_0^2\right]. \tag{48}$$

Substituting Eqs. (13) and (48) into Eq. (37), and performing the integration yields the following approximate expression for the mean irradiance distribution at the probing depth z in the tissue

$$\langle I(\vec{r}) \rangle \simeq \frac{P_{\mathrm{S}}}{\pi}\left[\frac{e^{-\mu_{\mathrm{s}} z}\exp\left[-r^2/w_{\mathrm{H}}^2\right]}{w_{\mathrm{H}}^2} + \frac{\left(1 - e^{-\mu_{\mathrm{s}} z}\right)\exp\left[-r^2/w_{\mathrm{S}}^2\right]}{w_{\mathrm{S}}^2}\right]. \tag{49}$$

The first term in the brackets on the right hand side of Eq. (49) can be interpreted to represent the attenuated distribution obtained in the absence of the inhomogeneities, and the corresponding second term represents a broader halo resulting

from scattering by the inhomogeneities. The quantities w_{H} and w_{S} are the $1/e$ irradiance radii in the absence and presence of scattering, respectively, given by

$$w_{\mathrm{H}}^2 = w_0^2\left(A-\frac{B}{f}\right)^2+\left(\frac{B}{kw_0}\right)^2 \tag{50}$$

$$w_{\mathrm{S}}^2 = w_0^2\left(A-\frac{B}{f}\right)^2+\left(\frac{B}{kw_0}\right)^2+\left(\frac{2B}{k\rho_0}\right)^2. \tag{51}$$

For the OCT system, we have

$$w_{\mathrm{H}} = \frac{f}{kw_0} \tag{52}$$

$$w_{\mathrm{S}} = \sqrt{w_{\mathrm{H}}^2+\left(\frac{2f}{k\rho_0}\right)^2}. \tag{53}$$

It is only in the very superficial layers of highly scattering tissue that it is possible to achieve diffraction limited focusing. In this region, the lateral resolution is given by $2w_{\mathrm{H}}$. At deeper probing depths the lateral resolution is dependent on the scattering properties and given by $2w_{\mathrm{S}}$. It is seen from Eqs. (53) and (29) that the lateral resolution is degraded due to multiple scattering when the probing depth is increased. This is illustrated in Fig. 5, where the intensity pattern is shown as a function of the probing depth z in the tissue using Eq. (49).

Moreover, in Fig. 6, $w_{\mathrm{S}}/w_{\mathrm{H}}$ is shown as a function of the asymmetry parameter g at $z = 0.5\,\mathrm{mm}$ for three values of the scattering coefficient. This figure demonstrates how the lateral resolution at a given depth in the tissue is degraded with decreasing asymmetry parameter, and increasing scattering coefficient.

Finally, it is important to note that the shower curtain effect leads to an increased lateral resolution.

Design considerations

The numerical aperture NA is an important design parameter of an OCT system. Thus, in this section it is shown how the heterodyne efficiency factor and the mean square heterodyne signal depend on the choice of numerical aperture.

Fig. 7 shows the heterodyne efficiency factor as a function of the focal length f, or numerical aperture NA, for the case where the $1/e$ intensity radius of the sample beam is kept fixed, the depth $z = 0.5\,\mathrm{mm}$, and the shower curtain effect is included using Eq. (29). The dashed and solid curves are calculated for the case of a low ($2\,\mathrm{mm}^{-1}$) and a high ($10\,\mathrm{mm}^{-1}$) scattering coefficient, respectively. In contrast to the case where the shower curtain effect is excluded and the heterodyne efficiency factor is constant (not shown in Fig. 7) as a function of the focal length, the two curves increase with increasing focal length (for $\mu_{\mathrm{s}} = 2\,\mathrm{mm}^{-1}$ the increase is very small). It is important to note that the slopes of the two curves are not equal. This is a consequence of the fact that the shower curtain effect is a multiple scattering effect thus playing a crucial role in a medium with a high scattering coefficient. Furthermore, it is important to note that the increase in the heterodyne efficiency factor is obtained at the expense of the lateral resolution because of a larger spot size in the discontinuity plane.

To emphasize this difference between media with a low and a high scattering coefficient, the corresponding mean square heterodyne signal current $\langle i^2\rangle$ is shown in Fig. 8 ($\mu_{\mathrm{s}} = 2\,\mathrm{mm}^{-1}$) and Fig. 9 ($\mu_{\mathrm{s}} = 10\,\mathrm{mm}^{-1}$) as a function of the focal length f, or numerical aperture NA, with (solid curve) and without (dashed curve) the shower curtain effect. For the purpose of system optimization in terms of maximum signal it is obvious from Fig. 8 and Fig. 9 that the optimal choice of

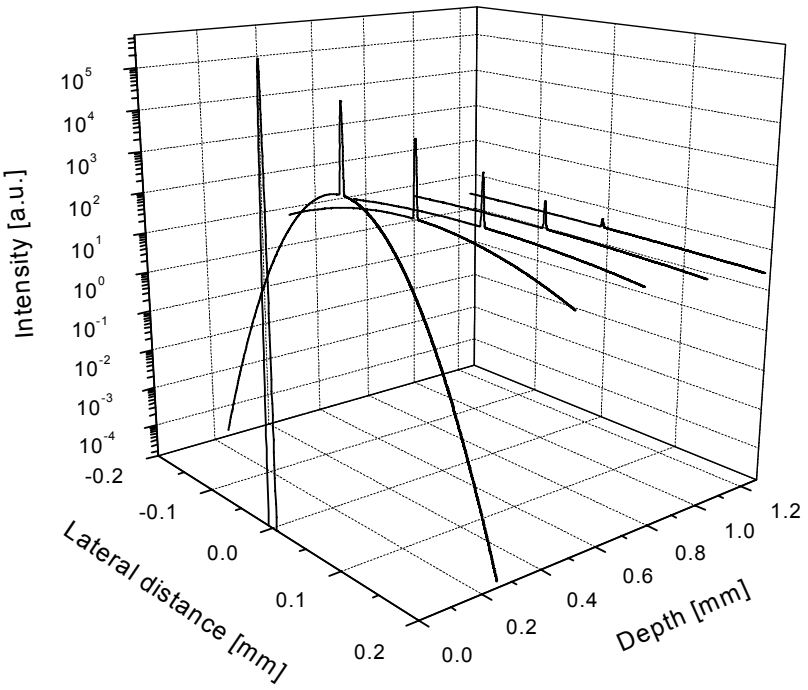

Figure 5. The intensity pattern as a function of the probing depth z in the tissue ($\lambda = 814\,\mathrm{nm}$, $\mu_\mathrm{s} = 10\,\mathrm{mm}^{-1}$, $g = 0.955$ ($\theta_\mathrm{rms} = 0.3\,\mathrm{rad}$), $n = 1.4$, $f = 5\,\mathrm{mm}$, $w_0 = 0.5\,\mathrm{mm}$).

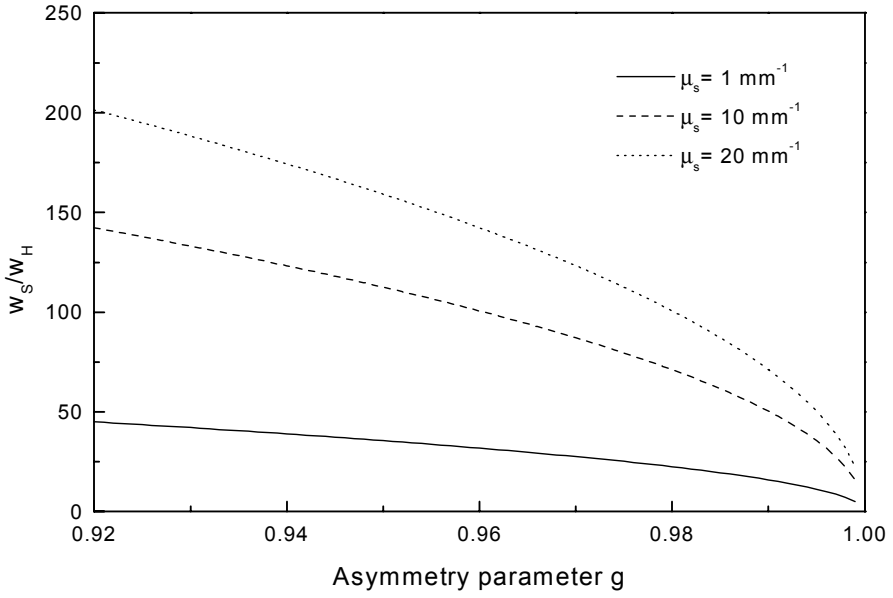

Figure 6. The ratio $w_\mathrm{S}/w_\mathrm{H}$ as a function of the asymmetry parameter g at $z =$ $0.5\,\mathrm{mm}$ for three values of the scattering coefficient ($\lambda = 814\,\mathrm{nm}$, $n = 1.4$, $f =$ $5\,\mathrm{mm}$, $w_0 = 0.5\,\mathrm{mm}$).

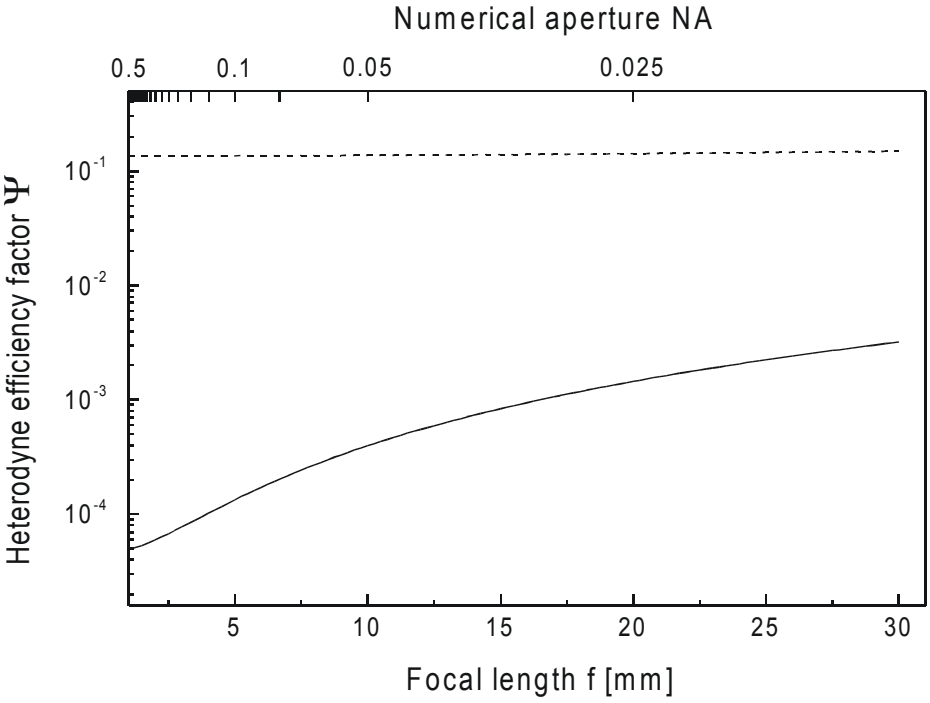

Figure 7. The heterodyne efficiency factor $\Psi(z)$ as a function of the focal length f, or numerical aperture NA, when the probing depth $z = 0.5\,\mathrm{mm}$, and the shower curtain effect is included. The dashed and solid curves are calculated for the case of a low $(2\,\mathrm{mm}^{-1})$ and a high $(10\,\mathrm{mm}^{-1})$ scattering coefficient, respectively ($\lambda = 814\,\mathrm{nm}$, $g = 0.955$ ($\theta_{\mathrm{rms}} = 0.3\,\mathrm{rad}$), $n = 1.4$, $w_0 = 0.5\,\mathrm{mm}$).

focal length is to keep it as short as possible. However, as a direct consequence of the shower curtain effect, the advantage of choosing a short focal length decreases with increasing value of the scattering coefficient, or the optical depth $\mu_{\mathrm{s}}z$.

We now consider the case where the numerical aperture, and subsequently the lateral resolution, are kept constant while the distance d from the lens to the tissue is varied, and the probing depth z is constant. If the shower curtain effect is excluded, we get that the heterodyne efficiency factor decreases when the distance from the lens to the tissue increases. On the other hand, if the shower curtain effect is included, we get that the heterodyne efficiency factor is independent of the distance from the lens to the tissue. The latter is intuitively correct for the geometry of interest. This is due to the fact that the reference beam or local oscillator can be projected onto the surface of the tissue, and as long as the numerical aperture is kept constant, the local oscillator will be the same. Therefore, we expect the heterodyne efficiency factor to be independent of the distance from the lens to the tissue as long as the numerical aperture is kept constant.

Calculation of the maximum probing depth

The maximum probing depth is of considerable interest in the characterization and optimization of an OCT system when used for imaging in highly scattering tissue. Therefore, a calculation of the maximum probing depth, which is based on the OCT model described above, is presented in this section. Without loss of generality, the calculation is performed for a shot-noise limited system.

The calculation of the maximum probing depth z_{max}, which is carried out in this section, is based on the minimum acceptable signal-to-noise ratio. The mini-

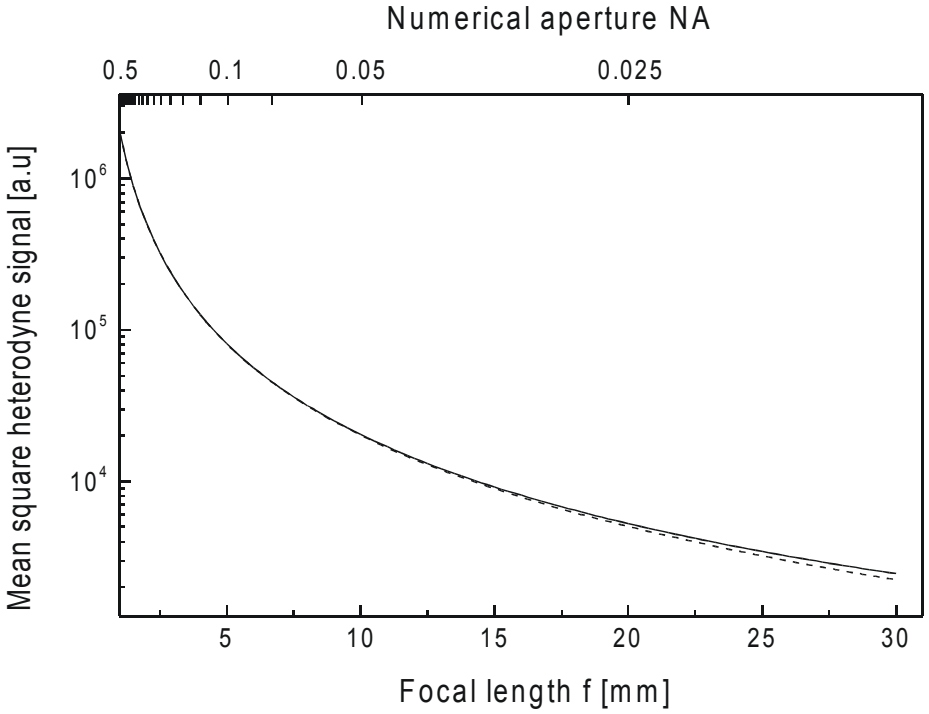

Figure 8. The mean square heterodyne signal current $\langle i^2 \rangle$ *as a function of the focal length* f*, or numerical aperture NA, with* (*solid curve*) *and without* (*dashed curve*) *the shower curtain effect. The scattering coefficient* $\mu_\mathrm{s} = 2\,\mathrm{mm}^{-1}$*, and the probing depth* $z = 0.5\,\mathrm{mm}$ ($\lambda = 814\,\mathrm{nm}$, $g = 0.955$ ($\theta_\mathrm{rms} = 0.3\,\mathrm{rad}$), $n = 1.4$, $w_0 = 0.5\,\mathrm{mm}$).

mum acceptable signal-to-noise ratio is closely related to the maximum acceptable uncertainty in the determination of the amplitude and position of the OCT signal when the envelope detection is performed. In these calculations, the value 3 is used as the minimum acceptable signal-to-noise ratio, i.e., $SNR\,(z_\mathrm{max}) = 3$. Thus, using Eq. (34) and Eq. (36), we have to solve the following equation with respect to z_max in order to determine the maximum probing depth

$$\frac{2\eta P_\mathrm{S}}{h\nu B_\mathrm{w}} \left(\frac{w_0}{f}\right)^2 R_\mathrm{d} \Psi\,(z_\mathrm{max}) = 3. \tag{54}$$

The heterodyne efficiency factor Ψ is given by either Eq. (27) or Eq. (30) depending on the reflection characteristics of the probed discontinuity. As can be seen from Eq. (54), this calculation of the maximum probing depth is based on the design variables of the OCT system, the detector characteristics, and the optical properties of the tissue.

Fig. 10 shows the maximum probing depth z_max as a function of the scattering coefficient μ_s for a typical OCT system. The solid curve represents the case found in tissue where the probed discontinuity is giving a diffuse backscattering and the shower curtain effect is present. The dashed curve represents three different cases which all give the same dependence of the maximum probing depth on the scattering coefficient. The three different cases are diffuse backscattering at the discontinuity with exclusion of the shower curtain effect, specular reflection at the discontinuity, and pure single backscattering. It is important to note that the shower curtain effect, which is a multiple scattering effect, alone is responsible for the marked difference between the solid and the dashed curves. This demonstrates that multiple scattering and the shower curtain effect are important effects to consider when calculating the maximum probing depth in tissue.

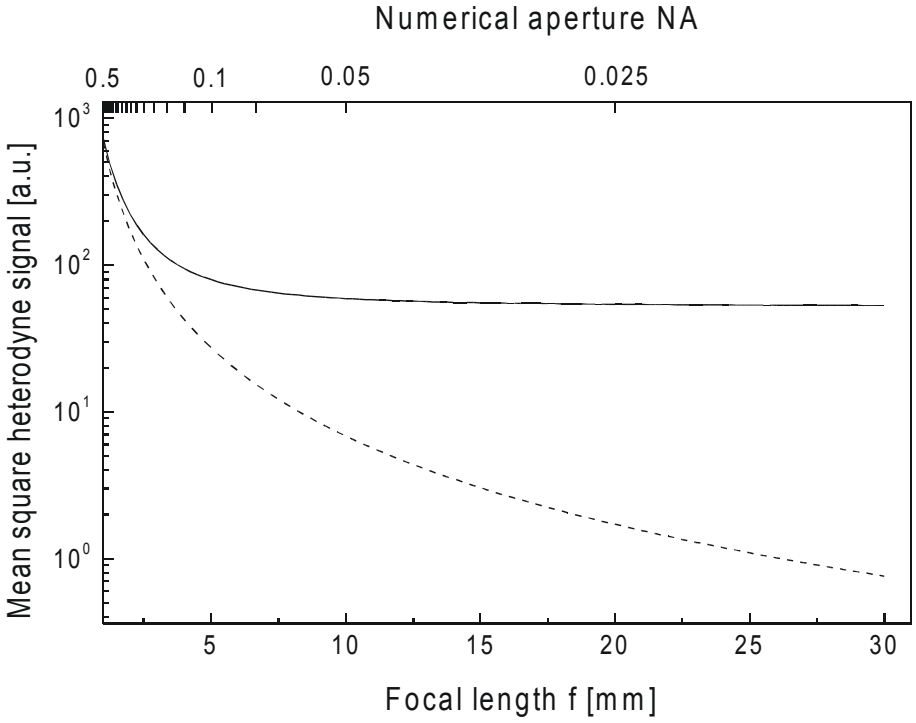

Figure 9. The mean square heterodyne signal current $\langle i^2 \rangle$ *as a function of the focal length* f*, or numerical aperture NA, with* (*solid curve*) *and without* (*dashed curve*) *the shower curtain effect. The scattering coefficient* $\mu_s = 10\,\mathrm{mm}^{-1}$*, and the probing depth* $z = 0.5\,\mathrm{mm}$ ($\lambda = 814\,\mathrm{nm}$, $g = 0.955$ ($\theta_{\mathrm{rms}} = 0.3\,\mathrm{rad}$), $n = 1.4$, $w_0 = 0.5\,\mathrm{mm}$).

Fig. 11 shows $z_{\max}$ as a function of μ_s and the reflection coefficient R_d of the probed tissue discontinuity for the case found in tissue where the discontinuity is giving a diffuse backscattering and the shower curtain effect is present. The 3D plot shows $z_{\max}$ with common parameters for skin tissue, and commonly used OCT system parameters. The range of R_d is based on the values of the index of refraction of the various layers of human skin given by V. V. Tuchin *et al.* [61]. The range of the scattering coefficient has been chosen from commonly cited values in the literature [52],[61].

The focal length of the focusing lens in the sample arm and the $1/e$ intensity radius of the sample beam being focused are important design variables of the OCT system. In order to investigate how these parameters influence the maximum probing depth, $z_{\max}$ is shown as a function of μ_s and the focal length f in Fig. 12 for a typical OCT system. As in Fig. 11, the calculations are carried out for the case found in tissue where the discontinuity is giving a diffuse backscattering and the shower curtain effect is present.

Fig. 12 shows that, in general, the maximum probing depth depends on the focal length at small values of the scattering coefficient, but is independent of the focal length at larger values of the scattering coefficient. A similar behavior is observed for the maximum probing depth as a function of μ_s and the $1/e$ intensity radius of the sample beam being focused. This behavior is due to multiple scattering of the light in the tissue. At scattering coefficients found in human skin tissue [52],[61], for example, it may be concluded from Fig. 12 that the maximum probing depth is independent of the focal length f. This is an important conclusion because the depth of focus and the lateral resolution of the OCT system may then be chosen independently of the maximum probing depth. For example, if no scanning of the

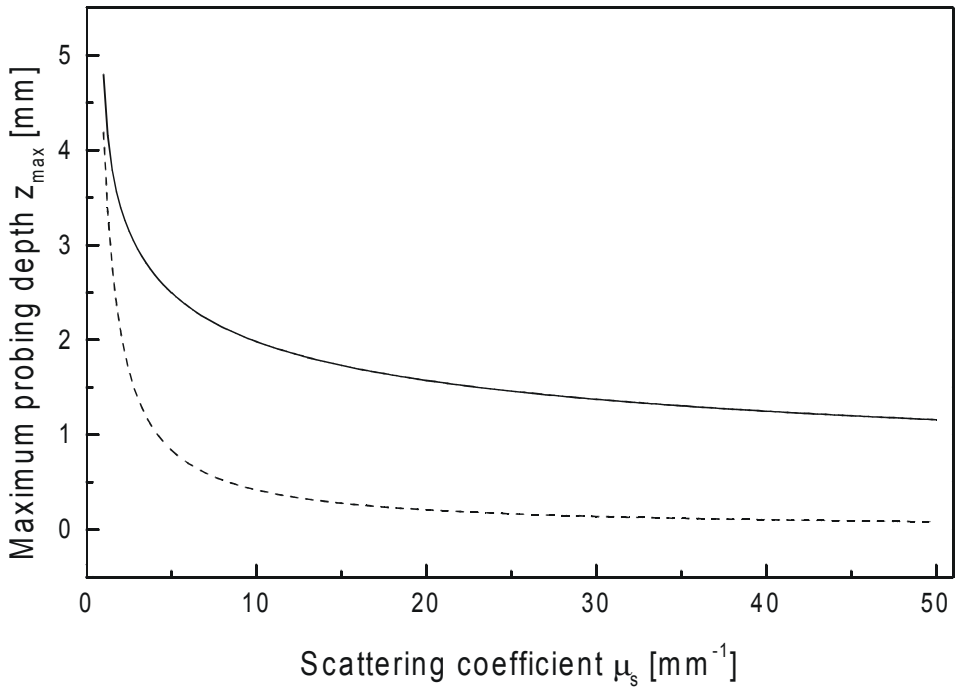

Figure 10. The maximum probing depth $z_{\max}$ as a function of the scattering coefficient μ_s for a typical OCT system. Solid curve: diffuse backscattering at discontinuity and shower curtain effect included. Dashed curve: represents three different cases yielding similar results; (i) diffuse backscattering at discontinuity and the shower curtain effect excluded, (ii) specular reflection at discontinuity, and (iii) pure single backscattering ($\lambda = 814\,\mathrm{nm}$, $g = 0.955$ ($\theta_{\mathrm{rms}} = 0.3\,\mathrm{rad}$), $n = 1.4$, $R_{\mathrm{d}} = 0.05\,\%$, $f = 16\,\mathrm{mm}$, $w_0 = 0.125\,\mathrm{mm}$, $P_{\mathrm{S}} = 650\,\mu\mathrm{W}$, $B_{\mathrm{w}} = 10\,\mathrm{kHz}$, $\eta = 0.8$).

focal plane in the tissue is desirable and, therefore, a large depth of focus has been chosen, the same maximum probing depth is obtained as for a system with a short depth of focus where the focal plane is scanned to keep it matched to the reference arm. This conclusion is not surprising or contrary to assumptions already held in the field. However, the theoretical analysis in this section provides a theoretical foundation for these. This agreement may also be taken as a validation of the new OCT model.

Summary

A new theoretical description of the OCT technique when used for imaging in highly scattering tissue has been presented. The description is based on the extended Huygens-Fresnel principle. It is shown that the theoretical model describes the performance of the OCT system in both the single and multiple scattering regimes simultaneously. The model inherently includes the shower curtain effect. This effect has been omitted in previous theoretical models of OCT systems. It has been demonstrated in this chapter that the shower curtain effect is of utmost importance in the theoretical description of an OCT system.

The analytical model enables a calculation of the SNR, where the optical properties of the tissue have been taken into account. A method for calculating the maximum probing depth based on the SNR has been presented. Finally, the model enables the determination of the lateral resolution of the OCT system at arbitrary depths in the scattering tissue.

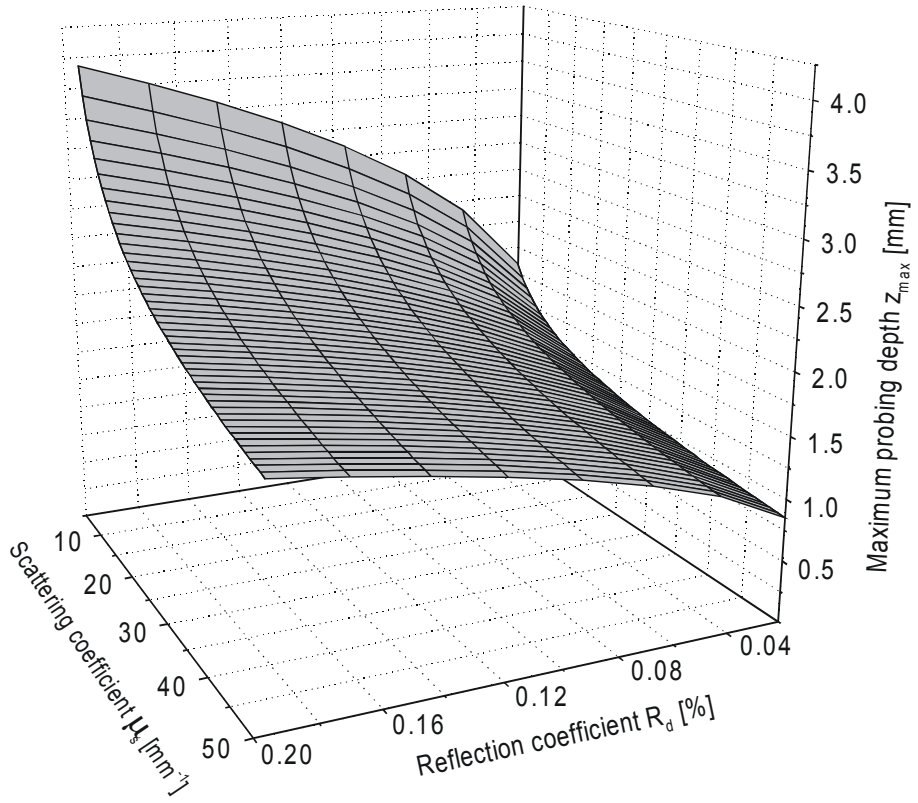

Figure 11. The maximum probing depth $z_{\max}$ as a function of the scattering coefficient μ_s and the reflection coefficient R_d for a typical OCT system together with diffuse backscattering at the discontinuity and the shower curtain effect included ($\lambda = 814\,\mathrm{nm}$, $g = 0.955$ ($\theta_{\mathrm{rms}} = 0.3\,\mathrm{rad}$), $n = 1.4$, $f = 16\,\mathrm{mm}$, $w_0 = 0.125\,\mathrm{mm}$, $P_S = 650\,\mu\mathrm{W}$, $B_w = 10\,\mathrm{kHz}$, $\eta = 0.8$).

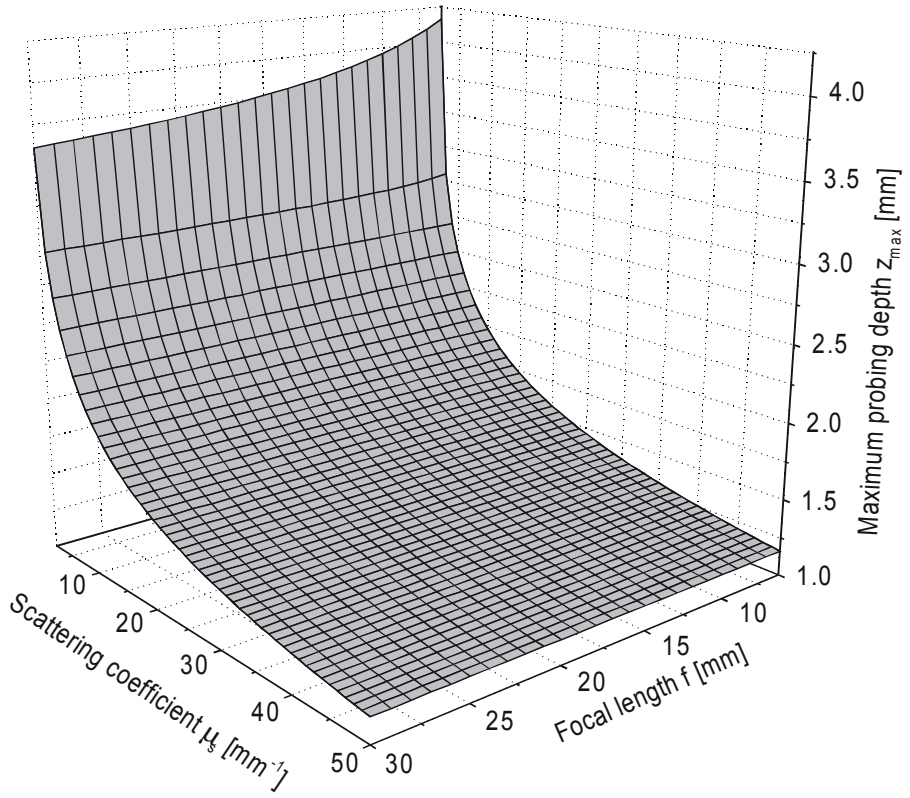

Figure 12. The maximum probing depth $z_{\max}$ as a function of the scattering coefficient μ_s and the focal length f for a typical OCT system together with diffuse backscattering at the discontinuity and the shower curtain effect included ($\lambda = 814\,\mathrm{nm}$, $g = 0.955$ ($\theta_{\mathrm{rms}} = 0.3\,\mathrm{rad}$), $n = 1.4$, $R_{\mathrm{d}} = 0.05\,\%$, $w_0 = 2\,\mathrm{mm}$, $P_{\mathrm{S}} = 650\,\mu\mathrm{W}$, $B_{\mathrm{w}} = 10\,\mathrm{kHz}$, $\eta = 0.8$).

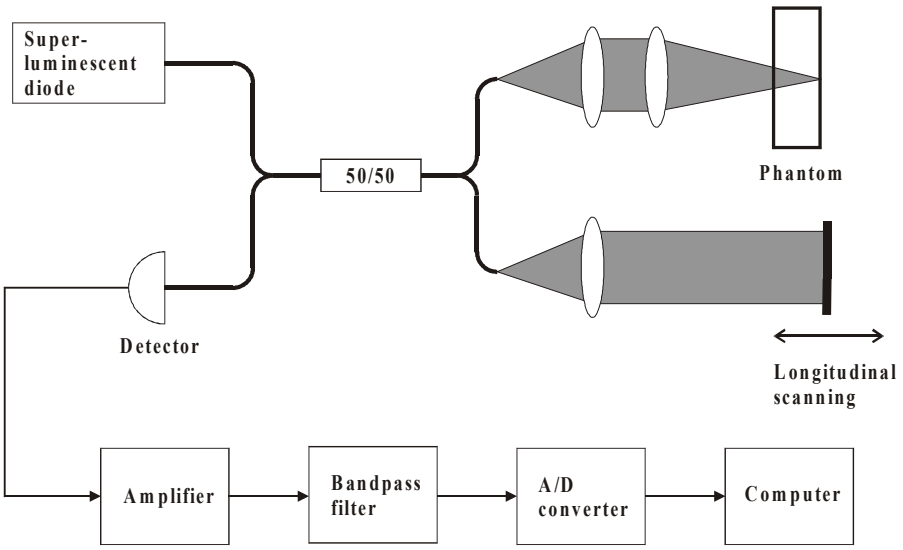

Figure 13. The OCT system used in the experimental verification of the OCT model.

3 Experimental verification of the new OCT model

The new OCT model is verified by measurements on liquid phantoms consisting of aqueous suspensions of microspheres, and solid phantoms [35], [36],[37],[39]. The measurements are carried out by using a conventional OCT setup [1], which has been constructed during the Ph.D. thesis project.

3.1 Experimental setup

A schematic of the OCT system is shown in Fig. 13. It consists of a superluminescent diode (SLD), Superlum SLD-361/A-BUT-SM, with a center wavelength of 814 nm, a FWHM spectral bandwidth of 22.8 nm, and an output power of 1.9 mW. The measured spectrum of the SLD is shown in Fig. 14, which was obtained by using a 600 l/mm spectrograph. The light from the SLD is coupled into a single-mode fiber-optic Michelson interferometer with a 50/50 beamsplitter. In the sample arm, the beam, having a $1/e$ intensity radius w_0 of 0.125 mm, is focused in the phantom by a lens with a focal length f of 16 mm. In the reference arm, the light is reflected at a mirror attached to a piezo-stack, which is placed on a computer-controlled translation stage. The reference mirror is scanned by the piezo (translation stage stationary) when measurements are carried out on the liquid phantoms. This is due to the fact that the phase and the amplitude of the scattered electric field are modulated because of the random motion of the scattering microspheres in the liquid phantoms [62]. These modulations appear as fluctuations in the measured interference signal. The piezo enables capturing of a large number of scans on a time-scale which is short compared to the fluctuations. Each scan is then analyzed to determine the maximum amplitude of the envelope, and their mean value is used in the determination of the heterodyne efficiency factor.

The light reflected at the probed discontinuity in the phantom and at the reference mirror are mixed at a silicon detector, and the resulting interference signal is amplified. Within the scan range used of the translation stage and the piezo, the velocity v is constant. The constant-velocity movement of the reference mir-

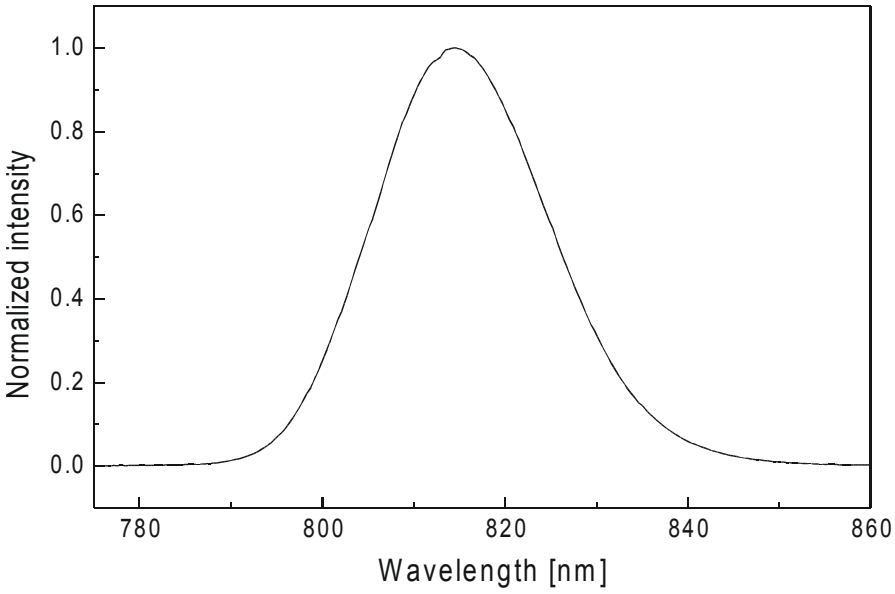

Figure 14. The measured spectrum of the superluminescent diode.

ror shifts the center frequency of the interference signal to the Doppler frequency $f_\mathrm{d} = 2v/\lambda$, which facilitates removal of the dc background and low-frequency noise. Therefore, after the amplification, the interference signal is bandpass filtered by a filter centered at f_d. The Doppler frequency and the bandpass filter used in the case of the translation stage scanning and piezo scanning are 15 kHz, $10-20$ kHz, and 3.5 kHz, $2-5$ kHz, respectively. After the bandpass filtering, the interference signal is digitized with a 12-bit analog-digital converter and transferred to a computer. The data acquisition is carried out by using appropriate LabVIEW programs[1].

The envelope of the low-coherence interference signal is determined by using the Hilbert transform [63]. The envelope is given by $|i_\mathrm{s} + \mathrm{i}H_\mathrm{t}(i_\mathrm{s})|$, where i_s is the interference signal, H_t is the Hilbert transform, and i is the imaginary unit. The maximum amplitude of the envelope is then used in the determination of the heterodyne efficiency factor.

An example of a measured interference signal with envelope is shown in Fig. 15. The signal is from a polymer-air interface of one of the solid phantoms described below. The coherence length l_c, determined from this measurement (FWHM), is 16.7 μm. This should be compared with the value of the coherence length obtained by using the equation $l_\mathrm{c} = (\sqrt{2\ln(2)/\pi})\lambda^2/\Delta\lambda$ for a Gaussian spectrum, where λ and $\Delta\lambda$ (FWHM) are determined from the measured spectrum of the SLD shown in Fig. 14 [7]. The coherence length obtained in this way is 19.3 μm, which is in good agreement with the measured value.

3.2 Measurements on liquid phantoms

The liquid phantoms consist of latex (polyvinyltoluene) microspheres with a mean diameter of 2.04 μm (std. dev. 2.2 %) suspended in distilled, deionized water. Mie theory [53] is used to calculate g and μ_s, using the sphere diameter, the index of refraction (1.59 @ 589 nm (25 °C)), the specific weight (1.05 g/ml), and the

[1] LabVIEW 5.0 is a program development environment that uses a graphical programming language, *G*, to create programs in block diagram form.

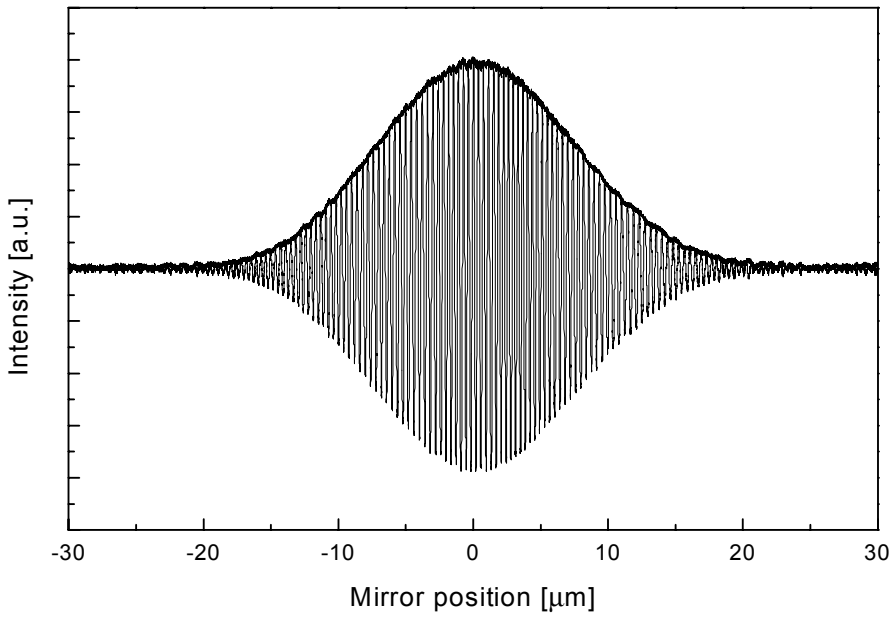

Figure 15. An example of a measured interference signal with envelope.

concentration of the microspheres (g/g), together with the index of refraction (1.33) and the specific weight (1.00 g/ml) of liquid water. The absorption of these liquid phantoms is negligible.

In the first experiment, the liquid phantoms are placed in a 1.0 mm (internal thickness) glass cuvette. Apart from the front glass plate of the cuvette, the geometry is identical to the one shown in Fig. 1 with $z = 1.0\,\mathrm{mm}$. In this case, the probed liquid - glass discontinuity gives a specular reflection.

Fig. 16 shows the theoretical prediction (solid line) and measurements (circles) of the heterodyne efficiency factor Ψ as a function of the scattering coefficient μ_s for this case with specular reflection at the discontinuity. Note, that the cuvette glass plate in front of the liquid phantoms has been taken into account in the theoretical analysis by using the following equation for $d\,(z)$

$$d\,(z) = f - \left(\frac{z}{n}\right) + \delta\left(1 - \frac{1}{n_\mathrm{g}}\right), \tag{55}$$

where δ and n_g are the thickness and index of refraction of the glass plate, respectively. As shown in Fig. 16, excellent agreement between theory and experiment is obtained. Note that this agreement is obtained without any kind of fitting. As seen from the figure, the multiple scattering regime, which is indicated by the change of slope of the curve, has not been reached in this experiment.

In the second experiment, the liquid phantoms are placed in a 0.5 mm (internal thickness) glass cuvette with a changeable back plate. In the measurements, both a silicon and a glass plate giving diffuse backscattering and specular reflection, respectively, are used to define the probed liquid - back plate discontinuity. Apart from the front glass plate of the cuvette, the geometry is identical to the one shown in Fig. 1 with $z = 0.5\,\mathrm{mm}$.

Fig. 17 shows the theoretical predictions and measurements of the heterodyne efficiency factor Ψ as a function of the scattering coefficient μ_s for the case of diffuse backscattering (dashed (no fit) and solid (fitted curve; fitting parameter: w_0) lines; squares) and specular reflection (dash-dot line; circles) at the discontinuity.

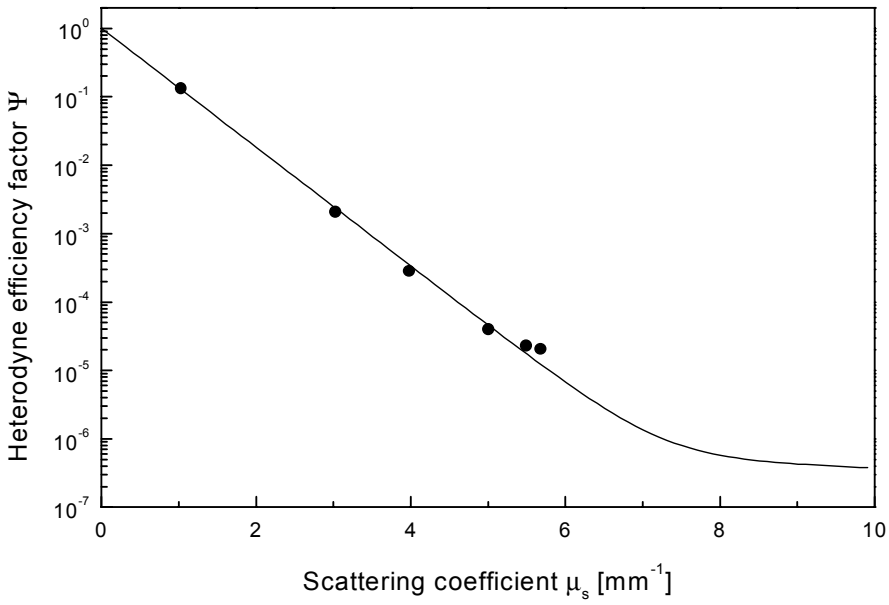

Figure 16. The theoretical prediction (solid line) and measurements (circles) of the heterodyne efficiency factor Ψ as a function of the scattering coefficient μ_s for the case of specular reflection at the discontinuity at depth $z = 1.0\,\mathrm{mm}$ ($g = 0.929$ ($\theta_{\mathrm{rms}} = 0.38\,\mathrm{rad}$), $n = 1.33$, $\delta = 1.15\,\mathrm{mm}$, $n_g = 1.5$).

As shown in Fig. 17, excellent agreement between theory and experiment in the case of specular reflection is obtained. As for the first experiment, this agreement is obtained without any kind of fitting. In the case of diffuse backscattering, the experimental data show deviations from theory (dashed line; no fit). However, there is no doubt that the experimental results show a clear deviation from what would be obtained in the absence of the shower curtain effect (i.e., specular reflection). At $\mu_s = 7\,\mathrm{mm}^{-1}$, the experimental value of the heterodyne efficiency factor is a factor of about 5 larger than the value that would be obtained in the absence of the shower curtain effect. This means that we have certainly demonstrated how the shower curtain effect increases the heterodyne signal through enhanced spatial coherence of the multiple scattered light.

The strong fluctuations of the interference signal caused by the motion of the scattering microspheres may be the reason for the deviation from the theoretical curve.

3.3 Measurements on solid phantoms

In order to further verify the validity of the new OCT model, and to sustain the claim regarding the motion of the microspheres given above, measurements are carried out on solid phantoms. In this experiment, the geometry is identical to the one shown in Fig. 1. Solid phantoms consisting of scattering microspheres (approximate diameter size $10\,\mu\mathrm{m}$) in polymer are used as the scattering medium with thickness z. The optical parameters of the solid phantoms, i.e., the asymmetry parameter, the scattering coefficient, and the absorption coefficient, were determined by carrying out integrating sphere and collimated transmission measurements, and using the inverse adding-doubling method [64]. All phantoms used had a negligible absorption. The probed discontinuity is defined by the phantom-air interface. This discontinuity is giving a diffuse backscattering.

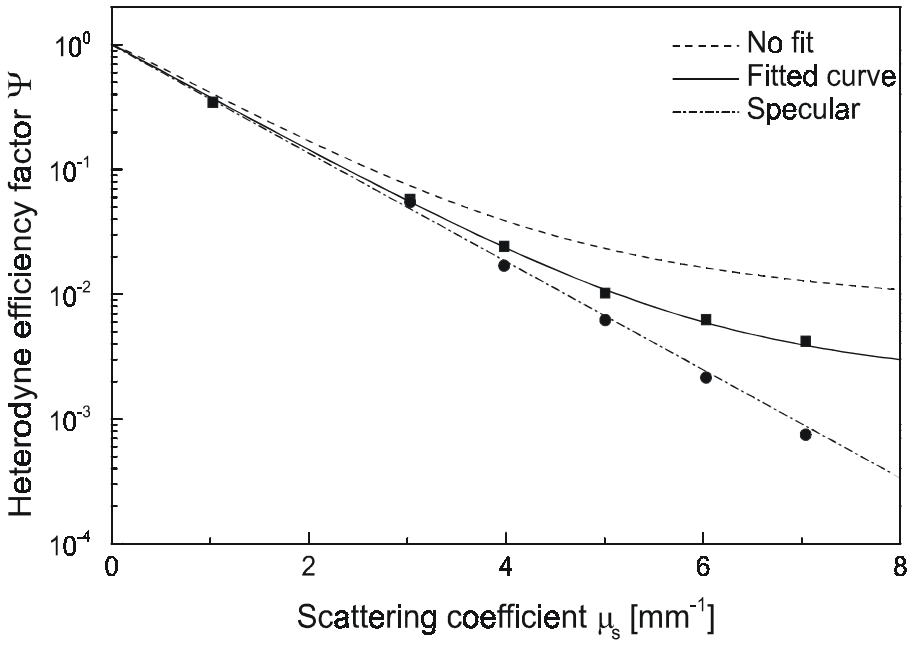

Figure 17. The theoretical curves and measurements of the heterodyne efficiency factor Ψ as a function of the scattering coefficient μ_s for the case of diffuse backscattering (dashed (no fit) and solid (fitted curve; fitting parameter: w_0) lines; squares) and specular reflection (dash-dot line; circles) at the discontinuity. The probing depth z is 0.5 mm, and the typical standard deviation for the squares is $\pm 7.8\,\%$ ($g = 0.929$ ($\theta_{\mathrm{rms}} = 0.38$ rad), $n = 1.33$, $\delta = 1.256$ mm, $n_g = 1.5$).

Fig. 18 shows the theoretical curves and the measurements of the heterodyne efficiency factor Ψ as a function of the scattering coefficient μ_s for two different probing depths z ($z = 5.25$ mm (dashed; square) and $z = 7.55$ mm (dash-dot; circle)) and diffuse backscattering at the probed discontinuity. The theoretical curves are created by fitting to the experimental points using g as the only fitting parameter. The values of g obtained in this way are 0.994 for $z = 5.25$ mm and 0.989 for $z = 7.55$ mm. These values are lying within the experimental errors of the measured asymmetry parameters ($g = 0.996$ and $g = 0.997$, respectively), which means that we have a good agreement between theory and experiment. The author is aware that this conclusion is based on a limited number of measurements. However, this experiment may be taken as a supplement to the other two experiments.

3.4 Summary

The new OCT model has been verified by measurements on liquid phantoms consisting of aqueous suspensions of microspheres, and solid phantoms.

In the two experiments with liquid phantoms and a specular reflection, excellent agreement between theory and experiment were obtained for Ψ as a function of μ_s. This agreement was obtained without any kind of fitting.

In the experiment with liquid phantoms and a diffuse backscattering, it was demonstrated how the shower curtain effect increases the heterodyne signal through enhanced spatial coherence of the multiple scattered light. The validity of the model in the case of diffuse backscattering was further supported by an experiment with solid phantoms.

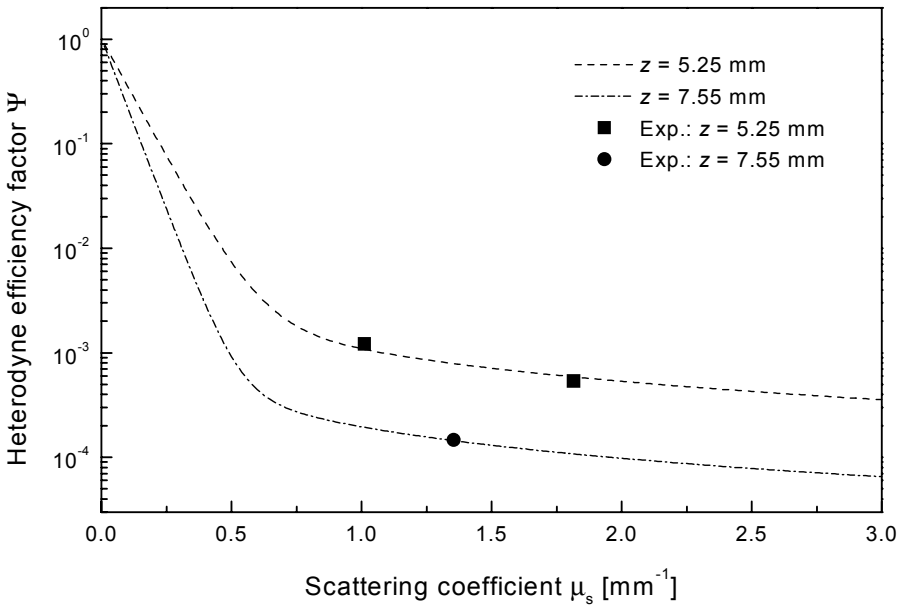

Figure 18. The theoretical curves and measurements of the heterodyne efficiency factor Ψ as a function of the scattering coefficient μ_s for two different probing depths ($z = 5.25\,\mathrm{mm}$ (dashed; square) and $z = 7.55\,\mathrm{mm}$ (dash-dot; circle)) and diffuse backscattering at the probed discontinuity ($n = 1.5$).

The measurements were carried out by using a conventional OCT setup, which has been constructed during the Ph.D. thesis project.

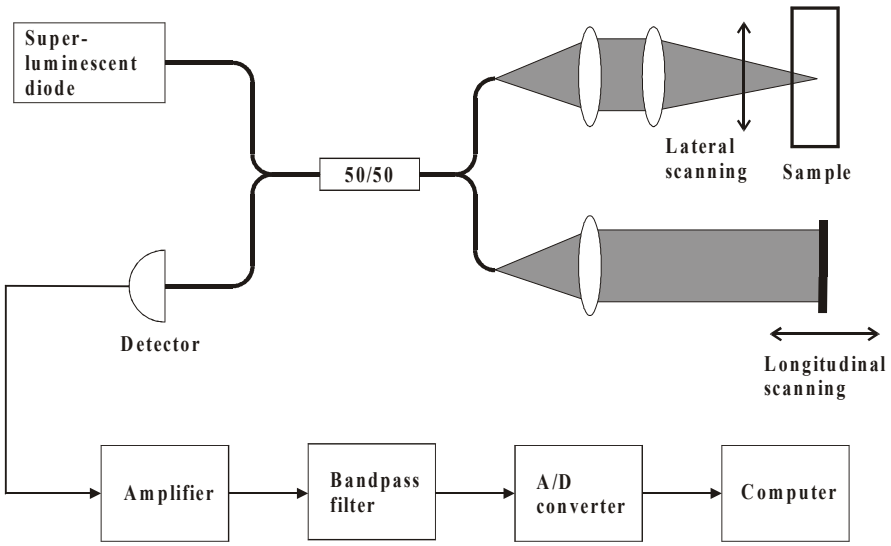

Figure 19. The OCT imaging system

4 OCT imaging

In this chapter, OCT images of human skin, a mouse ear, and a table tennis ball is presented. The aim is to demonstrate the imaging capabilities of the OCT system, which has been developed during the Ph.D. thesis project. Furthermore, a new true-reflection OCT imaging algorithm is presented, and the principle is demonstrated by measurements on a solid phantom.

4.1 Experimental setup

In the last chapter, a description was given of the OCT system used in the experimental verification of the new OCT model. The main part of this OCT system is also used in the imaging system. In the following, the elements, which are specific for the imaging system, will be described.

A schematic of the OCT imaging system is shown in Fig. 19. The probe module, consisting of the end of the sample arm fiber with a collimating GRIN lens, and a focusing lens or microscope objective, is placed on a xyz computer-controlled translation stage. This enables the lateral scanning of the sample, which is necessary in order to obtain OCT images. The distance between adjacent longitudinal or depth scans is $10\,\mu$m in the OCT images shown in this thesis. Only one longitudinal scan is taken in every lateral position, so no averaging is performed. The longitudinal scans are performed using the translation stage described in the last chapter. The optical power on the sample is $500\,\mu$W.

The data acquisition is carried out by using an appropriate LabVIEW program. A C++ program has been developed to handle the processing of the data and the creation of the OCT images[2]. As in the processing of the phantom measurements, the envelope of the individual depth scans is determined by using the Hilbert transform [63]. The resulting data array is then viewed directly as a false-color or gray-scale image.

[2]The C++ program was developed by Thomas M. Jørgensen, Risø National Laboratory, Denmark.

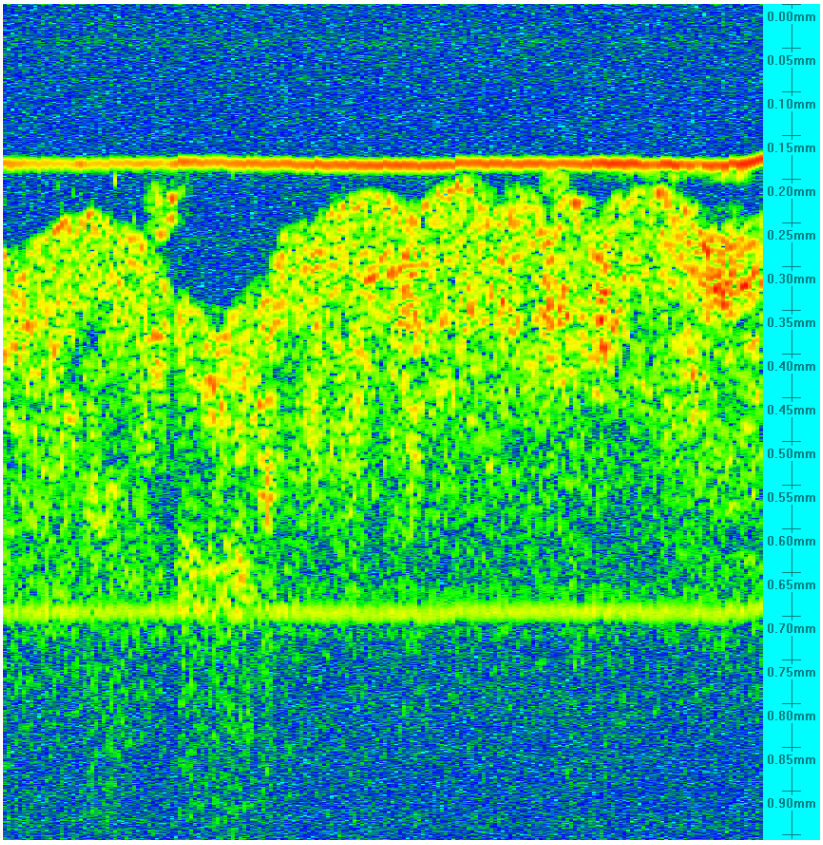

Figure 20. In vivo OCT image of healthy skin on the left forearm (volar side) of a human volunteer (2.0 mm *lateral* × 0.955 mm *longitudinal*).

4.2 OCT images of human skin

OCT images of healthy skin on the forearm (volar side) of two human volunteers have been obtained *in vivo*. In order to prevent surface movement, the area imaged is placed in contact with a glass window, and index-matching oil is used to reduce the reflection of light from the skin surface. The probe module is adjusted along the optical axis until the skin surface is brought into focus. In this case, a lens with a focal length of 10 mm is used. Using Eq. (52), the upper limit of the lateral resolution is 20.7 μm. The longitudinal resolution in the human skin tissue is 19.3 μm/1.4 = 13.8 μm, where 1.4 is used as the mean index of refraction of the human skin tissue [52].

The OCT images of the healthy skin on the forearm (volar side) of the two human volunteers are shown in Fig. 20 and Fig. 21. Fig. 20 is from the left forearm, and Fig. 21 is from the right forearm. The images are shown with a logarithmic false-color palette (blue:low - red:high), and they have not been subject to image processing. The size of these images is 2.0 × 0.955 mm (lateral × longitudinal). The images have been expanded by a factor of four in the lateral direction, and they consist of 200 × 880 pixels (lateral × longitudinal). This corresponds to a pixel spacing of 10 μm× 1.09 μm (lateral × longitudinal). The scale shown on the right hand side of the images has been corrected by a value of 1.4 for the index of refraction of the human skin tissue [52].

The horizontal lines in the upper part of both images is the glass/skin interface. The horizontal green line just below the glass/skin interface in Fig. 21, and the horizontal lines in the lower part of both images are so-called ghosts caused by the system itself. They may be due to reflections, a non-Gaussian spectrum, or

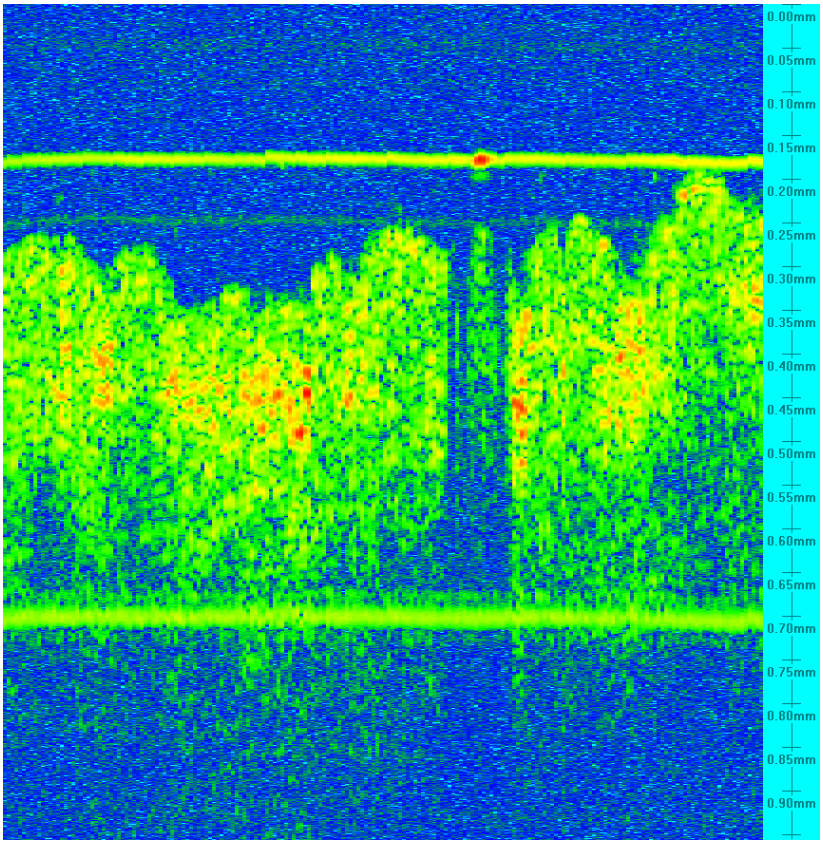

Figure 21. In vivo OCT image of healthy skin on the right forearm (volar side) of a human volunteer (2.0 mm *lateral* × 0.955 mm *longitudinal*).

dispersion.

At the forearm region, the uppermost layer, the stratum corneum, has a thickness of only $10-20\,\mu$m. Other investigations have shown that the border between the stratum corneum and the living epidermis cannot be distinguished with OCT systems having a longitudinal resolution around $10\,\mu$m [65]. This means, that the first skin layer with low signal in Fig. 20 and Fig. 21 may be the epidermis, consisting of stratum corneum and the living part of epidermis. This is supported by the thickness of this layer in both images, which is in good agreement with the values of 50 to $150\,\mu$m given by the literature for the thickness of the stratum corneum together with the living epidermis [66],[67]. The more signal-dense region below the epidermis can then be assigned to the upper part of the dermis. This interpretation of OCT images from the volar side of the forearm is in accordance with the interpretation given by Knüttel *et al.* in a recent publication [68]. The attenuation of the OCT signal is visible in the lower part of the images. It is important to note that a shadowing effect is seen in the middle of Fig. 21, which is probably due to absorption in the epidermis. The maximum probing depth reached in the skin with this OCT system is about $500\,\mu$m. This is comparable with the maximum probing depth obtained in other investigations of human skin using a similar OCT system around 800 nm [69].

4.3 OCT images of a mouse ear

OCT images of a mouse ear have been obtained *in vitro*. The mouse ear is placed in formalin in a closed sample holder with a glass window. The probe module

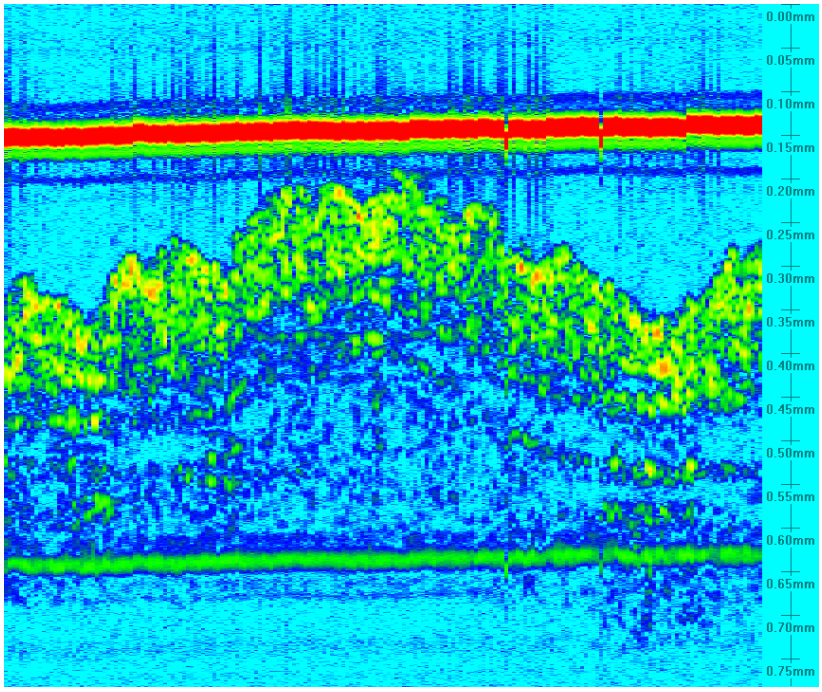

Figure 22. In vitro OCT image of a mouse ear (2.0 mm *lateral* × 0.782 mm *longitudinal*).

is adjusted along the optical axis until the inside surface of the glass window is brought into focus. A lens with a focal length of 10 mm is used. Using Eq. (52), the upper limit of the lateral resolution is 20.7 μm. The longitudinal resolution in the mouse ear tissue is 19.3 μm/1.4 = 13.8 μm, where 1.4 is used as the mean index of refraction of the mouse ear tissue.

Two OCT images from the same site on the mouse ear are shown in Fig. 22 and Fig. 23. The images are shown with a logarithmic false-color palette (light blue:low - red:high), and they have not been subject to image processing. The size of these images is 2.0 × 0.782 mm (lateral × longitudinal). The images have been expanded by a factor of four in the lateral direction, and they consist of 200 × 720 pixels (lateral × longitudinal). This corresponds to a pixel spacing of 10 μm× 1.09 μm (lateral × longitudinal). The scale shown on the right hand side of the images has been corrected by a value of 1.4 for the index of refraction of the mouse ear tissue.

The horizontal red line in the upper part of both images is the inside surface of the glass window. Based on the large signal obtained from this surface, it is concluded, that there is no direct contact between the glass and the mouse ear at the specific site being probed. This means, that the top of the curved layer defines the surface of the mouse ear. The horizontal blue lines just above and below the glass surface, and the horizontal green line in the lower part of both images are ghosts. Furthermore, the vertical blue lines in the upper part of the images are due to noise. Note, that the upper value of the palette is optimized to the signal from the mouse ear and not to the large signal from the glass surface.

In mouse skin, the entire epidermis, i.e., stratum corneum and living epidermis, has a thickness of about 30 μm [70]. This means, that the curved layer seen in the OCT images mainly consists of the dermis, and that the very thin epidermis cannot be distinguished from the dermis in this case. It has not been possible to find OCT images of a mouse ear in the literature for comparison. The two OCT images, which are from exactly the same site on the mouse ear, demonstrate

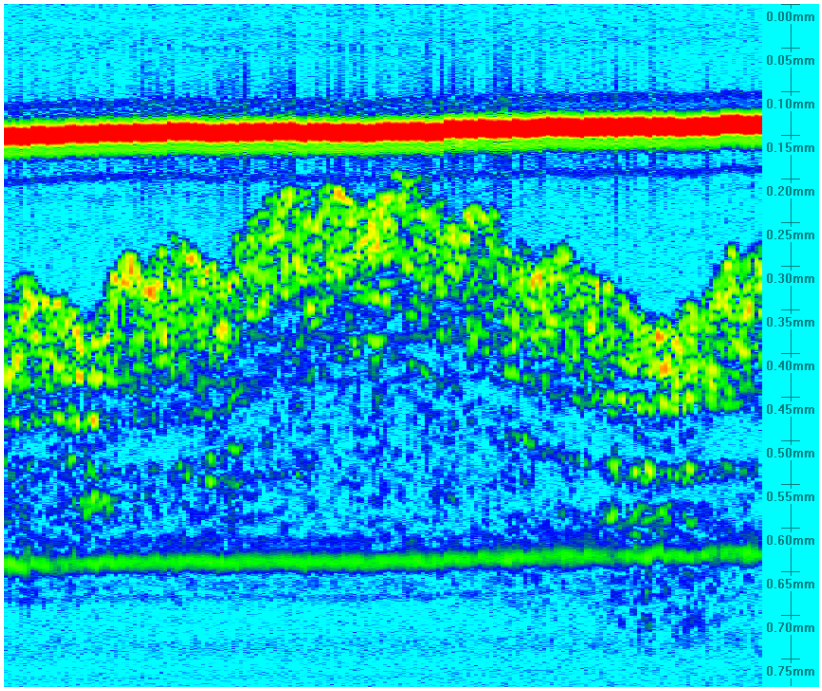

Figure 23. In vitro OCT image of a mouse ear (2.0 mm *lateral* × 0.782 mm *longitudinal*).

excellent reproducibility.

4.4 OCT images of a table tennis ball

In order to demonstrate the difference of using a probe module with a low and a high numerical aperture when generating OCT images, images of a table tennis ball are obtained. A cross-sectional view of the geometry is shown in Fig. 24. The focal plane of the sample beam is lying in the tangential plane of the contact point, which is perpendicular to the plane of the paper in Fig. 24. The imaging plane is lying in the plane of the paper, and the OCT images are generated by scanning the sample beam as indicated in Fig. 24. The longitudinal resolution in the shell of the table tennis ball is $19.3\,\mu\text{m}/1.5 = 12.9\,\mu\text{m}$, where 1.5 is used as the mean index of refraction of the celluloid shell of the table tennis ball.

Two OCT images have been obtained by using a probe module with a low and a relatively higher numerical aperture, and the images are shown in Fig. 25 and Fig. 26, respectively. The images are shown with a logarithmic false-color palette (light blue:low - red:high), and they have not been subject to image processing. The size of these images is 4.0 × 1.0125 mm (lateral × longitudinal). The images have been expanded by a factor of two in the lateral direction, and they consist of 400 × 548 pixels (lateral × longitudinal). This corresponds to a pixel spacing of $10\,\mu\text{m}\times\ 1.85\,\mu\text{m}$ (lateral × longitudinal).

The images shown in Fig. 25 and Fig. 26 were obtained by using a microscope objective with a focal length of 14.8 mm and 4.3 mm, respectively. This means that the corresponding lateral resolution in the focal plane, and the depth of focus are $30.7\,\mu\text{m}$,1.8 mm and $8.9\,\mu\text{m}$,0.15 mm, respectively. The differences in the lateral resolution and the depth of focus are expressed in the OCT images. Due to the higher lateral resolution, the OCT image of the table tennis ball in Fig. 26 is less coarse-grained than the OCT image in Fig. 25. However, due to the smaller depth of focus, a backscattered signal is only obtained from the upper part of the table

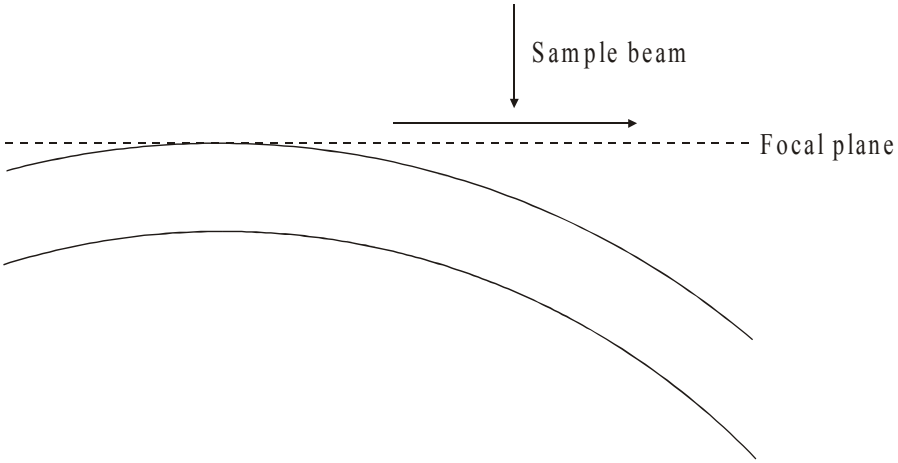

Figure 24. The geometry used in the imaging of the table tennis ball.

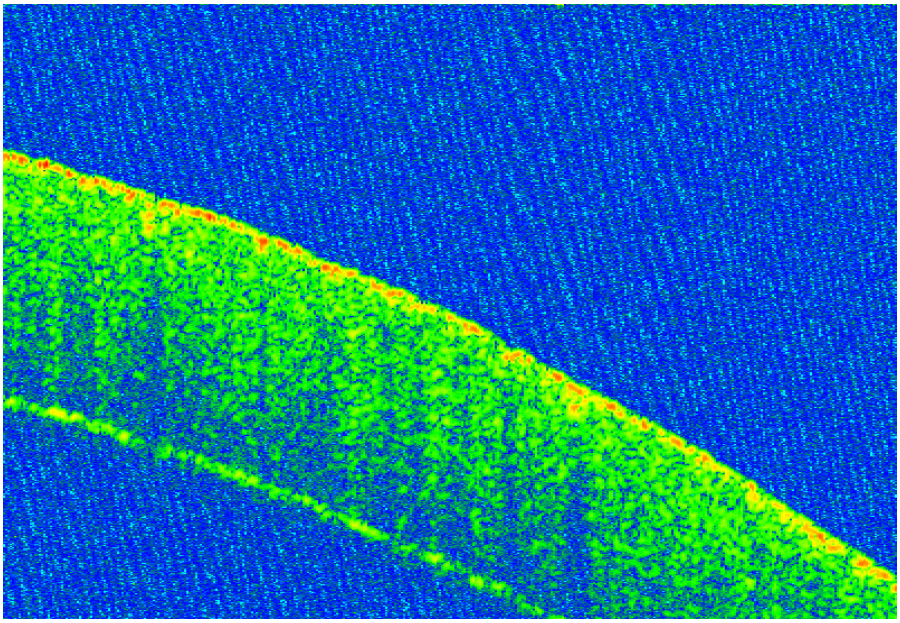

Figure 25. OCT image of a table tennis ball obtained by using a low numerical aperture (4.0 mm *lateral* × 1.0125 mm *longitudinal*).

tennis ball in Fig. 26 as compared with Fig. 25, and the reflected signal from the internal ball-air interface is weaker. This demonstrates why a depth of focus, which is small compared with the thickness of the object under investigation, should be combined with dynamic focusing [71]. This means that the focal plane is always matched to the coherence gate, which also results in a depth-independent lateral resolution in the case of diffraction limited focusing [71].

4.5 True-reflection OCT imaging algorithm

The interpretation of conventional OCT images like the ones shown above is not always an easy task. One reason for this is the fact that an OCT signal, measured at a given position in a nonabsorbing scattering medium, is a result of not only the amount of light reflected at the given position, but also the attenuation due to

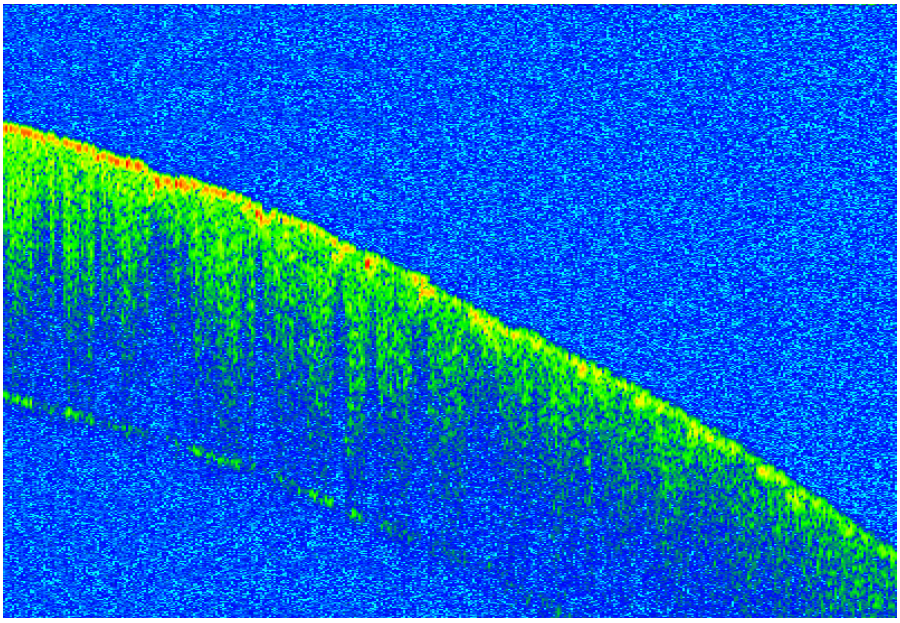

Figure 26. OCT image of a table tennis ball obtained by using a high numerical aperture (4.0 mm *lateral* × 1.0125 mm *longitudinal*).

scattering when the light propagates through the scattering medium. Therefore, to make images, which give a direct measure of the amount of light reflected at a given position, thereby making interpretation of OCT images easier, it is necessary to be able to separate reflection and scattering effects. This is actually possible by using the new OCT model described in this thesis. It was shown in section 2.2, Eq. (27), that the mean square heterodyne signal current for light reflected at a depth z can be expressed as

$$\left\langle i^2\left(z\right)\right\rangle = \left\langle i^2(z)\right\rangle_0 \Psi\left(z\right), \tag{56}$$

where $\left\langle i^2(z)\right\rangle_0$ is the mean square heterodyne signal current in the absence of scattering, and $\Psi\left(z\right)$ is the heterodyne efficiency factor, which includes all of the scattering effects. The maximum of the envelope of the measured interference signal corresponds to $\sqrt{\left\langle i^2\left(z\right)\right\rangle}$. By dividing the envelope of the measured interference signal with $\sqrt{\Psi\left(z\right)}$, we are able to correct for the scattering effects and determine the envelope that would be obtained in the absence of scattering. It is important to note, that in addition to the system parameters λ, f, and w_0, knowledge about μ_s, θ_rms, and n of the scattering medium is necessary in order to be able to calculate $\sqrt{\Psi\left(z\right)}$. However, in practice, μ_s and θ_rms may be obtained by fitting the expression for $\sqrt{\left\langle i^2\left(z\right)\right\rangle}$ to a measured depth scan of the homogeneous backscattering tissue using an estimated value of n and the appropriate system parameters. Implementing this procedure as an option in the imaging program gives the opportunity to make what may be called *true-reflection OCT images*.

To demonstrate the principle of this algorithm, an experiment has been carried out using a solid phantom. The phantom is shown in Fig. 27. This solid phantom is of the same type as the ones used in the experimental verification of the OCT model. It consists of scattering microspheres (approximate diameter size 10 μm) in a polymer. The optical parameters of the solid phantom, i.e., the asymmetry parameter, the scattering coefficient, and the absorption coefficient, were determined by carrying out integrating sphere and collimated transmission measurements, and using the inverse adding-doubling method [64]. It turned out that the phantom had negligible absorption.

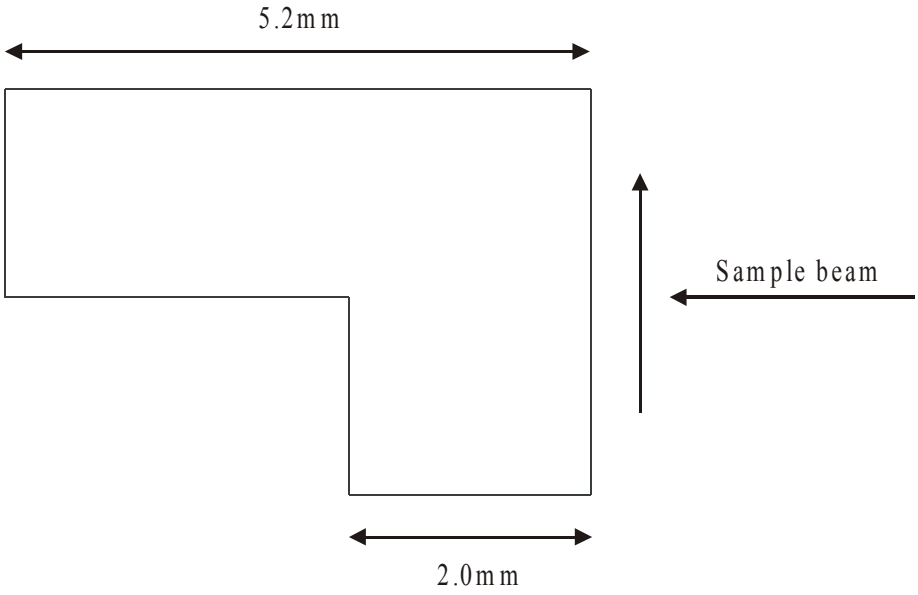

Figure 27. A schematic of the solid phantom used in the demonstration of the true-color OCT imaging algorithm

In the experiment, 40 longitudinal (horizontal) scans are performed across the step as indicated in Fig. 27. The distance between adjacent longitudinal scans is $10\,\mu$m, and only one longitudinal scan is taken in every lateral position. The light is reflected at the air-phantom discontinuity ($z = 0.0\,$mm) and at the two phantom-air discontinuities at $z = 2.0\,$mm and $z = 5.2\,$mm, respectively, which all give a diffuse backscattering and are characterized by the same reflection coefficient. The backscattering from the bulk of the phantom is negligible and cannot be detected. A lens with a focal length of 16 mm is used in this case.

The original unprocessed envelopes of the 40 longitudinal scans are shown in Fig. 28 with the use of a linear false-color palette. The orientation is similar to the orientation in Fig. 27. The first signal from the right is due to light reflected at the air-phantom discontinuity, which will be denoted *the first discontinuity* in the following. The signal from the phantom-air discontinuity at $z = 2.0\,$mm (*the second discontinuity)* is difficult to distinguish, and the signal from the phantom-air discontinuity at $z = 5.2\,$mm (*the third discontinuity)* cannot be distinguished in Fig. 28. This is due to the scattering of the light in the phantom, which attenuates the signal.

By using the true-reflection algorithm described above to correct for the scattering effects, we get the envelopes shown in Fig. 29. The optical parameters of the solid phantom, which were used in the algorithm, are $\mu_s = 1.815\,\text{mm}^{-1}$, $\theta_{\text{rms}} = 0.1096\,$rad ($g = 0.994$), and $n = 1.5$. Because the three discontinuities are characterized by the same reflection coefficient, the same signal level is expected at the three discontinuities in Fig. 29. This is nearly obtained in one position at each discontinuity. A reasonable explanation of the lateral variations of the signal is speckle [7]. The variation of the signal close to the step may also be due to a partly reflection of the beam.

The experimental errors of the measured values of μ_s and g of the solid phantom have been estimated to be $\pm 5\,\%$ and $\pm 1\,\%$, respectively. Values of $\mu_s + 5\,\%$ and $-5\,\%$ have been used in the algorithm, but the changes of the signal levels were very small. This is in contrast to the observation when a value of $g - 1\,\%$ was used in the algorithm, and the envelopes are shown in Fig. 30. Note that the maximum signal of the second discontinuity is now slightly larger than the signal from the

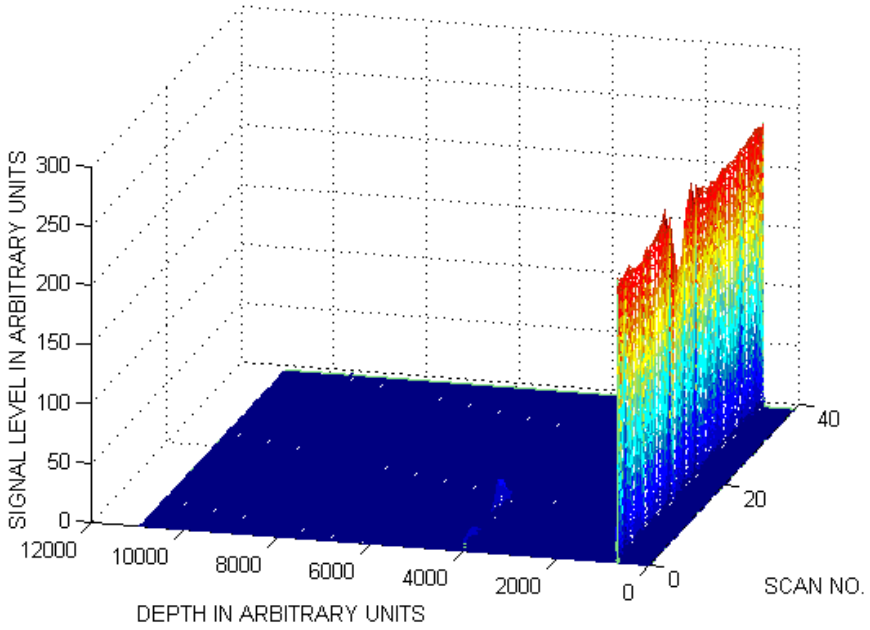

Figure 28. The original unprocessed envelopes of the 40 *longitudinal scans.*

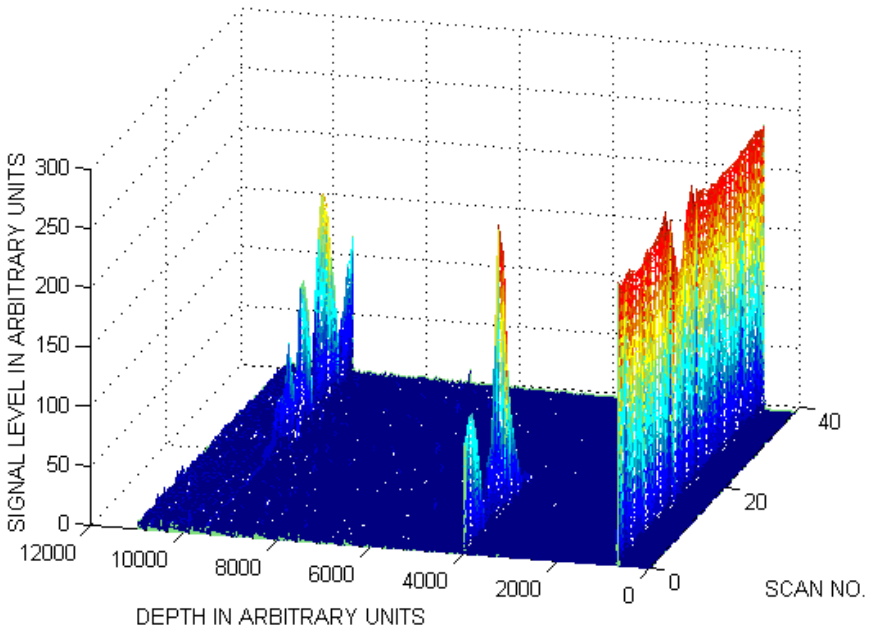

Figure 29. The envelopes of the 40 *longitudinal scans when the true-reflection algorithm has been used.*

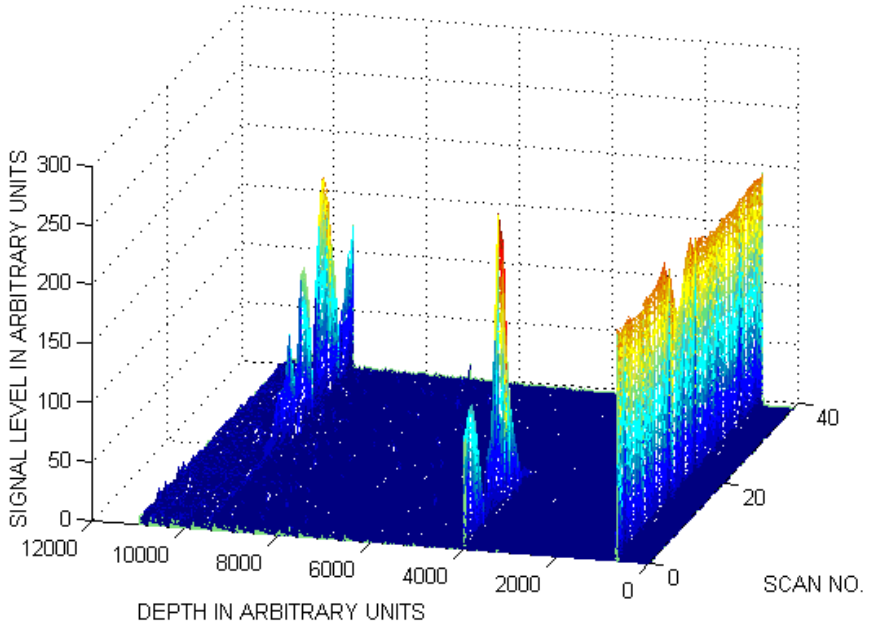

Figure 30. The envelopes of the 40 *longitudinal scans when the true-reflection algorithm has been used together with a value of* $g - 1\,\%$.

first discontinuity. However, the maximum signal levels of the second and third discontinuities seem to be closer to the signal level of the first discontinuity as compared to Fig. 29.

Fig. 31 shows, for comparison, the envelopes obtained if only the single scattering term is used in the expression for Ψ in Eq. (27). It is obvious that the single backscattering model is not sufficient in this case, and it further demonstrates the importance of taking multiple scattering effects into account.

In conclusion, the principle of a so-called true-reflection OCT imaging algorithm has been demonstrated. This algorithm makes it possible to make images, which give a direct measure of the amount of light reflected at a given position by correcting for the scattering effects. Such images may be easier to interpret than conventional OCT images.

4.6 Summary

In order to demonstrate the imaging capabilities of the OCT system, which has been developed during the Ph.D. thesis project, OCT images of human skin, a mouse ear, and a table tennis ball have been obtained.

The OCT images of human skin are of healthy skin on the forearm (volar side) of two human volunteers and have been obtained *in vivo*. The maximum probing depth reached in skin tissue is comparable with the maximum probing depth obtained in other investigations of human skin using a similar OCT system around 800 nm.

Two OCT images of a mouse ear were obtained *in vitro* at exactly the same site, and an excellent reproducibility was demonstrated.

Two OCT images of a table tennis ball have been obtained by using a probe module with a low and a relatively higher numerical aperture. The differences in the lateral resolution and the depth of focus in the two cases were expressed in the OCT images. It was demonstrated why a depth of focus, which is small compared

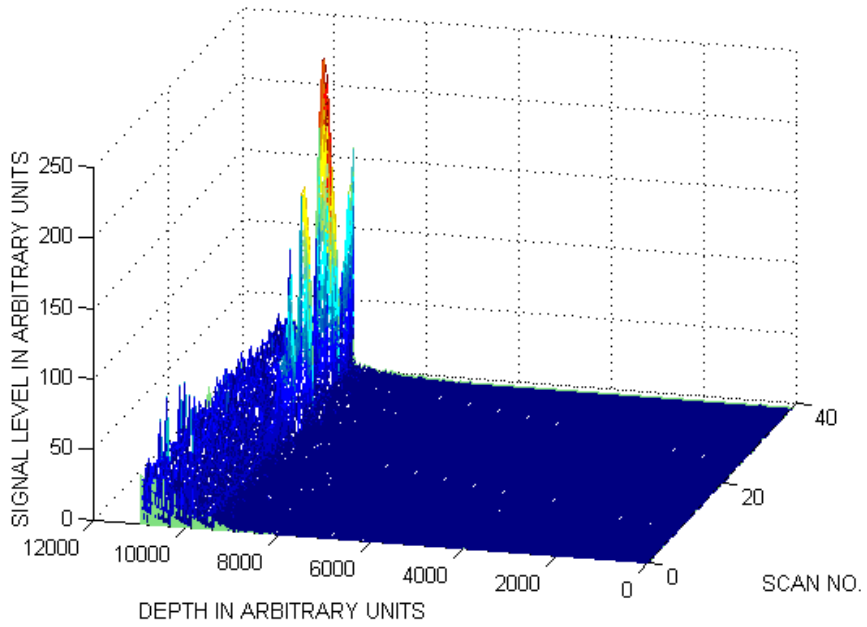

Figure 31. The envelopes obtained by using the true-reflection algorithm when only the single scattering term is used in the expression for Ψ.

with the thickness of the object under investigation, should be combined with dynamic focusing.

Finally, a new true-reflection OCT imaging algorithm has been presented, and the principle has been demonstrated experimentally by measurements on a solid phantom. This algorithm facilitates making images, which give a direct measure of the amount of light reflected at a given position by correcting for the scattering effects, hence the label *true-reflection OCT*. Such images may be easier to interpret than conventional OCT images.

5 The Wigner phase-space distribution function for the OCT geometry

5.1 Introduction

Recently the Wigner phase-space distribution [72] for multiple light scattering in biological media has received considerable attention. This is because it has been suggested by numerous authors that new venues for medical imaging may be based on coherence tomography using measurements of Wigner phase-space distributions [73, 74, 75]. It has been suggested that the Wigner phase-space distribution is particularly useful for biomedical imaging because the phase-space approach provides maximum information, i.e., both space and momentum (angular) information, about the light being used. Therefore, it is important to show that a closed-form solution for the Wigner phase-space distribution function can readily be obtained directly from the extended Huygens-Fresnel [46] solution for the optical field.

In all cases considered here, as well as in Refs. [73],[76],[77],[78],[74],[75], the Wigner phase-space distribution function is positive definite [79], and hence the Wigner function and the specific radiance may be used interchangeably.

As indicated in Fig. 32, we are primarily concerned with a standard OCT propagation geometry, and, as such, we consider a sample beam reflected at a discontinuity giving rise to diffuse backscattering. Although some theoretical analyses of the Wigner phase-space distribution regarding direct transmission appear in the literature [76],[77], [78],[74],[75], to the best of our knowledge, no theoretical models relating to diffuse reflection in an OCT geometry exist in the literature.

For completeness, it should be mentioned that a model of the Wigner phase-space distribution for light backscattered from the bulk of a random medium has been published [80]. In contrast to the analysis presented in this thesis, this model consider the case where the scattering particles are smaller than a wavelength. In this case, the bulk backscattering is stronger due to nearly isotropic scattering, and it is more appropriate to use the diffusion approximation [41] than the extended Huygens-Fresnel principle used in this thesis. Therefore, this model published by Wax *et al.* [80] does not apply to the OCT geometry where the light scattering in the bulk tissue is predominantly in the forward direction.

In section 5.2, on the basis of the extended Huygens-Fresnel principle, we derive a general expression for the Wigner phase-space distribution within the paraxial approximation that is valid in both the single and multiple scattering regimes. This solution is also valid for both an arbitrary small-angle volume scattering function within the paraxial approximation, and (real) optical $ABCD$ systems. In section 5.3 we discuss some general features of the Wigner phase-space distribution function and derive asymptotic results that are valid in the multiple scattering regime. In particular, we investigate two different types of scattering functions: the quadratic type and the linear type.

Because most of the previous published work regarding the Wigner function are carried out for the direct transmission geometry, it is important to note that, within the paraxial approximation, the extended Huygens-Fresnel principle and the $ABCD$ matrix formalism can be used successfully to describe this case. Therefore, for completeness, we present in Appendix C the general closed-form solution for the Wigner phase-space distribution function in $ABCD$ paraxial optical systems for propagation through a random scattering medium, i.e., transmission ge-

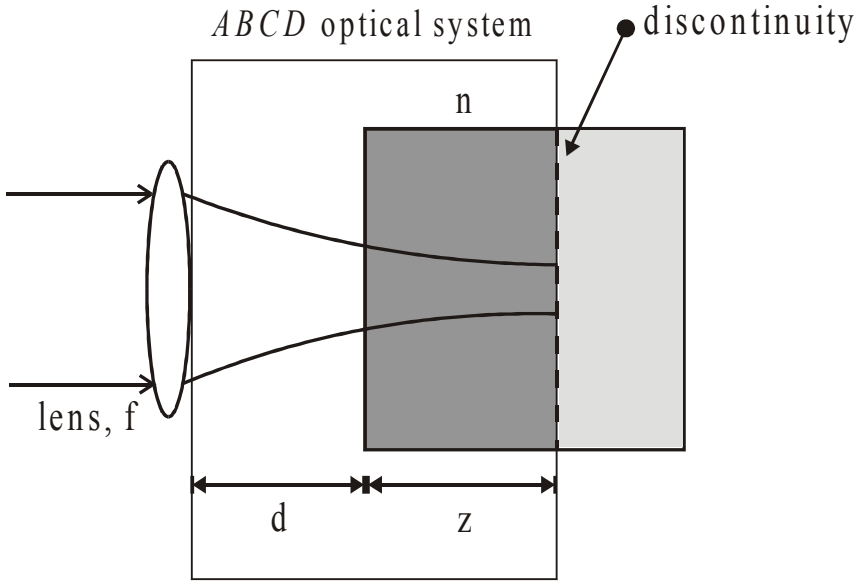

Figure 32. Schematic illustration of the propagation geometry. For clarity, we show the standard OCT geometry, where the focal and discontinuity planes coincide. The discontinuity at a depth z gives rise to diffuse backscattering. In principle, the space between the lens plane and the scattering medium may contain optical elements that are characterized by ABCD ray matrices.

ometry. In particular, for the special case of direct propagation through a spatially uniform random scattering medium, it is noted that the solution of the transport equation in the small-angle approximation is identical to the corresponding solution obtained directly from the extended Huygens-Fresnel principle. This important equivalence is proved in section 5.4. Furthermore, in Appendix D we extend the result of Appendix C to an absorbing medium, where it is pointed out that all previous treatments where absorption effects were included as just an overall attenuation factor are, strictly speaking, incorrect and should be used with caution in applications where absorption effects are important.

In section 5.5, we derive and discuss the Wigner phase-space distribution function in the context of an OCT geometry for both types of scattering functions. Furthermore, a novel method of creating OCT images based on measurements of the momentum width of the Wigner phase-space distribution is proposed.

We note that the theoretical results presented in this chapter and the corresponding appendices, have been obtained in close collaboration with Harold T. Yura [81].

5.2 General considerations

Consider a CW quasi-monochromatic optical wave propagating through a non-absorbing random small-angle scattering medium, reflecting off a discontinuity giving a diffuse reflection and subsequently propagating back to the initial plane. We denote the resulting optical field in the initial plane perpendicular to the optic axis by $U_{\mathrm{S}}(\vec{P})$, where $\vec{P}$ is a two-dimensional vector in this plane. For simplicity in notation, we omit the time dependence. The Wigner phase-space distribution,

$W(\vec{P},\vec{q})$ may be written as [82]

$$W(\vec{P},\vec{q}) = \int \frac{d\vec{p}}{(2\pi)^2} \left\langle U_{\mathrm{S}}(\vec{P}+\vec{p}/2)U_{\mathrm{S}}^{*}(\vec{P}-\vec{p}/2)\right\rangle \exp[i\vec{q}\cdot\vec{p}], \tag{57}$$

where angle brackets denote the ensemble average. That is, the Wigner phase-space distribution function is a two-dimensional Fourier transform of the indicated mutual coherence function $\left\langle U_{\mathrm{S}}(\vec{P}+\vec{p}/2)U_{\mathrm{S}}^{*}(\vec{P}-\vec{p}/2)\right\rangle$ and as such, contains the same information about the optical field as does the mutual coherence function. The quantity $\vec{q}$ is a transverse momentum, and in the small-angle approximation its magnitude q can be related directly to the scattering angle simply as $q = 2k\sin\theta/2 \simeq k\theta$, where k is the free-space wave number. In addition, because in the small-angle approximation the differential element of the solid angle $\mathrm{d}\Omega = 2\pi\sin\theta\mathrm{d}\theta \simeq 2\pi\theta\mathrm{d}\theta = 2\pi q\mathrm{d}q/k^2$, it is easily verified that the integral of $W(\vec{P},\vec{q})$ over all $\vec{q}$ (i.e., over solid angle) equals the intensity $I(\vec{P})$, i.e., $\left|U_{\mathrm{S}}(\vec{P})\right|^2$, at the observation point $\vec{P}$. Hence, to within a multiplicative constant, the Wigner phase-space distribution is equal to the specific radiance distribution of the optical field at the observation point of interest for those cases where the Wigner phase-space distribution is positive definite. More specific, the specific radiance distribution $N(\vec{P},\theta) = k^2W(\vec{P},k\theta)$ within the paraxial approximation.

In the present analysis, we neglect polarization effects, bulk backscattering, and enhanced backscattering, which is obtained very close to the optic axis.

In random media where the scattering particles are large compared with the wavelength and the index of refraction ratio is near unity, the bulk backscattering efficiency is much smaller than the scattering efficiency. Moreover, the scattering is primarily in the forward direction, which is the basis of using the paraxial approximation. Therefore the bulk backscattering may be neglected when one is considering the light propagation problem, since its contribution is small. An example of this is skin tissue with cell sizes of 5-10 μm diameter and index of refraction ratio of $1.45/1.4 = 1.04$.

It is well known that a medium with random scattering inhomogeneities will produce an amplification effect of the mean intensity in the strictly backward direction, as compared with the corresponding intensity obtained in the homogeneous medium [83]. This so-called enhanced backscattering is due to multichannel coherence effects, i.e., interference at a source point between waves transmitted in the forward and backward directions by the same inhomogeneities in the medium. Additionally, because of conservation of energy, enhanced backscattering is accompanied by a corresponding reduction in intensity in directions close to the strictly backward direction. In general, as discussed in Ref. [83], the linear dimension of the region surrounding the strictly backward direction where enhanced backscattering is obtained is of the order of or less than the transverse intensity correlation length, l. The corresponding reduction of intensity occurs near the surface of a cone of angle of the order l/Z, where Z is the one-way propagation distance in the medium. Strictly speaking, enhanced backscattering effects are obtained in situations where the linear dimensions of the illuminated region, a, in the backscattering plane satisfy $a^2 \ll \lambda Z$, where λ is the wavelength. When the radiation at some point $\vec{P}$ in the observation plane results from illuminated regions that are large compared with $\sqrt{\lambda Z}$, $\vec{P}$ will not be in the strictly backscattered direction with respect to the reflected light, and, as a consequence, enhanced backscattering will not be manifested. In all cases considered here $a \gg \sqrt{\lambda Z}$, and therefore enhanced backscattering effects are neglected.

As indicated in Fig. 32, the signal of interest results from diffuse reflection at the discontinuity of interest only. As discussed above, the statistics of the forward- and backpropagating optical waves are assumed here to be independent. This case

was treated in section 2.2, and from Eq. (21) with $\vec{p}_{1,2} = \vec{P} \pm \vec{p}/2$, the extended Huygens-Fresnel solution for the mutual coherence function for diffuse reflection in the discontinuity plane and for observation in the lens plane is given by

$$\left\langle U_{\mathrm{S}}\left(\vec{P}+\vec{p}/2\right) U_{\mathrm{S}}^{*}\left(\vec{P}-\vec{p}/2\right)\right\rangle = \frac{4\pi}{k^2}\int d\vec{r}\,\langle I_B\left(\vec{r}\right)\rangle\, G_0\left(\vec{r},\vec{P}+\vec{p}/2\right) \times G_0^{*}\left(\vec{r},\vec{P}-\vec{p}/2\right)\Gamma_{\mathrm{pt}}\left(p\right). \tag{58}$$

As defined in section 2.2, $\langle I_B\left(\vec{r}\right)\rangle$ is the mean backscattered irradiance distribution in the plane of the discontinuity, and $\Gamma_{\mathrm{pt}}\left(p\right)$ is the mutual coherence function of a point source located in the discontinuity plane and observed in the lens plane, where $p = |\vec{p}_1 - \vec{p}_2|$. Furthermore, $G_0(\vec{r},\vec{p})$, which is the Huygens-Fresnel Green's function for non-scattering homogeneous media when propagating from the discontinuity plane to the lens plane, is given by (Eq. (24))

$$G_0(\vec{r},\vec{p}) = -\frac{ik}{2\pi B_{\mathrm{b}}}\exp\left[-\frac{ik}{2B_{\mathrm{b}}}\left(A_{\mathrm{b}}r^2 - 2\vec{r}\cdot\vec{p} + D_{\mathrm{b}}p^2\right)\right], \tag{59}$$

where A_{b}, B_{b}, and D_{b} are the (real) $ABCD$ ray-matrix elements for backpropagation through the optical system. In Fig. 32 we illustrate for clarity the OCT geometry. However, in principle, the space between the lens plane and the scattering medium may contain optical elements that are characterized by $ABCD$ ray-matrices. To be as general as possible, we assume an arbitrary $ABCD$ optical system between the lens and the discontinuity planes.

For the OCT geometry, we recall that $A_{\mathrm{b}} = D_{\mathrm{b}} = 1$ and $B_{\mathrm{b}} = d + z/n$, where d is the distance from the lens to the tissue surface, n is the mean index of refraction of the tissue, and z is the depth of the discontinuity.

As shown in section 2.2, the mutual coherence function $\Gamma_{\mathrm{pt}}\left(p\right)$ is given by

$$\Gamma_{\mathrm{pt}}(p) = \exp\{-s[1 - b_\phi(p)]\}, \tag{60}$$

where the optical depth $s = \mu_{\mathrm{s}} z$. The quantity μ_{s} is the bulk scattering coefficient, and $b_\phi(p)$ is the normalized phase autocorrelation function of a point source whose origin is in the discontinuity plane given by

$$b_\phi(p) = \frac{\int_0^z dz' \int_0^\infty \sigma(\theta;z') J_0(k p_{\mathrm{s}}\theta)\theta d\theta}{\int_0^z dz' \int_0^\infty \sigma(\theta;z')\theta d\theta}, \tag{61}$$

J_0 is the Bessel function of the first kind, of order zero,

$$p_{\mathrm{s}} = \frac{B_{\mathrm{b}}(z')}{B_{\mathrm{b}}} p, \tag{62}$$

where $B_{\mathrm{b}}(z')$ is the B-matrix element for backpropagation from the discontinuity plane to a distance z', and $\sigma(\theta;z')$ is the volume scattering function as a function of position measured from the discontinuity plane in the optical system. Strictly speaking, Eq. (60) applies to the case where the scattering is in the near-forward direction and all of the scattered light is contained within the collection solid angle of the optical system being used. For propagation in an inhomogeneous medium where appreciable light is scattered outside the collection solid angle, the mutual coherence function of Eq. (60) becomes $\Gamma_{\mathrm{pt}}\left(p\right) = \exp\{-s_{\mathrm{W}} - s_{\mathrm{N}}\left[1 - b_\phi\left(p\right)\right]\}$, where the subscripts N and W refer to the near-forward and wide-angle contributions to the optical depth, respectively [76],[77],[78]. That is, the portion of the light scattered outside the collection solid angle thus appears much like an effective absorption coefficient for propagation in the near-forward direction. We note that all correlation functions of interest here can be expressed directly in terms of the spectral densities through the relation $\sigma\left(\theta\right) = 2\pi k^4 \Phi_{\mathrm{n}}\left(k\theta\right)$, where Φ_{n} is the three-dimensional spectrum of the index of refraction inhomogeneities, and we

have omitted the functional dependence on path length for notational simplicity [60].

For the OCT geometry, we have $\sigma(\theta; z') = \sigma(\theta)$ for $0 \le z' \le z$, and 0 otherwise; $B_{\rm b}(z') = z'/n$ for $0 \le z' \le z$, and $B_{\rm b}(z') = z/n + z' - z$ for $z \le z' \le d + z$.

In this analysis it is assumed that we are dealing with a statistically stationary and isotropic random medium. Then, it is well-known that all second-order spatial correlation functions of the optical field, such as $\Gamma_{\rm pt}(p)$, are functions of the magnitude of the difference of the spatial coordinates and satisfy the identity $\Gamma_{\rm pt}(-p) = \Gamma^*_{\rm pt}(p)$ [60].

Because the point-source mutual coherence function given in Eq. (60) is valid for arbitrary values of s [60], the results given below for the Wigner phase-space distribution function are valid in both the single and the multiple scattering regimes.

Substituting Eqs. (58) and (59) into Eq. (57) and simplifying yields

$$W(\vec{P}, \vec{q}) = \frac{1}{\pi B_{\rm b}^2} \int \frac{d\vec{p}}{(2\pi)^2} \exp\left[i\vec{p} \cdot \left(\vec{q} - \frac{kD_{\rm b}}{B_{\rm b}} \vec{P} \right) \right] \Gamma_{\rm pt}(p) H(\vec{p}), \tag{63}$$

where

$$H(\vec{p}) = \int d\vec{r} \, \langle I_B(\vec{r}) \rangle \exp\left(i \frac{k}{B_{\rm b}} \vec{p} \cdot \vec{r} \right) \tag{64}$$

is related to the Fourier transform of $\langle I_B(\vec{r}) \rangle$. In Appendix E it is shown that

$$H(\vec{p}) = R_{\rm d} \Gamma_{\rm pt}(-p) K(-\vec{p}) = R_{\rm d} \Gamma^*_{\rm pt}(p) K(-\vec{p}), \tag{65}$$

where $R_{\rm d}$ is the reflection coefficient of the discontinuity,

$$K(\vec{r}) = \int d\vec{R} \, U_{\rm Si}\left(\vec{R} + \vec{r}/2 \right) U^*_{\rm Si}\left(\vec{R} - \vec{r}/2 \right) \exp\left(-i \frac{kA}{B} \vec{r} \cdot \vec{R} \right), \tag{66}$$

and $U_{\rm Si}(\vec{r})$ is the initial optical wave function. Substituting Eq. (65) into Eq. (63) yields

$$\begin{aligned} W(\vec{P}, \vec{q}) &= \frac{R_{\rm d}}{\pi B_{\rm b}^2} \int \frac{d\vec{p}}{(2\pi)^2} \left| \Gamma_{\rm pt}(p) \right|^2 K(-\vec{p}) \exp\left[i\vec{p} \cdot \left(\vec{q} - \frac{kD_{\rm b}}{B_{\rm b}} \vec{P} \right) \right] \\ &= \frac{R_{\rm d}}{2\pi^2 B_{\rm b}^2} \int_0^\infty dp p \left| \Gamma_{\rm pt}(p) \right|^2 K(p) J_0\left(\left| \vec{q} - \frac{kD_{\rm b}}{B_{\rm b}} \vec{P} \right| p \right). \\ &\quad \text{(for axially symmetric } U_{\rm Si}) \end{aligned} \tag{67}$$

This is the required general solution for the Wigner phase-space distribution function for diffuse reflection in the paraxial approximation. That is, for a given initial optical wave function and a medium whose scattering function is known, Eq. (67) is the solution for the Wigner phase-space distribution function, i.e., specific radiance. Note that $I(\vec{P}) = \int W(\vec{P}, \vec{q}) d\vec{q} = R_{\rm d} P_0 / \pi B_{\rm b}^2$, where P_0 is the transmitted power. As expected for diffuse reflection, the intensity in the observation plane is constant, independent of position.

5.3 Discussion and special cases

For general scattering functions $\sigma(\theta)$, the integral indicated in Eq. (67) cannot be obtained analytically, although numerical results may be readily obtained. However, some general features of the Wigner phase-space distribution function may be obtained by direct examination of the general formula.

First, examination of Eq. (67) reveals that, in general, the Wigner phase-space distribution attains its maximum along the line given by $\vec{P} = B_{\rm b}\vec{q}/kD_{\rm b} = B_{\rm b}\vec{\theta}/D_{\rm b}$.

Additionally, because $\Gamma_{\rm pt}(p)$ in Eq. (60) can be rewritten as

$$\Gamma_{\rm pt}(p) = e^{-s} + e^{-s}\{\exp[sb_\phi(p)] - 1\}, \tag{68}$$

we may conclude from Eqs. (67) and (68) that in general, the Wigner phase-space distribution function consists of three terms. The square of the first term on the right-hand side of Eq. (68), which corresponds to the ballistic photons, leads to an attenuated distribution of what would be obtained in the absence of the scattering inhomogeneities. The square of the corresponding second term represents a broader halo resulting from multiple scattering in the medium. The third term is a cross term between the ballistic and the multiple scattering contributions. Physically, the cross term is the coherent mixing of the unscattered and the multiple scattered light.

Next, for sufficiently large values of s, examination of Eq. (60) reveals that $\Gamma_{\rm pt}$ is nonzero for $s[1 - b_\phi(p)]$ less than the order unity, that is, for $b_\phi(p)$ near unity. As shown in section 2.2, expanding $b_\phi(p)$ in powers of p and retaining the first two nonzero terms allows one to obtain asymptotic results. In the limit $s \gg 1$, for all cases of practical concern the resulting width of $|\Gamma_{\rm pt}(p)|^2$ is much narrower than $K(p)$, and without loss of generality, we may replace $K(p)$ by its value at the origin $K(0) = P_0$, the transmitted power.

Quadratic-type scattering function

We distinguish between two types of scattering functions $\sigma(\theta)$. The first and most common type is scattering functions that lead to phase correlation functions such that near the origin $b_\phi(p) \simeq 1 - p^2/3\rho_\phi^2$, where ρ_ϕ is the phase correlation length. Such scattering functions include the Gaussian form, which is commonly used in statistical optics [7]. As shown in section 2.2, we get the following equation for $\Gamma_{\rm pt}$ in this case

$$\Gamma_{\rm pt}\,(p) \simeq \exp[-p^2/\rho_0^2], \quad s \gg 1, \tag{69}$$

where ρ_0, the point source lateral coherence length, is given by

$$\rho_0 = \frac{\sqrt{3}\rho_\phi}{\sqrt{s}}. \tag{70}$$

For the $ABCD$ system indicated in Figure 32 it follows from Appendix A that

$$\rho_0 = \sqrt{\frac{3}{s}}\frac{\lambda}{\pi\theta_{\rm rms}}\left(\frac{nB_{\rm b}}{z}\right), \tag{71}$$

where λ is the wavelength, and $\theta_{\rm rms}$ is the root-mean-square scattering angle given by [54]

$$\theta_{\rm rms} = \sqrt{\frac{\int_0^\infty d\theta\,\theta\,\sigma(\theta)\theta^2}{\int_0^\infty d\theta\,\theta\,\sigma(\theta)}}. \tag{72}$$

It is assumed here that all scattering functions of interest are such that the integrals indicated in Eq. (72) are finite. We note that the so-called shower curtain effect is represented by the term in parentheses on the right-hand side of Eq. (71), as discussed in section 2.2. In view of Eq. (68), an analytic engineering approximation for the point-source mutual coherence function for scattering functions that have a quadratic dependence on spatial separation near the origin, valid for arbitrary values of s, is given by

$$\Gamma_{\rm pt}(p) \simeq e^{-s} + (1 - e^{-s})\exp[-p^2/\rho_0^2]\,. \tag{73}$$

Substituting Eq. (69) into Eq. (67), and performing the integration yields for $s \gg 1$ that

$$W(\vec{P},\vec{q}) = \frac{P_0\rho_0^2 R_\mathrm{d}}{2\pi(2\pi B_\mathrm{b})^2}\exp\left[-\frac{\rho_0^2}{8}\left|\vec{q}-\frac{kD_\mathrm{b}}{B_\mathrm{b}}\vec{P}\right|^2\right]. \tag{74}$$

Linear-type scattering function

A second type of scattering function is one that leads to a phase correlation function that has a linear dependence on spatial separation near the origin. An example of such a function is the Henyey-Greenstein scattering function [56], which has been widely used in approximating the angular scattering dependence of single-scattering events in some biological media [57],[52]. This function is given by [84]

$$\sigma(\theta) = \frac{1}{4\pi}\frac{1-g^2}{(1+g^2-2g\cos\theta)^{3/2}}, \tag{75}$$

where θ is the scattering angle and g, the asymmetry parameter [53], is defined as

$$g = \frac{\int_0^\pi \sigma(\theta)\cos\theta\sin\theta d\theta}{\int_0^\pi \sigma(\theta)\sin\theta d\theta}. \tag{76}$$

Here we are concerned with the case of small-angle forward scattering where g is greater than ~ 0.9. For sufficiently small θ, we have that $\cos\theta \simeq 1-\theta^2/2$, and Eq. (75) becomes

$$\sigma(\theta) \simeq \frac{1}{4\pi}\frac{1-g^2}{(\theta_\mathrm{HG}^2+\theta^2)^{3/2}}, \quad \theta \ll 1, \tag{77}$$

where

$$\theta_\mathrm{HG} = \frac{1-g}{\sqrt{g}}. \tag{78}$$

Substituting Eq. (77) into Eq. (61) and performing the indicated integration yields

$$b_\phi(p) = \frac{1-\exp[-p/r_0]}{p/r_0}, \tag{79}$$

where the Henyey-Greenstein phase correlation length, r_0, is given by

$$r_0 = \frac{1}{k\theta_\mathrm{HG}}\left(\frac{nB_\mathrm{b}}{z}\right) = \frac{\lambda\sqrt{g}}{2\pi(1-g)}\left(\frac{nB_\mathrm{b}}{z}\right). \tag{80}$$

The so-called shower curtain effect is represented by the term in parentheses on the right-hand side of Eq. (80). Near the origin, we have that $b_\phi(p) \simeq 1-p/2r_0$. That is, for the Henyey-Greenstein scattering function, the corresponding phase correlation function near the origin has a linear dependence on spatial separation. As a result, we obtain

$$\Gamma_\mathrm{pt}(p) = \exp\left[-sp/2r_0\right] \quad \text{for } s \gg 1. \tag{81}$$

Similarly, the corresponding analytic engineering approximation for the point-source mutual coherence function for scattering functions that have a linear dependence on spatial separation near the origin, valid for arbitrary values of s, is given by

$$\Gamma_\mathrm{pt}(p) \simeq e^{-s} + (1-e^{-s})\exp\left[-sp/2r_0\right]. \tag{82}$$

Substituting Eq. (81) into Eq. (67) and performing the indicated integration yields for $s \gg 1$ that

$$W(\vec{P},\vec{q}) = \frac{P_0 R_\mathrm{d}}{\pi(2\pi B_\mathrm{b})^2}\left(\frac{r_0}{s}\right)^2\frac{1}{\left(1+\left(\frac{r_0}{s}\right)^2\left|\vec{q}-\frac{kD_\mathrm{b}}{B_\mathrm{b}}\vec{P}\right|^2\right)^{3/2}}. \tag{83}$$

5.4 The transmission geometry

Because most of the previous published work regarding the Wigner function has been carried out for the direct transmission geometry using radiation transport theory, it is important to note that, within the paraxial approximation, the extended Huygens-Fresnel principle and the $ABCD$ matrix formalism may also be used successfully to describe this case.

Therefore, for completeness, we present in Appendix C the general closed-form solution for the Wigner phase-space distribution function in $ABCD$ paraxial optical systems for propagation through a random scattering medium.

Furthermore, in Appendix D, we extend the results of Appendix C to an absorbing medium. It is pointed out in Appendix D that all previous treatments where absorption effects are included as just an overall attenuation factor are, strictly speaking, incorrect and should be used with caution in applications where absorption effects are important.

Spatially uniform random scattering medium

In all cases considered in this thesis, as well as in Refs. [73], [76],[77],[78],[74],[75], the Wigner phase-space distribution function is positive definite [79], and hence the Wigner function and the specific radiance may be used interchangeably.

Using the paraxial approximation and the extended Huygens-Fresnel principle, Yura [85] obtained a closed-form solution for the Wigner phase-space distribution function that is valid for one-way propagation through a random medium characterized by an arbitrary small-angle scattering function, that is independent of position along the propagation path. Yura's result is given in Eqs. (C.1)-(C.6) using the present notation and Fourier transform sign convention. This result is easily extended to an arbitrary $ABCD$ optical system by using the extended Huygens-Fresnel principle, and the result is given in Appendix C.

As indicated by Yura in Ref. [85], his result for the Wigner function is identical to the result of Arnush [86], who first obtained the corresponding solution for the Wigner function based on the solution of the full transport equation within the small-angle approximation. In this regard we note that the transport equation solved by the authors of Refs. [76],[77],[78],[75] is identical to that solved by Arnush, and as a consequence one must view the solution for the Wigner function given in Refs. [76],[77],[78],[75] as a "rediscovery" of previous known results. No solution of the corresponding transport equation for arbitrary $ABCD$ optical systems is available in the literature.

The important equivalence of solutions obtained by using the Boltzmann equation in the small-angle approximation and the extended Huygens-Fresnel principle is proven below. This is done by showing that the result obtained by Arnush [86] is identical to the result of Yura [85], which is given in Eqs. (C.1)-(C.6). Note that the result given in Eqs. (C.1)-(C.6) is for the Wigner function W.

Arnush's result for the specific radiance, which is given in Eq. (9) of Ref. [86], is expressed as

$$f\left(\vec{u},\vec{r},z\right) = \left(2\pi\right)^{-4} e^{-\mu_{\mathrm{a}}z} \iint d^2k d^2p F_0\left(\vec{p}+z\vec{k},\vec{k}\right) G\, e^{i\left(\vec{p}\cdot\vec{u}+\vec{k}\cdot\vec{r}\right)}, \tag{84}$$

$$G = \exp\left[-\mu_{\mathrm{s}}z + \mu_{\mathrm{s}}\int_0^z d\xi Q\left(\vec{p}+\xi\vec{k}\right)\right], \tag{85}$$

where $\vec{u}$ is a given ray direction at the point $(\vec{r},z)$ in a cylindrical coordinate system, and z is the propagation distance. Note that the symbols used in the present thesis for the volume absorption coefficient and the scattering coefficient

have been applied. Using Eq. (6) of Arnush [86], $F_0(\vec{p}+z\vec{k},\vec{k})$ is given by

$$F_0\left(\vec{p}+z\vec{k},\vec{k}\right)=\iint d^2r'd^2u'e^{-i(\vec{k}\cdot\vec{r}'+(\vec{p}+z\vec{k})\cdot\vec{u}')}f_0\left(\vec{u}',\vec{r}'\right), \tag{86}$$

where $f_0\left(\vec{u}',\vec{r}'\right)$ is the specific radiance at $z=0$, and $\vec{u}'$ is a given ray direction at the point $(\vec{r}',0)$ in the cylindrical coordinate system. Furthermore, using Eq. (7) of Arnush [86], $Q(\vec{p}+\xi\vec{k})$ is given by

$$Q\left(\vec{p}+\xi\vec{k}\right)=\int d^2u\,e^{-i\vec{u}\cdot(\vec{p}+\xi\vec{k})}\Sigma\left(\vec{u}\right), \tag{87}$$

where $\Sigma\left(\vec{u}\right)$ is the normalized scattering function. The volume scattering function is given by $\mu_{\rm s}\Sigma\left(\vec{u}\right)$. We consider nonabsorbing media, so $\mu_{\rm a}=0$ in the following. Furthermore, for simplicity, we consider the case where the index of refraction of the medium is 1.

Substituting Eq. (86) into Eq. (84) yields

$$\begin{aligned} f\left(\vec{u},\vec{r},z\right) &= (2\pi)^{-4}\iint d^2kd^2p\iint d^2r'd^2u'G\,f_0\left(\vec{u}',\vec{r}'\right) \\ &\quad\times\exp\left[i\left(\vec{p}\cdot\left(\vec{u}-\vec{u}'\right)+\vec{k}\cdot\left(\vec{r}-\vec{r}'-z\vec{u}'\right)\right)\right]. \end{aligned} \tag{88}$$

Equation (88) can now be compared directly with Eqs. (C.1) and (C.3). The quantity G corresponds to $F\left(\vec{p},\vec{r}\right)$ given by Eqs. (C.4)-(C.6). By using the following changes of variables it is straightforward to show that the result obtained by Arnush [86] is identical to the result of Yura [85]: $\vec{r}'=\vec{R}-Z\vec{q}'/k$, $\vec{k}=\frac{k_{\rm m}}{Z}(\vec{r}_{\rm EHF}-\vec{p}_{\rm EHF})$, $\vec{u}'=\vec{q}'/k$, $\vec{u}=\vec{q}/k=\vec{\theta}$, $\vec{p}=k\vec{p}_{\rm EHF}$, $\vec{r}=\vec{P}$, $z=Z$, and $\xi=z'$. Note the use of the subscript "EHF" for *extended Huygens-Fresnel* in order to avoid confusion regarding notation.

5.5 Applications to optical coherence tomography

It follows from the analysis in section 2.2 that the SNR in a standard OCT system can be expressed as

$$\begin{aligned} SNR &= \text{constant} \\ &\quad\times\mathrm{Re}\left[\iint\Gamma_{\rm R}(\vec{P}+\vec{p}/2,\vec{P}-\vec{p}/2)\,\Gamma_{\rm S}(\vec{P}+\vec{p}/2,\vec{P}-\vec{p}/2)d\vec{P}d\vec{p}\right], \end{aligned} \tag{89}$$

where Re denotes the real part, and $\Gamma_{\rm R}$ and $\Gamma_{\rm S}$ are the mutual coherence functions of the deterministic reference beam and the sample beam, respectively, in the mixing plane. Because the Wigner phase-space distribution function and the mutual coherence function are Fourier transform related, the SNR can be rewritten as

$$SNR=\text{constant}\times\mathrm{Re}\left[\iint W_{\rm R}(\vec{P},-\vec{q})W_{\rm S}(\vec{P},\vec{q})d\vec{P}d\vec{q}\right], \tag{90}$$

where $W_{\rm R}$ and $W_{\rm S}$ are the corresponding Wigner phase-space distribution functions of the reference and the sample beams, respectively. Eq. (90) indicates, in particular, that the SNR of a standard OCT system is related globally to the Wigner phase-space distribution function of the sample beam. That is, images obtained from standard OCT systems contain global, rather than local, information of the Wigner phase-space distribution function of the sample beam.

Improved OCT imagery can thus be obtained only from systems that make use of the local properties of the Wigner phase-space distribution function, rather than globally where information is inevitably lost. Below we derive expressions for

the Wigner phase-space distribution function of the sample beam for a standard OCT geometry for both classes of scattering functions discussed in section 5.3.

Consider an OCT system where the initial optical wave function, i.e., immediately following the lens, is given by

$$U_{\mathrm{Si}}(r) = \sqrt{\frac{P_0}{\pi w_0^2}} \exp\left[-\frac{r^2}{2}\left(\frac{1}{w_0^2} + \frac{ik}{f}\right)\right], \tag{91}$$

where w_0 is the initial $1/e$ intensity radius and f is the focal length. For an OCT system that is focused at a tissue discontinuity at depth z, i.e., $B = f$, we then get the following equation

$$K(r) = P_0 \exp\left[-\frac{r^2}{4w_0^2}\right]. \tag{92}$$

Quadratic-type scattering function

We now obtain analytic engineering approximations for the Wigner phase-space distribution function, valid for all values of s, for b_ϕ that are quadratic near the origin. Substituting Eqs. (73) and (92) into Eq. (67) and simplifying yields

$$\begin{aligned} W(\vec{P},\vec{q}) \;\simeq\; & \frac{R_{\mathrm{d}} P_0 4w_0^2}{(2\pi f)^2}[e^{-2s}\exp\left(-Q^2 w_0^2\right) \\ & + e^{-s}(1-e^{-s})\frac{\tilde{\rho}_0^2}{4w_0^2}\exp\left(-\frac{Q^2\tilde{\rho}_0^2}{4}\right) \\ & + (1-e^{-s})^2\frac{\tilde{\rho}_0^2}{8w_0^2}\exp\left(-\frac{Q^2\tilde{\rho}_0^2}{8}\right)], \end{aligned} \tag{93}$$

where

$$\frac{1}{\tilde{\rho}_0^2} = \frac{1}{\rho_0^2} + \frac{1}{4w_0^2}, \tag{94}$$

ρ_0 is given by Eq. (71) with $B_{\mathrm{b}} = f$, and

$$Q = \left|\vec{q} - \frac{k}{f}\vec{P}\right|. \tag{95}$$

The first, second, and third terms on the right-hand side of Eq. (93) represent the ballistic, cross, and multiple scattering contributions, respectively, to the Wigner phase-space distribution function discussed below Eq. (68).

In the limit of $s \ll 1$, examination of Eq. (93) reveals that for $\vec{P} = 0$, the $1/e$ transverse momentum width, Δ_{q}, of the Wigner phase-space distribution is given by $\Delta_{\mathrm{q}} = 1/w_0$. Furthermore, in the limit $s \gg 1$, $\Delta_{\mathrm{q}} = 2\sqrt{2}\tilde{\rho}_0^{-1}$, where $\tilde{\rho}_0 \cong \rho_0$. In this case, $\Delta_{\mathrm{q}} \propto z^{3/2}$ in the presence of the shower curtain effect, which, as discussed above, manifests itself in the standard OCT geometry. For comparison, $\Delta_{\mathrm{q}} \propto z^{1/2}$ in the absence of the shower curtain effect.

Linear-type scattering function

We have not been able to obtain a corresponding analytic approximation, valid for all values of s, for the Henyey-Greenstein type of scattering function. For this case we can only conclude that

$$W(\vec{P},\vec{q}) \simeq \frac{R_{\mathrm{d}} P_0}{(2\pi f)^2}(1-2s)\exp\left[-Q^2 w_0^2\right] \quad \text{for } s \ll 1, \tag{96}$$

and that

$$W(\vec{P},\vec{q}) \simeq \frac{R_{\mathrm{d}}P_0}{\pi(2\pi f)^2}\left(\frac{r_0}{s}\right)^2 \frac{1}{\left(1+\left(\frac{r_0}{s}\right)^2\left|\vec{q}-\frac{k}{f}\vec{P}\right|^2\right)^{3/2}} \quad \text{for } s \gg 1, \tag{97}$$

where r_0 is given by Eq. (80) with $B_{\mathrm{b}} = f$. In the limit of $s \ll 1$, examination of Eq. (96) reveals that for $\vec{P} = 0$, the $1/e$ transverse momentum width, Δ_{q}, of the Wigner phase-space distribution is given by $\Delta_{\mathrm{q}} = 1/w_0$. Furthermore, in the limit $s \gg 1$, it is obtained from Eq. (97) that $\Delta_{\mathrm{q}} = s/r_0$. In this case, $\Delta_{\mathrm{q}} \propto z^2$ in the presence of the shower curtain effect. For comparison, $\Delta_{\mathrm{q}} \propto z$ in the absence of the shower curtain effect.

It is important to note that for both types of scattering functions, the momentum width increases with increasing depth as z^γ, with considerably larger values of γ being obtained in the presence of the shower curtain effect. Furthermore, the actual value of γ is strongly dependent on the details of the scattering function.

Improved OCT imagery

As shown above, it is possible to determine the lateral coherence length of the sample field from measurements of the Wigner phase-space distribution. As is evident from Eq. (71), the lateral coherence length depends on the optical parameters of the tissue, i.e., n, μ_{s}, and θ_{rms}. Therefore, it is feasible to create images based on measurements of the lateral coherence length as a function of position in the tissue. In contrast to OCT signals used to create conventional OCT images, the lateral coherence length is related only to the propagation of the light in the tissue, and its magnitude is independent of the amount of light backscattered or reflected at the probed depth. In general, a discontinuity between two tissue layers is characterized by a change in the scattering coefficient, the backscattering coefficient, and the index of refraction. The relative change in the scattering coefficient and the backscattering coefficient is markedly greater than the corresponding relative change in the index of refraction [52]. In human skin tissue, for example, the scattering coefficients of epidermis and dermis are $50\,\mathrm{mm}^{-1}$ and $21.7\,\mathrm{mm}^{-1}$, respectively, while the indices of refraction lie in the range $1.37 - 1.5$ [52]. On this basis, it may be shown from the analysis above that an imaging system based on measurements of the lateral coherence length may have a higher sensitivity to changes in the scattering coefficient than the conventional OCT system that probes the corresponding change in the backscattering coefficient. The higher sensitivity may lead to an improved contrast in the obtained image. These statements assume adequate measurements of the Wigner phase-space distribution of the sample field.

It should be mentioned here that methods have been developed for measuring Wigner phase-space distributions using both coherent [75],[87],[78] and low-coherence [88],[89],[90],[87],[80] light sources. This model and the above discussion gives more insight into the ideas presented recently that new venues for medical imaging may be based on coherence tomography with use of measurements of Wigner phase-space distributions [73, 74, 75].

5.6 Summary

Using the extended Huygens-Fresnel principle, we have obtained a closed-form solution for the Wigner phase-space distribution function for diffuse reflection and small-angle scattering in a nonabsorbing random medium. The analysis is applicable in both the single and multiple scattering regimes and it is general

in the sense that it applies to both an arbitrary small-angle volume scattering function and (real) $ABCD$ optical systems.

In particular, we obtained analytic results applicable to OCT systems, where the corresponding depth dependence of the Wigner phase-space distribution was discussed. A novel method of creating OCT images based on measurements of the momentum width of the Wigner phase-space distribution has been suggested. Moreover, the advantage over conventional OCT has been discussed, i.e., a higher sensitivity to changes in the scattering coefficient.

Finally, the Wigner phase-space distribution function for the transmission geometry has been investigated. The important equivalence of solutions obtained by using the transport equation in the small-angle approximation and the extended Huygens-Fresnel principle has been verified.

6 Conclusion

A new theoretical description of the optical coherence tomography (OCT) technique when used for imaging in highly scattering tissue has been developed. The description is based on the extended Huygens-Fresnel principle. It is shown that the theoretical model describes the performance of the OCT system in both the single and multiple scattering regimes simultaneously. The model inherently includes the shower curtain effect. This effect has been omitted in previous theoretical models of OCT systems. It has been demonstrated that the shower curtain effect is of utmost importance in the theoretical description of an OCT system.

The analytical model enables a calculation of the signal-to-noise ratio (SNR), where the optical properties of the tissue have been taken into account. A method for calculating the maximum probing depth based on the SNR has been presented. Furthermore, the model enables the determination of the lateral resolution of the OCT system at arbitrary depths in the scattering tissue.

The new OCT model has been verified by measurements on liquid phantoms consisting of aqueous suspensions of microspheres, and solid phantoms.

In the two experiments with liquid phantoms and a specular reflection, excellent agreement between theory and experiment were obtained for the heterodyne efficiency factor as a function of the scattering coefficient. This agreement was obtained without any kind of fitting.

In the experiment with liquid phantoms and a diffuse backscattering, it was demonstrated how the shower curtain effect increases the heterodyne signal through enhanced spatial coherence of the multiple scattered light. The validity of the model in the case of diffuse backscattering was further supported by an experiment with solid phantoms.

The measurements were carried out by using a conventional OCT setup, which has been constructed during the Ph.D. thesis project.

In order to demonstrate the imaging capabilities of the OCT system, images of human skin, a mouse ear, and a table tennis ball have been obtained.

A new true-reflection OCT imaging algorithm has been presented, and the principle has been demonstrated experimentally by measurements on a solid phantom. This algorithm facilitates making images, which give a direct measure of the amount of light reflected at a given position by correcting for the scattering effects, hence the label *true-reflection OCT*. Such images may be easier to interpret than conventional OCT images.

Using the extended Huygens-Fresnel principle, a closed-form solution for the Wigner phase-space distribution function for diffuse reflection and small-angle scattering in a nonabsorbing random medium have been obtained. The analysis is applicable in both the single and multiple scattering regimes and it is general in the sense that it applies to both an arbitrary small-angle volume scattering function and (real) $ABCD$ optical systems.

In particular, we obtained analytic results applicable to OCT systems, where the corresponding depth dependence of the Wigner phase-space distribution was discussed. A novel method of creating images based on measurements of the momentum width of the Wigner phase-space distribution has been suggested. Moreover, the advantage over conventional OCT has been discussed, i.e., a higher sensitivity to changes in the scattering coefficient.

Finally, the Wigner phase-space distribution function for the transmission geometry has been investigated. The important equivalence of solutions obtained by

using the transport equation in the small-angle approximation and the extended Huygens-Fresnel principle has been verified.

6.1 Perspective

The analytical model enables a calculation of the SNR, where the optical properties of the tissue have been taken into account. This is an important tool in the design of future OCT systems. The model may be extended to more layers having different optical properties, thereby enabling a more realistic modeling for certain types of tissues. Moreover, such modeling is imperative for the true-reflection OCT imaging algorithm.

The true-reflection OCT imaging algorithm, which facilitates making images that give a direct measure of the amount of light reflected at a given position, will need to be further investigated. A demonstration of the potential of the algorithm on OCT images of tissue will hopefully verify that the processed images are easier to interpret than conventional images. Hence, enhanced diagnostic procedures may be envisioned.

A novel method of creating images based on measurements of the momentum width of the Wigner phase-space distribution has been suggested in the thesis. An interesting future development would be the experimental demonstration of the suggested imaging technique. This technique will provide the medical doctor with a new type of image that will contain additional information compared to conventional OCT images. Again, such imaging may also enhance diagnostic procedures.

A Derivation of the lateral coherence length for the OCT geometry

This appendix contains the derivation of the equation of the lateral coherence length $\rho_0(z)$ for the OCT geometry in the case of spherical waves.

A direct application of ABCD ray-matrix theory [49] to the work of Lutomirski [91] yields, that the spherical wave mutual coherence function $\Gamma_{\rm pt}(\rho)$, for an inhomogeneous scattering medium, can be expressed as

$$\Gamma_{\rm pt}(\rho) = \exp\left[-\frac{\rho^2}{4}\int_0^L k^2\theta_{\rm rms}^2(z')\,\mu_{\rm s}(z')\left[\frac{B_{\rm b}(z')}{B(L)}\right]^2 dz'\right], \tag{A.1}$$

where the propagation variable z' is measured from the location of the point source, i.e., the tissue discontinuity plane, and L is the distance from the point source to the observation plane, i.e., the lens plane. For the OCT geometry, the matrix elements $B_{\rm b}(z')$ and $B(L)$ in Eq. (A.1) are defined as

$$B_{\rm b}(z') = \frac{z'}{n}, \quad 0 \le z' \le z \tag{A.2}$$

$$B(L) = B_{\rm b} = B = d + \frac{z}{n}. \tag{A.3}$$

Furthermore, the scattering coefficient $\mu_{\rm s}(z')$ and the root mean square scattering angle $\theta_{\rm rms}(z')$ are given by

$$\mu_{\rm s}(z') = \begin{cases} \mu_{\rm s}, & 0 \le z' \le z \\ 0, & z < z' \le L \end{cases} \tag{A.4}$$

and

$$\theta_{\rm rms}(z') = \begin{cases} \theta_{\rm rms}, & 0 \le z' \le z \\ 0, & z < z' \le L \end{cases} \tag{A.5}$$

Substituting Eqs. (A.2)–(A.5) and $k = 2\pi/\lambda$ into Eq. (A.1) and performing the integration yields

$$\Gamma_{\rm pt}(\rho) = \exp\left[-\frac{\rho^2\pi^2\theta_{\rm rms}^2\mu_{\rm s}z}{3\lambda^2}\,\frac{z^2}{(nd+z)^2}\right]. \tag{A.6}$$

Using that for large phase variances $\Gamma_{\rm pt}(\rho)$ should be on the form $\exp\left[-\rho^2/\rho_0^2\right]$ [54], we get the following expression for the lateral coherence length $\rho_0(z)$ in the case of spherical waves

$$\rho_0(z) = \sqrt{\frac{3}{\mu_{\rm s}z}}\,\frac{\lambda}{\pi\theta_{\rm rms}}\left(1 + \frac{nd(z)}{z}\right). \tag{A.7}$$

B Comparison between the analytic approximation and the exact numerical calculation of the heterodyne efficiency factor

A comparison between the analytic approximation and the exact numerical calculation of the heterodyne efficiency factor as a function of $\mu_{\rm s}$ for $z = 0.5\,\text{mm}$ is

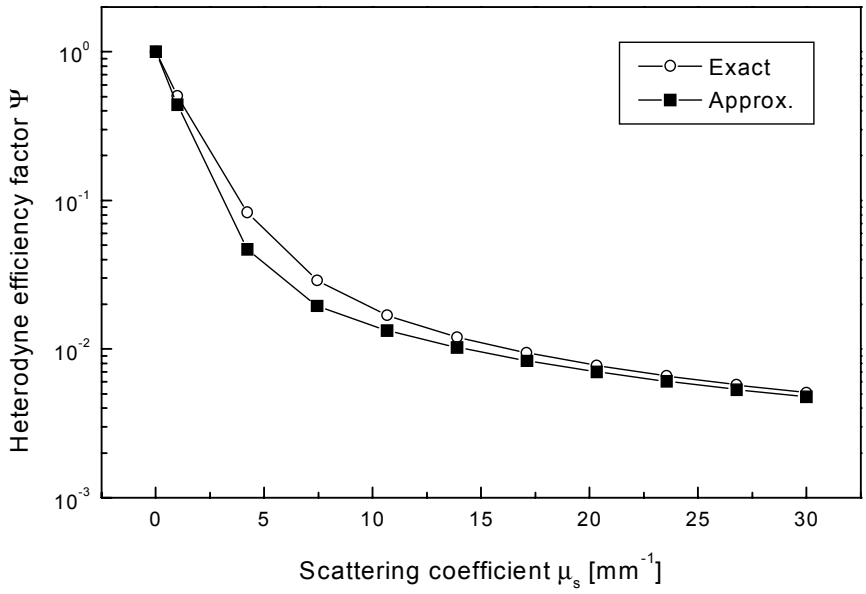

Figure 33. Comparison between the analytic approximation and the exact numerical calculation of the heterodyne efficiency factor as a function of μ_s *for* $z = 0.5\,\mathrm{mm}$ ($\lambda = 814\,\mathrm{nm}$, $g = 0.955$ ($\theta_{\mathrm{rms}} = 0.3\,\mathrm{rad}$), $n = 1.4$, $f = 16\,\mathrm{mm}$, $w_0 = 0.125\,\mathrm{mm}$).

shown in Fig. 33 for the Gaussian scattering function. The case of diffuse backscattering at the discontinuity, and inclusion of the shower curtain effect is considered in this comparison. The term analytic approximation refers to the expression for the heterodyne efficiency factor given in Eq. (27). The exact numerical calculation of the heterodyne efficiency factor has been carried out by using the exact expression for the intensity, given in Eq. (45), and following the same procedure for the determination of Ψ as given in section 2.2.

The main conclusion is that the analytic approximation and the exact numerical calculation for the Gaussian scattering function agrees well for optical depths less than unity and larger than 7-8 [91]. In the intermediate region, the approximation shows some deviation. However, even in this region it is still considered useful.

C The Wigner phase-space distribution function in *ABCD* paraxial optical systems for direct propagation through random media without absorption

In all cases considered in this thesis, as well as in Refs. [73], [76],[77],[78],[74],[75], the Wigner phase-space distribution function is positive definite, and hence the Wigner function and the specific radiance can be used interchangeably. Using the paraxial approximation and the extended Huygens-Fresnel principle, Yura [85] obtained a closed-form solution for the Wigner phase-space distribution function that is valid for one-way propagation through a random medium characterized by an arbitrary small-angle scattering function, which is independent of position

along the propagation path. As indicated by Yura in Ref. [85], his result for the Wigner function is identical to the result of Arnush [86], who first obtained the corresponding solution for the Wigner function based on the solution of the full transport equation, i.e., the Boltzmann equation in the small-angle approximation. In this regard we note that the transport equation solved by the authors of Refs. [76],[77],[78],[75] is identical to that solved by Arnush, and as a consequence one must view the solution for the Wigner function given in Refs. [76],[77],[78],[75] as a "rediscovery" of previous known results.

Here we present the solution for the Wigner distribution function, based on the extended Huygens-Fresnel principle that applies to one-way propagation through an arbitrary (real) $ABCD$ paraxial optical system [49, 51]. That is, we consider the case of paraxial-wave propagation through any optical system that can be characterized by a real $ABCD$ ray-matrix, i.e., a cascaded series of lenses, mirrors, inclined parallel plates, and sections of free space and a section of inhomogeneous scattering that can be situated anywhere along the optical path. Using both the present notation and Fourier transform sign convention, Yura's result for the Wigner distribution function, $W(\vec{P},\vec{q})$, for propagation a distance Z through a spatially uniform random scattering medium of bulk index of refraction n can be expressed as [85]

$$W(\vec{P},\vec{q};Z) = \iint d\vec{R}d\vec{q}'H(\vec{P}-\vec{R},\vec{q}-\vec{q}';Z)W(\vec{R}-Z\vec{q}'/k,\vec{q}';0), \qquad \text{(C.1)}$$

where $W(\vec{R},\vec{q};0)$ is the (assumed given) Wigner function in the initial plane, i.e., in the plane $Z=0$, given by

$$W\left(\vec{R},\vec{q};0\right) = \int \frac{d\vec{r}}{(2\pi)^2}\left\langle U_0\left(\vec{R}+\vec{r}/2\right)U_0^*\left(\vec{R}-\vec{r}/2\right)\right\rangle \exp\left[i\vec{q}\cdot\vec{r}\right], \qquad \text{(C.2)}$$

where U_0 is the initial optical field,

$$\begin{aligned} H\left(\vec{P}-\vec{R},\vec{q}-\vec{q}';Z\right) &= \left(\frac{k_{\rm m}}{4\pi^2 Z}\right)^2 \iint d\vec{p}d\vec{r}F\left(\vec{p},\vec{r}\right) \\ &\quad \times \exp\left[i\frac{k_{\rm m}}{Z}\left(\vec{r}-\vec{p}\right)\cdot\left(\vec{P}-\vec{R}\right)\right] \\ &\quad \times \exp\left[i\vec{p}\cdot\left(\vec{q}-\vec{q}'\right)\right], \end{aligned} \qquad \text{(C.3)}$$

$k_{\rm m} = 2\pi n/\lambda$ is the optical wave number in the medium,

$$F\left(\vec{p},\vec{r}\right) = \exp\left\{-s[1-f(\vec{p},\vec{r})]\right\}, \qquad \text{(C.4)}$$

$$s = \int_0^Z dz' \int d\vec{\theta}\,\sigma(\vec{\theta}) = \mu_{\rm s}Z \qquad \text{(C.5)}$$

is the optical depth associated with the small-angle scattering, $\sigma(\vec{\theta})$ is the volume scattering function, and

$$f\left(\vec{p},\vec{r}\right) = \frac{1}{s}\int_0^Z dz' \int d\vec{\theta}\sigma(\vec{\theta})\exp\left\{ik\vec{\theta}\cdot\left[\frac{z'}{Z}\vec{r}+\left(1-\frac{z'}{Z}\right)\vec{p}\right]\right\}. \qquad \text{(C.6)}$$

Equation (C.1) relates the Wigner distribution function in the initial plane to the Wigner function at propagation distance Z, and hence the quantity H can be interpreted as the propagation kernel for the Wigner distribution function. This kernel contains all of the propagation effects of the intervening space. For propagation in a spatially uniform medium, H is a function of both $\vec{P}-\vec{R}$ and $\vec{q}-\vec{q}'$. As discussed in Ref. [85], Eq. (C.1) is identical to the corresponding result presented in Ref. [86] that was obtained by solving the transport equation in the small-angle approximation. This important equivalence is proved in section 5.4.

In contrast to methods that are based on the transport equation, the generalization of Eq. (C.1) to an arbitrary $ABCD$ optical system by using the extended Huygens-Fresnel principle is straightforward. By using the free-space Green's function given by [49]

$$G_0(\vec{r},\vec{p}) = -\frac{ik}{2\pi B}\exp\left[-\frac{ik}{2B}\left(Ar^2 - 2\vec{r}\cdot\vec{p} + Dp^2\right)\right], \tag{C.7}$$

we can show that

$$W(\vec{P},\vec{q};Z) = \iint d\vec{R}d\vec{q}'H(\vec{P},\vec{R},\vec{q},\vec{q}';Z)W(\vec{R}-B\vec{q}'/k,\vec{q}';0), \tag{C.8}$$

where the Wigner propagation kernel for the $ABCD$ system is given by

$$\begin{aligned} H\left(\vec{P},\vec{R},\vec{q},\vec{q}';Z\right) &= \left(\frac{k}{4\pi^2 B}\right)^2 \iint d\vec{p}d\vec{r}F\left(\vec{p},\vec{r}\right) \\ &\quad\times\exp\left\{i\frac{k}{B}\left[\vec{R}\cdot\left(\vec{p}-A\vec{r}\right)-\vec{P}\cdot\left(D\vec{p}-\vec{r}\right)\right]\right\} \\ &\quad\times\exp\left[i\vec{p}\cdot\left(\vec{q}-\vec{q}'\right)+i\vec{q}'\cdot\vec{r}(A-1)\right], \end{aligned} \tag{C.9}$$

where A, B, and D are the (real) $ABCD$ ray-matrix elements for backpropagation through the optical system, i.e., from the observation plane to the initial plane,

$$F(\vec{p},\vec{r}) = \exp\left\{-s[1-f(\vec{p},\vec{r})]\right\}, \tag{C.10}$$

$$\begin{aligned} f(\vec{p},\vec{r}) &= \frac{1}{s}\int_z^{z+\Delta z} dz' \int d\vec{\theta}\,\sigma(\vec{\theta};z') \\ &\quad\times\exp\left\{ik\vec{\theta}\cdot\left[\frac{B(z')}{B}\vec{r}+\left(1-\frac{B(z')}{B}\right)\vec{p}\right]\right\}, \end{aligned} \tag{C.11}$$

where $\sigma(\vec{\theta};z')$ is the volume scattering function as a function of position measured from the observation plane, $B(z')$ is the B-matrix element for backpropagation from the observation plane to the distance z', and $s = \mu_s\Delta z$ is the optical depth of the scattering layer that is located between $z' = z$ and $z' = z+\Delta z$. The advantage of this formulation, as well as in all propagation-kernel-type solutions, is the separation of the geometry of the problem (which is defined by the spatial/momentum extent and form of the initial Wigner distribution function) from the propagation problem (which is defined by the propagation kernel H and contains all of the effects of the intervening optical system and random scattering medium). In contrast to propagation through a spatially uniform medium, the propagation kernel H for $ABCD$ systems is a function of $\vec{P},\vec{R},\vec{q}'$,and $\vec{q}$ separately. Equation (C.8) is the general solution for the Wigner phase-space distribution function for propagation through an $ABCD$ optical system that contains a section of a random scattering medium. For an $ABCD$ system containing N sections of independent scattering media, the modification to the results given above is that the right-hand side of Eq. (C.10) becomes

$$\exp\left\{-\sum_{j=1}^{N} s_j[1-f_j(\vec{p},\vec{r})]\right\},$$

where s_j and $f_j(\vec{p},\vec{r})$ are the appropriate quantities that pertain to the jth scattering section. Note that the limits on the z' integration of the jth term in the summation are now from z_j to $z_j+\Delta z_j$.

It should be mentioned that in the special case where there is no scattering medium, i.e., $F = 1$, the result for the specific radiance obtained by using Eq. (C.8) is given by

$$N(\vec{P},\vec{\theta};Z) = N(D\vec{P} - B\vec{\theta}, \frac{\vec{P}}{B} - \frac{A}{B}(D\vec{P} - B\vec{\theta}); 0), \tag{C.12}$$

which is identical to Eq. (16) in Ref. [92] as expected.

Finally, the mutual coherence function,

$$\Gamma(\vec{P},\vec{p};Z) \equiv \left\langle U(\vec{P}+\vec{p}/2;Z)U^*(\vec{P}-\vec{p}/2;Z)\right\rangle, \tag{C.13}$$

corresponding to the Wigner function of Eq. (C.8) obtained by an inverse Fourier transform, is given by

$$\Gamma(\vec{P},\vec{p};Z) = \iint d\vec{R}d\vec{r}G(\vec{P},\vec{p},\vec{R},\vec{r};Z)\Gamma(\vec{R},\vec{r};0), \tag{C.14}$$

where $\Gamma(\vec{R},\vec{r};0)$ is the assumed given mutual coherence function in the initial plane and the corresponding kernel, G, for the propagation of mutual coherence is given by

$$\begin{aligned} G(\vec{P},\vec{p},\vec{R},\vec{r};Z) &= \left(\frac{k}{2\pi B}\right)^2 F(\vec{p},\vec{r}) \\ &\quad \times \exp\left\{i\frac{k}{B}\left[\vec{R}\cdot(\vec{p}-A\vec{r}) - \vec{P}\cdot(D\vec{p}-\vec{r})\right]\right\}, \end{aligned} \tag{C.15}$$

and F is given by Eq. (C.10). The mean irradiance distribution in the observation plane is given by $I(\vec{P};Z) = \Gamma(\vec{P},0;Z)$, and hence from Eq. (C.14), we obtain

$$\begin{aligned} I(\vec{P};Z) &= \iint d\vec{R}d\vec{r}G(\vec{P},0,\vec{R},\vec{r};Z)\Gamma(\vec{R},\vec{r};0) \\ &= \left(\frac{k}{2\pi B}\right)^2 \int d\vec{r}K(\vec{r})\Gamma_{\rm pt}(\vec{r})\exp\left(i\frac{k}{B}\vec{P}\cdot\vec{r}\right), \end{aligned} \tag{C.16}$$

where

$$K(\vec{r}) = \int d\vec{R}\exp\left(-i\frac{k}{B}A\vec{R}\cdot\vec{r}\right)U(\vec{R}+\vec{r}/2;0)U^*(\vec{R}-\vec{r}/2;0), \tag{C.17}$$

and $\Gamma_{\rm pt}(\vec{r}) = F(0,\vec{r})$ is the mutual coherence function of a point source located in the observation plane and evaluated in the initial plane, i.e., the backpropagated spherical-wave mutual coherence function. Equation (C.16) for the mean irradiance distribution in an $ABCD$ optical system is identical to Eq. (37) in section 2.2 as expected.

D The Wigner phase-space distribution function in $ABCD$ paraxial optical systems for direct propagation through random media with absorption

Here, for simplicity, we first consider a uniform small-angle scattering medium characterized by an index of refraction n and volume absorption and scattering coefficients $\mu_{\rm a}$ and $\mu_{\rm s}$, respectively. The Helmholtz Green's function in the

absorbing medium, $G_{\rm a}(\vec{R},\vec{P})$, is given by $\exp[-i\tilde{k}\,l(\vec{R},\vec{P})]/l(\vec{R},\vec{P})$, where $\tilde{k} = 2\pi n/\lambda - i\mu_{\rm a}/2$ and $l(\vec{R},\vec{P})$ is the distance between the vector positions $\vec{R}$ and $\vec{P}$ in the initial and the observation plane, respectively. In the paraxial approximation, this Green's function becomes

$$G_{\rm a}(\vec{R},\vec{P}) = \frac{e^{-ik_{\rm m}Z-\mu_{\rm a}Z/2}}{Z}\exp\left[-i\frac{k_{\rm m}}{2Z}(\vec{R}-\vec{P})^2 - \frac{\mu_{\rm a}}{2Z}(\vec{R}-\vec{P})^2\right], \qquad \text{(D.1)}$$

where Z is the propagation distance between the initial and the observation plane, respectively, and $k_{\rm m} = 2\pi n/\lambda$ is the optical wave number in the medium. In addition to the usual overall multiplicative absorption attenuation factor $e^{-\mu_{\rm a}Z/2}$, the Green's function contains an additional term, given by the second term in the exponent of Eq. (D.1), that represents the additional attenuation due to absorption of the light in propagating off the optic axis from $\vec{R}$ in the initial plane to $\vec{P}$ in the observation plane. Note that in all cases of practical concern, $k_{\rm m} \gg \mu_{\rm a}$, and hence $\left|\tilde{k}\right|^2 = k_{\rm m}^2 + \mu_{\rm a}^2/4 \simeq k_{\rm m}^2$. Proceeding in a manner similar to that which led to Eq. (C.1), we obtain that the Wigner function in the presence of an absorbing medium $W_{\rm a}$ is given by

$$W_{\rm a}(\vec{P},\vec{q};Z) = \iint d\vec{R}d\vec{q}'\,H_{\rm a}(\vec{P}-\vec{R},\vec{q}-\vec{q}';Z)W(\vec{R}-Z\vec{q}'/k,\vec{q}';0), \qquad \text{(D.2)}$$

where

$$\begin{aligned} H_{\rm a}(\vec{P}-\vec{R},\vec{q}-\vec{q}';Z) &= e^{-\mu_{\rm a}Z}\exp\left\{-\frac{\mu_{\rm a}}{8Z}\left[(\vec{p}-\vec{r})^2 + 4(\vec{P}-\vec{R})^2\right]\right\} \\ &\quad \times H(\vec{P}-\vec{R},\vec{q}-\vec{q}';Z). \end{aligned} \qquad \text{(D.3)}$$

As an example that clearly illustrates the physical effects of the off-axis propagation term in the Green's function, we consider a plane wave initially propagating along the optic axis. Rather than the Wigner function, we consider the corresponding specific radiance N, because it is perhaps easier to visualize physically. The specific radiance in the initial plane is given by $I_0\delta(\theta)$, where I_0 is the initial intensity and $\delta(\cdot)$ is the two-dimensional Dirac delta function. For definiteness, consider a scattering function whose phase correlation function is quadratic near the origin. Then it can be shown that in the multiple scattering regime, i.e., $\mu_{\rm s}Z \gg 1$, the specific radiance is given by

$$N(\theta;Z) = \frac{e^{-\mu_{\rm a}Z}I_0}{\pi\,\theta_{0{\rm a}}^2}\exp\left[-\theta^2/\theta_{0{\rm a}}^2\right], \qquad \text{(D.4)}$$

where

$$\theta_{0{\rm a}}^2 = \frac{\theta_0^2}{1+\frac{\mu_{\rm a}Z\,\theta_0^2}{6}}, \qquad \text{(D.5)}$$

$$\theta_0^2 = s\theta_{\rm rms}^2 = \mu_{\rm s}Z\,\theta_{\rm rms}^2. \qquad \text{(D.6)}$$

$\theta_{\rm rms}$ is the root-mean-square single-scattering angle defined in Eq. (72), and we have neglected terms of the order θ_0^4 with respect to θ_0^2. In the absence of absorption, $\theta_{0{\rm a}}^2 = \theta_0^2$. That is, the mean square angular spread of the light in the absence of absorption is given by the mean square single-scattering angle $\theta_{\rm rms}^2$ times the mean number of scattering events $\mu_{\rm s}Z$, i.e., a random walk. On the other hand, examination of Eq. (D.5) reveals that in the presence of absorption, the angular spread of the multiple-scattered component of the light is a decreasing function of the absorption depth $\mu_{\rm a}Z$, which tends to zero as $(\mu_{\rm a}Z)^{-1/2}$ as $\mu_{\rm a}Z \to \infty$. This is expected physically because the multiple-scattered light that propagates off axis travels a greater distance than the corresponding light that propagates near the axis. Hence the attenuation of the off-axis light is correspondingly greater than

that which propagates near the axis. That is, in addition to the decrease in magnitude of the specific radiance (Wigner function) with increasing values of $\mu_{\mathrm{a}}Z$, the corresponding angular (momentum) spread of the multiple-scattered component light progressively narrows. In general, not only does the radiance pattern (Wigner function) contain an overall absorption attenuation factor but, in addition, the angular distribution of the radiation pattern is a decreasing function of the absorption coefficient.

All treatments (see, for example, Refs. [78],[75],[85],[86]) where the effects of absorption are given only by an overall multiplicative factor of the form $e^{-\mu_{\mathrm{a}}Z}$ are, strictly speaking, incorrect and should be used with caution in applications of practical concern where absorption effects are important (e.g., the corresponding plane-wave radiance (Wigner function) is given by an equation of the form of Eq. (D.4) with $\theta_{0\mathrm{a}}^2$ replaced by θ_0^2, which is independent of the absorption coefficient).

To generalize the results given above to $ABCD$ optical systems, we replace Eq. (D.3) with

$$\begin{aligned} H_{\mathrm{a}}(\vec{P},\vec{R},\vec{q},\vec{q}\,';Z) &= e^{-\mu_{\mathrm{a}}\Delta z}\exp\{-\frac{\mu_{\mathrm{a}}}{8\,B}[A(\vec{p}^{\,2}+4\vec{P}^2)-2\vec{p}\cdot\vec{r}+D\vec{r}^{\,2} \\ &\quad -8\vec{P}\cdot\vec{R}+4D\vec{R}^2]\}H(\vec{P},\vec{R},\vec{q},\vec{q}\,';Z), \end{aligned} \tag{D.7}$$

where, as indicated above, A, B, and D are the (real) $ABCD$ ray-matrix elements for backpropagation through the optical system, i.e., from the observation plane to the initial plane, Δz is the thickness of random medium that is located between $z' = z$ and $z' = z + \Delta z$, and the quantity H is given by Eq. (C.9).

E Appendix

Consider the Fourier transform, $F\left(\vec{q}\right)$, of the mean irradiance profile

$$F\left(\vec{q}\right) = \int d\vec{r}\,\langle I_{\mathrm{B}}\left(\vec{r}\right)\rangle \exp\left(i\vec{q}\cdot\vec{r}\right), \tag{E.1}$$

where, for general real $ABCD$ systems, it can be shown that [49]

$$\langle I_{\mathrm{B}}\left(\vec{r}\right)\rangle = R_{\mathrm{d}}\left(\frac{k}{2\pi B}\right)^2 \int d\vec{u}\exp\left(i\frac{k}{B}\vec{r}\cdot\vec{u}\right) K\left(\vec{u}\right)\Gamma_{\mathrm{pt}}\left(u\right), \tag{E.2}$$

and the other terms have been previously defined. Substituting Eq. (E.2) into Eq. (E.1) and performing the $\vec{r}$ integration yields

$$\begin{aligned} F(\vec{q}) &= R_{\mathrm{d}}\left(\frac{k}{2\pi B}\right)^2 \int d\vec{u}K(\vec{u})\Gamma_{\mathrm{pt}}(u)(2\pi)^2\delta(\vec{q}+k\vec{u}/B) \\ &= R_{\mathrm{d}}\Gamma_{\mathrm{pt}}\left(-\frac{B}{k}q\right)K\left(-\frac{B}{k}\vec{q}\right), \end{aligned} \tag{E.3}$$

where $\delta\left(\cdot\right)$ is the two-dimensional Dirac delta function. It follows directly from Eq. (E.3) and Eq. (64) that

$$H(\vec{p}) = F(k\vec{p}/B_{\mathrm{b}}) = R_{\mathrm{d}}\Gamma_{\mathrm{pt}}(-p)K(-\vec{p}) = R_{\mathrm{d}}\Gamma_{\mathrm{pt}}^*(p)K(-\vec{p}). \tag{E.4}$$

References

[1] D. Huang, E. A. Swanson, C. P. Lin, J. S. Schuman, W. G. Stinson, W. Chang, M. R. Hee, T. Flotte, K. Gregory, C. A. Puliafito, and J. G. Fujimoto. Optical coherence tomography. *Science*, 254:1178–1181, 1991.

[2] R. C. Youngquist, S. Carr, and D. E. N. Davies. Optical coherence-domain reflectometry: A new optical evaluation technique. *Opt. Lett.*, 12:158–160, 1987.

[3] K. Takada, I. Yokohama, K. Chida, and J. Noda. New measurement system for fault location in optical waveguide devices based on an interferometric technique. *Appl. Opt.*, 26:1603–1606, 1987.

[4] A. F. Fercher, K. Mengedoht, and W. Werner. Eye-length measurement by interferometry with partially coherent-light. *Opt. Lett.*, 13:186–188, 1988.

[5] C. K. Hitzenberger. Optical measurement of the axial eye length by laser Doppler interferometry. *Inv. Ophthalmol. Vis. Sci.*, 32:616–624, 1991.

[6] D. Huang, J. P. Wang, C. P. Lin, C. A. Puliafito, and J. G. Fujimoto. Micron-resolution ranging of cornea anterior-chamber by optical reflectometry. *Lasers Surg. Med.*, 11:419–425, 1991.

[7] J. W. Goodman. *Statistical Optics*. J. Wiley & Sons, New York, 1985.

[8] E. A. Swanson, D. Huang, M. R. Hee, J. G. Fujimoto, C. P. Lin, and C. A. Puliafito. High-speed optical coherence domain reflectometry. *Opt. Lett.*, 17:151–153, 1992.

[9] J. M. Schmitt. Optical coherence tomography (OCT): A review. *IEEE J. Select. Topics Quantum Electron.*, 5:1205–1215, 1999.

[10] U. Morgner, F. X. Kärtner, S. H. Cho, Y. Chen, H. A. Haus, J. G. Fujimoto, E. P. Ippen, V. Scheuer, G. Angelow, and T. Tschudi. Sub-two-cycle pulses from a Kerr-lens mode-locked Ti:Sapphire laser. *Opt. Lett.*, 24:411–413, 1999.

[11] W. Drexler, U. Morgner, F. X. Kärtner, C. Pitris, S. A. Boppart, X. D. Li, E. P. Ippen, and J. G. Fujimoto. In vivo ultrahigh resolution optical coherence tomography. *Opt. Lett.*, 24:1221–1223, 1999.

[12] K. Takada. Noise in optical low-coherence reflectometry. *IEEE J. Quantum Electron.*, 34:1098–1108, 1998.

[13] A. G. Podoleanu. Unbalanced versus balanced operation in an optical coherence tomography system. *Appl. Opt.*, 39:173–182, 2000.

[14] B. E. Bouma and G. J. Tearney. Power-efficient nonreciprocal interferometer and linear-scanning fiber-optic catheter for optical coherence tomography. *Opt. Lett.*, 24:531–533, 1999.

[15] A. M. Rollins and J. A. Izatt. Optimal interferometer designs for optical coherence tomography. *Opt. Lett.*, 24:1484–1486, 1999.

[16] A. M. Rollins, M. D. Kulkarni, S. Yazdanfar, R. Ung-Arunyawee, and J. A. Izatt. In vivo video rate optical coherence tomography. *Opt. Express*, 3:219–229, 1998.

[17] A. M. Weiner, D. E. Leaird, J. S. Patel, and J. R. Wullert. Programmable femtosecond pulse shaping by use of a multielement liquid-crystal phase modulator. *Opt. Lett.*, 15:326–328, 1990.

[18] K. F. Kwong, D. Yankelevich, K. C. Chu, J. P. Heritage, and A. Dienes. 400-Hz mechanical scanning optical delay line. *Opt. Lett.*, 18:558–560, 1993.

[19] G. J. Tearney, M. E. Brezinski, B. E. Bouma, S. A. Boppart, C. Pitris, J. F. Southern, and J. G. Fujimoto. In vivo endoscopic optical biopsy with optical coherence tomography. *Science*, 276:2037–2039, 1997.

[20] G. J. Tearney, B. E. Bouma, and J. G. Fujimoto. High speed phase- and group-delay scanning with a grating-based phase control delay line. *Opt. Lett.*, 22:1811–1813, 1997.

[21] J. A. Izatt, M. R. Hee, E. A. Swanson, C. P. Lin, D. Huang, J. S. Schuman, C. A. Puliafito, and J. G. Fujimoto. Micrometer-scale resolution imaging of the anterior eye in vivo with optical coherence tomography. *Arch. Ophthalmol.*, 112:1584–1589, 1994.

[22] M. R. Hee, J. A. Izatt, E. A. Swanson, D. Huang, J. S. Schuman, C. P. Lin, C. A. Puliafito, and J. G. Fujimoto. Optical coherence tomography of the human retina. *Arch. Ophthalmol.*, 113:325–332, 1995.

[23] C. A. Puliafito, M. R. Hee, C. P. Lin, E. Reichel, J. S. Schuman, J. S. Duker, J. A. Izatt, E. A. Swanson, and J. G. Fujimoto. Imaging of macular diseases with optical coherence tomography. *Ophthalmology*, 102:217–229, 1995.

[24] M. E. Brezinski and J. G. Fujimoto. Optical coherence tomography: High-resolution imaging in nontransparent tissue. *IEEE J. Select. Topics Quantum Electron.*, 5:1185–1192, 1999.

[25] J. G. Fujimoto, C. Pitris, S. A. Boppart, and M. E. Brezinski. Optical coherence tomography: An emerging technology for biomedical imaging and optical biopsy. *Neoplasia*, 2:9–25, 2000.

[26] H. T. Yura. Signal-to-noise ratio of heterodyne lidar systems in the presence of atmospheric turbulence. *Optica Acta*, 26:627–644, 1979.

[27] I. Dror, A. Sandrov, and N. S. Kopeika. Experimental investigation of the influence of the relative position of the scattering layer on image quality: the shower curtain effect. *Appl. Opt.*, 37:6495–6499, 1998.

[28] J. M. Schmitt, A. Knüttel, and R. F. Bonner. Measurement of optical properties of biological tissues by low-coherence reflectometry. *Appl. Opt*, 32:6032–6042, 1993.

[29] J. M. Schmitt, A. Knüttel, A. S. Gandjbakhche, and R. F. Bonner. Optical characterization of dense tissues using low-coherence interferometry. *Proc. SPIE*, 1889:197–211, 1993.

[30] M. J. Yadlowsky, J. M. Schmitt, and R. F. Bonner. Multiple scattering in optical coherence microscopy. *Appl. Opt.*, 34:5699–5707, 1995.

[31] M. J. Yadlowsky, J. M. Schmitt, and R. F. Bonner. Contrast and resolution in the optical coherence microscopy of dense biological tissue. *Proc. SPIE*, 2387:193–203, 1995.

[32] Y. Pan, R. Birngruber, and R. Engelhardt. Contrast limits of coherence-gated imaging in scattering media. *Appl. Opt.*, 36:2979–2983, 1997.

[33] J. M. Schmitt and A. Knüttel. Model of optical coherence tomography of heterogeneous tissue. *J. Opt. Soc. Am. A*, 14:1231–1242, 1997.

[34] D. J. Smithies, T. Lindmo, Z. Chen, J. S. Nelson, and T. E. Milner. Signal attenuation and localization in optical coherence tomography studied by Monte Carlo simulation. *Phys. Med. Biol.*, 43:3025–3044, 1998.

[35] L. Thrane, H. T. Yura, and P. E. Andersen. Analysis of optical coherence tomography systems based on the extended Huygens-Fresnel principle. *J. Opt. Soc. Am. A*, 17:484–490, 2000.

[36] L. Thrane, H. T. Yura, and P. E. Andersen. Optical coherence tomography: New analytical model and the shower curtain effect. *Proc. SPIE*, 4001:202–208, 2000.

[37] L. Thrane, H. T. Yura, and P. E. Andersen. Calculation of the maximum obtainable probing depth of optical coherence tomography in tissue. *Proc. SPIE*, 3915:2–11, 2000.

[38] A. Tycho, T. M. Jørgensen, and L. Thrane. Investigating the focusing problem in OCT: Comparison of Monte Carlo simulations, the extended Huygens-Fresnel principle and experiments. *Proc. SPIE*, 3915:25–35, 2000.

[39] P. E. Andersen, L. Thrane, H. T. Yura, A. Tycho, and T. M. Jørgensen. Modeling the optical coherence tomography geometry using the extended Huygens-Fresnel principle and Monte Carlo simulations. *Proc. SPIE*, 3914:394–406, 2000.

[40] V. I. Tatarskii. *Wave Propagation in a Turbulent Medium.* McGraw-Hill, New York, 1961.

[41] A. Ishimaru. *Wave Propagation and Scattering in Random Media.* IEEE Press, Piscataway, New Jersey, 1997.

[42] J. Strohbehn, editor. *Laser Beam Propagation in the Atmosphere.* Springer, New York, 1978.

[43] R. L. Fante. Wave propagation in random media: A systems approach. In *Progress in Optics XXII.* Elsevier, New York, 1985.

[44] J. M. Schmitt and G. Kumar. Turbulent nature of refractive-index variations in biological tissue. *Opt. Lett.*, 21:1310–1312, 1996.

[45] S. M. Rytov, Y. A. Kravtsov, and V. I. Tatarskii. Principles of statistical radiophysics. In *Wave Propagation Through Random Media*, volume 4. Springer, Berlin, 1989.

[46] R. F. Lutomirski and H. T. Yura. Propagation of a finite optical beam in an inhomogeneous medium. *Appl. Opt.*, 10:1652–1658, 1971.

[47] Z. I. Feizulin and Y. A. Kravtsov. Expansion of a laser beam in a turbulent medium. *Izv. Vyssh. Uchebn. Zaved. Radiofiz.*, 24:1351–1355, 1967.

[48] J. W. Goodman. *Introduction to Fourier Optics.* McGraw-Hill, Singapore, second edition, 1996.

[49] H. T. Yura and S. G. Hanson. Optical beam wave propagation through complex optical systems. *J. Opt. Soc. Am. A*, 4:1931–1948, 1987.

[50] H. T. Yura and S. G. Hanson. Second-order statistics for wave propagation through complex optical systems. *J. Opt. Soc. Am. A*, 6:564–575, 1989.

[51] A. E. Siegman. *Lasers.* University Science Books, Mill Valley, California, 1986. section 16.1.

[52] M. J. C. Van Gemert, S. L. Jacques, H. J. C. M. Sterenborg, and W. M. Star. Skin optics. *IEEE Transactions on Biomedical Engineering*, 36:1146–1154, 1989.

[53] C. F. Bohren and D. R. Huffman. *Absorption and Scattering of Light by Small Particles*. John Wiley & Sons, New York, 1983.

[54] H. T. Yura and S. G. Hanson. Effects of receiver optics contamination on the performance of laser velocimeter systems. *J. Opt. Soc. Am. A*, 13:1891–1902, 1996.

[55] H. T. Yura. Private communication, 1998.

[56] L. G. Henyey and J. L. Greenstein. Diffuse radiation in the galaxy. *Astrophysical J.*, 93:70–83, 1941.

[57] S. L. Jacques, C. A. Alter, and S. A. Prahl. Angular dependence of He-Ne laser light scattering by human dermis. *Lasers Life Sci.*, 1:309–333, 1987.

[58] C. M. Sonnenschein and F. A. Horrigan. Signal-to-noise relationships for coaxial systems that heterodyne backscatter from the atmosphere. *Appl. Opt.*, 10:1600–1604, 1971.

[59] D. L. Fried. Optical heterodyne detection of an atmospherically distorted signal wave front. *Proc. IEEE*, 55:57–67, 1967.

[60] V. I. Tatarskii. *The Effects of the Turbulent Atmosphere on Wave Propagation*. National Technical Information Service, Springfield, Va., 1971.

[61] V. V. Tuchin, S. R. Utz, and I. V. Yaroslavsky. Skin optics: Modeling of light transport and measuring of optical parameters. In *Medical Optical Tomography: Functional Imaging and Monitoring*, volume IS11, pages 234–258. SPIE Press, Bellingham, Washington, 1993.

[62] D. A. Boas, K. K. Bizheva, and A. M. Siegel. Using dynamic low-coherence interferometry to image Brownian motion within highly scattering media. *Opt. Lett.*, 23:319–321, 1998.

[63] R. N. McDonough and A. D. Whalen. *Detection of Signals in Noise*. Academic Press, San Diego, CA., 1995.

[64] S. A. Prahl, M. J. C. Van Gemert, and A. J. Welch. Determining the optical properties of turbid media by using the adding-doubling method. *Appl. Opt.*, 32:559–568, 1993.

[65] E. Lankenau, J. Welzel, R. Birngruber, and R. Engelhardt. In vivo tissue measurements with optical low coherence tomography. *Proc. SPIE*, 2981:78–84, 1997.

[66] E. G. Jung. *Dermatologie*. Hippokrates Verlag, Stuttgart, Germany, 1989.

[67] P. Therkildsen, M. Hædersdal, J. Lock-Andersen, F. de Fine Olivarius, T. Poulsen, and H. C. Wulf. Epidermal thickness measured by light microscopy: A methodological study. *Skin Res. and Tech.*, 4:174–179, 1998.

[68] A. Knüttel and M. Boehlau-Godau. Spatially confined and temporally resolved refractive index and scattering evaluation in human skin performed with optical coherence tomography. *J. Biomed. Opt.*, 5:83–92, 2000.

[69] G. J. Tearney, M. E. Brezinski, M. R. Hee, B. Bouma, J. A. Izatt, E. A. Swanson, J. F. Southern, R. R. Anderson, and J. G. Fujimoto. Optical coherence tomography in multiply scattering tissue. *Proc. SPIE*, 2389:29–34, 1995.

[70] M. Hædersdal, P. Therkildsen, N. Bech-Thomsen, T. Poulsen, and H. C. Wulf. Side effects from dermatological laser treatment related to UV exposure and epidermal thickness: A murine experiment with the copper vapor laser. *Lasers Surg. Med.*, 20:233–241, 1997.

[71] F. Lexer, C. K. Hitzenberger, W. Drexler, S. Molebny, H. Sattmann, M. Sticker, and A. F. Fercher. Dynamic coherent focus OCT with depth-independent transversal resolution. *J. Mod. Opt.*, 46:541–553, 1999.

[72] E. P. Wigner. On the quantum correction for thermodynamic equilibrium. *Phys. Rev.*, 40:749–759, 1932.

[73] M. G. Raymer, C. Cheng, D. M. Toloudis, M. Anderson, and M. Beck. Propagation of Wigner coherence functions in multiple scattering media. In *Advances in Optical Imaging and Photon Migration*, volume 2 of *OSA Trends in Optics and Photonics Series*, pages 236–238. Optical Society of America, Washington, D.C., 1996.

[74] S. John, G. Pang, and Y. Yang. Optical coherence propagation and imaging in a multiple scattering medium. *J. Biomed. Opt.*, 1:180–191, 1996.

[75] A. Wax and J. E. Thomas. Measurement of smoothed Wigner phase-space distributions for small-angle scattering in a turbid medium. *J. Opt. Soc. Am. A*, 15:1896–1908, 1998.

[76] C.-C. Cheng and M. G. Raymer. Long-range saturation of spatial decoherence in wave-field transport in random multiple-scattering media. *Phys. Rev. Lett.*, 82:4807–4810, 1999.

[77] M. G. Raymer and C.-C. Cheng. Propagation of the optical Wigner function in random multiple-scattering media. *Proc. SPIE*, 3914:372–380, 2000.

[78] C.-C. Cheng and M. G. Raymer. Propagation of transverse optical coherence in random multiple-scattering media. *Phys. Rev. A*, 62:023811–1–023811–12, 2000.

[79] M. Artin. *Algebra*. Prentice Hall, Englewood Cliffs, New Jersey, 1991.

[80] A. Wax, S. Bali, and J. E. Thomas. Time-resolved phase-space distributions for light backscattered from a disordered medium. *Phys. Rev. Lett.*, 85:66–69, 2000.

[81] H. T. Yura, L. Thrane, and P. E. Andersen. Closed-form solution for the Wigner phase-space distribution function for diffuse reflection and small-angle scattering in a random medium. *J. Opt. Soc. Am. A*, 17:2464–2474, 2000.

[82] M. Hillery, R. F. O'Connell, M. O. Scully, and E. P. Wigner. Distribution functions in physics: fundamentals. *Phys. Rep.*, 106:121–167, 1984.

[83] V. A. Banakh and V. L. Mironov. *LIDAR in a Turbulent Atmosphere*. Artech House, Boston, MA, 1987.

[84] S. L. Jacques and L. Wang. Monte Carlo modeling of light transport in tissues. In *Optical-Thermal Response of Laser-Irradiated Tissue*, chapter 4. Plenum Press, New York, 1995.

[85] H. T. Yura. A multiple scattering analysis of the propagation of radiance through the atmosphere. In *Proceedings of the Union Radio-Scientifique Internationale Open Symposium*, pages 65–69, La Baule, France, 1977.

[86] D. Arnush. Underwater light-beam propagation in the small-angle-scattering approximation. *J. Opt. Soc. Am.*, 62:1109–1111, 1972.

[87] K. F. Lee, F. Reil, S. Bali, A. Wax, and J. E. Thomas. Heterodyne measurement of Wigner distributions for classical optical fields. *Opt. Lett.*, 24:1370–1372, 1999.

[88] A. Wax and J. E. Thomas. Measurement of smoothed Wigner phase space distributions for coherence tomography. *Proc. SPIE*, 3726:494–501, 1998.

[89] A. Wax and J. E. Thomas. Measurement of smoothed Wigner phase space distributions for low coherence light in multiple scattering media. *Proc. SPIE*, 3598:2–9, 1999.

[90] A. Wax, S. Bali, and J. E. Thomas. Optical phase-space distributions for low-coherence light. *Opt. Lett.*, 24:1188–1190, 1999.

[91] R. F. Lutomirski. Atmospheric degradation of electrooptical system performance. *Appl. Opt.*, 17:3915–3921, 1978.

[92] A. T. Friberg. Propagation of a generalized radiance in paraxial optical systems. *Appl. Opt.*, 30:2443–2446, 1991.

List of symbols

a	linear dimension of illuminated region
b_ϕ	normalized phase autocorrelation function
d	distance between lens and tissue surface
$\mathrm{erf}(\cdot)$	error function
f	focal length
$f(\cdot)$	specific radiance (Arnush, section 5.4)
$f_0(\cdot)$	specific radiance at $z = 0$ (Arnush, section 5.4)
f_d	Doppler frequency
g	asymmetry parameter
$g(\tau)$	normalized temporal coherence function
h	Planck's constant
$i(z)$	heterodyne signal current
i_s	interference signal
$\langle i^2 \rangle_0$	mean square heterodyne signal current in the absence of scattering
k	wave number
$\tilde{k}$	complex wave number
k_m	wave number in medium
l	transverse intensity correlation length
$l(\vec{R}, \vec{P})$	distance between the vector positions $\vec{R}$ and $\vec{P}$
l_c	coherence length
l_0	scale of smallest random inhomogeneities
n, n_1	index of refraction of tissue
n_f	small fluctuating part of the index of refraction
n_g	index of refraction of cuvette glass plate
$\vec{p}, \vec{p}_1, \vec{p}_2$	two-dimensional position vector
$q, \vec{q}, \vec{q}'$	transverse momentum
q_e	electronic charge
$\vec{r}, \vec{r}_1, \vec{r}_2$	two-dimensional position vector
r_0	Henyey-Greenstein phase correlation length
s	optical depth
s_j	optical depth for the jth scattering section
s_N	near-forward contribution to the optical depth
s_W	wide-angle contribution to the optical depth
t	time
u	normalized transverse coordinate
$\vec{u}, \vec{u}'$	ray direction (Arnush, section 5.4)
v	scan velocity of reference mirror
w_H	$1/e$ irradiance radius in discontinuity plane in the absence of scattering
w_S	$1/e$ irradiance radius in discontinuity plane in the presence of scattering
w_0	$1/e$ intensity radius in the lens plane
z	depth of discontinuity in tissue
z'	propagation variable
z_max	maximum probing depth
A, A_b	ray-matrix element
$B, B_\mathrm{b}, B(L)$	ray-matrix element
B_w	system bandwidth

D, D_b	ray-matrix element
$\vec{E}$	electric field
G	extended Huygens-Fresnel Green's function
G_a	Helmholtz Green's function for absorbing medium
G_ca	current amplifier gain
G_0	Huygens-Fresnel Green's function
H	propagation kernel for the Wigner distribution function
H_a	propagation kernel for the Wigner distribution function, absorbing medium
H_t	Hilbert transform
I, I_0	irradiance
I_B	backscattered irradiance in the discontinuity plane
J_0	Bessel function of the first kind of order zero
L	distance from discontinuity plane to lens plane
N	specific radiance
N_p	mean square noise power
NA	numerical aperture
$\vec{P}$	two-dimensional position vector
P_R	power of reference beam
P_S	power of input sample beam
P_0	transmitted power
$\vec{R}$	point in space
R_d	Fresnel reflection coefficient
R_l	resistance of load
S	mean heterodyne signal power
SNR	signal-to-noise ratio
$(\mathrm{SNR})_0$	signal-to-noise ratio in the absence of scattering
$U(\vec{R})$	scalar component of $\vec{E}$
U_B	reflected sample field in the discontinuity plane
U_R	reference field
U_S	sample field
U_Si	input sample field
U_0	field in input plane
W	Wigner phase-space distribution
W_a	Wigner function in the presence of an absorbing medium
W_R	Wigner phase-space distribution function of reference beam
W_S	Wigner phase-space distribution function of sample beam
Z	one-way propagation distance
α	conversion factor for power to current
δ	thickness of cuvette glass plate
$\delta(\cdot)$	two-dimensional Dirac delta function
η	detector quantum efficiency
θ	scattering angle
$\vec{\theta}$	ray direction
θ_0a	root mean square angular spread of light in presence of absorption
θ_rms	rms scattering angle
λ	center wavelength
$\Delta\lambda$	FWHM spectral bandwidth
μ_a	absorption coefficient
μ_s	scattering coefficient

ν	optical frequency
ρ_0	lateral coherence length
ρ_ϕ	phase correlation length
σ	volume scattering function
σ_b	effective backscattering cross section of tissue discontinuity
τ	propagation time difference of reference and sample beams
ϕ	random phase of spherical wave
ϕ_R	phase of reference field relative to input sample field
ω_R	angular frequency of reference beam
ω_S	angular frequency of input sample beam
Γ_pt	mutual coherence function of point source
Γ_R	mutual coherence function of reference field
Γ_S	mutual coherence function of sample field
Δ_q	$1/e$ transverse momentum width
Δz	thickness of random medium
Σ	normalized scattering function (Arnush, section 5.4)
Φ_n	3d spectrum of the index of refraction inhomogeneities
Ψ	heterodyne efficiency factor
Ω	solid angle

Bibliographic Data Sheet **Risø–R–1217(EN)**

Title and author(s)

Optical Coherence Tomography: Modeling and Applications

Lars Thrane

ISBN
87–550–2771–7; 87–550–2882–9 (Internet)

ISSN
0106–2840

Dept. or group
Optics and Fluid Dynamics Department

Date
May 2001

Groups own reg. number(s)

Project/contract No.

Sponsorship

Pages	Tables	Illustrations	References
77	0	33	92

Abstract (Max. 2000 char.)

An analytical model is presented that is able to describe the performance of OCT systems in both the single and multiple scattering regimes simultaneously. This model inherently includes the *shower curtain effect*, well-known for light propagation through the atmosphere. This effect has been omitted in previous theoretical models of OCT systems. It is demonstrated that the shower curtain effect is of utmost importance in the theoretical description of an OCT system. The analytical model, together with proper noise analysis of the OCT system, enables calculation of the SNR, where the optical properties of the tissue are taken into account. Furthermore, by using the model, it is possible to determine the lateral resolution of OCT systems at arbitrary depths in the scattering tissue. During the Ph.D. thesis project, an OCT system has been constructed, and the theoretical model is verified experimentally using this system. A demonstration of the imaging capabilities of the OCT system is given. Moreover, a novel *true-reflection OCT imaging algorithm*, based on the new OCT model presented in this thesis, is demonstrated. Finally, a theoretical analysis of the Wigner phase-space distribution function for the OCT geometry, i.e., reflection geometry, is developed. As in the new OCT model, multiple scattered photons has been taken into account together with multiple scattering effects. As an important result, a novel method of creating images based on measurements of the momentum width of the Wigner phase-space distribution is presented, and compared with conventional OCT.

Descriptors INIS/EDB

Available on request from:
Information Service Department, Risø National Laboratory
(Afdelingen for Informationsservice, Forskningscenter Risø)
P.O. Box 49, DK–4000 Roskilde, Denmark
Phone (+45) 46 77 46 77, ext. 4004/4005 · Fax (+45) 46 77 40 13
E-mail: risoe@risoe.dk